

ANNUAL REPORT 2013

INSTITUTE OF RESOURCE ECOLOGY

hzdr

 **HELMHOLTZ**
ZENTRUM DRESDEN
ROSSENDORF

Wissenschaftlich-Technische Berichte
HZDR-048

Annual Report 2013

Institute of Resource Ecology

Editor:

Prof. Dr. Thorsten Stumpf

Executive editors:

Dr. Harald Foerstendorf

Dr. Frank Bok

Dr. Anke Richter

HZDR

 **HELMHOLTZ**
ZENTRUM DRESDEN
ROSSENDORF

Print edition: ISSN 2191-8708

Electronic edition: ISSN 2191-8716

The electronic edition is published under Creative Commons License (CC BY-NC-ND):

Qucosa: <http://fzd.qucosa.de/startseite/>

Published by Helmholtz-Zentrum Dresden-Rossendorf e.V.

Contact

Helmholtz-Zentrum Dresden-Rossendorf e.V.
Institute of Resource Ecology

Postal Address

P.O. Box 51 01 19
D-01314 Dresden
Germany

Address for visitors

Bautzner Landstraße 400
D-01328 Dresden
Germany

Phone: +49 (0) 351 260 3210

Fax: +49 (0) 351 260 3553

e-mail: contact.resourceecology@hzdr.de

<http://www.hzdr.de/FWO>

This report is also available at <http://www.hzdr.de/FWO>

Cover picture

Decontamination of mine water from uranium and heavy metals can be achieved by biofilms. For this purpose, the mine water of the former uranium mine in Königstein, Saxony, pass through flow cells where microorganisms build biofilms at the surface of glass slides (inset on the right bottom). The biofilms can be visualized by Confocal Laser Scanning Microscopy (CLSM). The compounds of the biofilms, that is the matrix, microorganisms, and ferric iron compounds/heavy metals, were stained by different fluorescence dyes and appear as green, red and grey areas, respectively (left). Additionally, the thickness of the biofilm can be determined by depth profiling using CLSM and is in the order of 20 µm (small stripes below and beside the CLSM picture). The pictures are a result of cooperation with Th. Neu (UFZ Magdeburg) by using IMARIS software. For details see p. 11.

Preface

THE INSTITUTE OF RESOURCE ECOLOGY (IRE) IS one of the eight institutes of the Helmholtz-Zentrum Dresden-Rossendorf (HZDR). The research activities are mainly integrated into the program “Nuclear Safety Research (NUSAFE)” of the Helmholtz Association (HGF) and focused on the topics “Safety of Nuclear Waste Disposal” and “Safety Research for Nuclear Reactors”.

Additionally, various activities have been started investigating chemical and environmental aspects of processing and recycling of strategic metals, namely rare earth elements. These activities are located in the HGF program “Energy Efficiency, Materials and Resources (EMR)”. Both programs, and therefore all work which is done at IRE, belong to the research sector “Energy” of the HGF.

The research objectives are the protection of humans and the environment from hazards caused by pollutants resulting from technical processes that produce energy and raw materials. Treating technology and ecology as a unity is the major scientific challenge in assuring the safety of technical processes and gaining their public acceptance. Namely, we investigate the ecological risks exerted by radioactive and non-radioactive metals in the context of nuclear waste disposal, the production of energy in nuclear power plants and in processes along the value chain of metalliferous raw materials. A common goal is to generate better understanding about the dominating processes essential for metal mobilization and immobilization on the molecular level. This in turn enables us to assess the macroscopic phenomena, including models, codes and data for predictive calculations, which determine the transport and distribution of contaminants in the environment.

The extraordinary broadness of topics is shown by some selected research highlights in 2013:

- The in-house developed reactor dynamics code DYN3D has been coupled with the well validated fuel performance code TRANSURANUS maintained by the EU Joint Research Center - ITU Karlsruhe. Due to the higher degree of detail in fuel behavior modeling in this coupling, the application range of DYN3D to the analysis of hypothetical accidents in Light Water Reactors, especially the control rod ejection event, has been extended.
- In the Reactive Transport Division, considerable progress has been achieved in elucidating basic processes of contaminant transport in complex systems. In radio-tracer exchange studies, evidence was provided for the first time that interaction of natural organic matter with mineral surfaces and with higher-valent metals is based on dynamic equilibria - a major prerequisite of transport modelling.
- In an international cooperation the formation of uranium(IV) colloids in a wetland area of a former mining site could be proved. In the soil the uranium(IV) was found to be a non-crystalline species bound to Al-P-Fe-Si aggregates. In the porewater the uranium was associated with Fe and organic matter colloids. These mobile porewater colloids are responsible for the release into surface water.
- Rare earth elements exhibit strong affinities to a large number of biomolecules. We have shown the super-

structure-dependent complexation of europium with rationally designed synthetic triangular DNA-origami. The europium-decorated triangles carry up to 2000 europium ions providing the first demonstration of a paramagnetically decorated synthetic DNA structure. It allows magnetic orientation of these nanoparticles which may allow novel applications in rare earth separation and in molecular alignments for NMR structure determination.

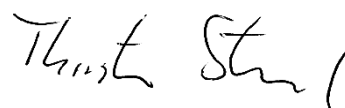
- Within the VESPA project (funded by BMWi) the sorption of Se(IV) and Se(VI) onto a variety of Fe corrosion products was investigated. The formation (depending on redox potential and pH) of up to three different surface species could be detected, and the respective structure of these inner- and outer-sphere complexes was derived applying EXAFS and ATR FT-IR techniques. The obtained distribution coefficients were demonstrated to reduce Se mobility in salt and clay host rocks for nuclear waste repositories by one to two orders of magnitude.

Beside these highlights, we obtained many other new scientific results in the past year which are presented in this Annual Report. Furthermore, 60 original papers were published in peer-reviewed international scientific journals. In the year 2013, more than 120 scientists, technicians, and students – working on their Ph.D., diploma, master, or bachelor thesis – were employed at the Institute of Resource Ecology. More than 30 Ph.D. students are working at the institute. Promotion of young scientists is an important requirement to ensure the competence and further scientific excellence in future times.

I would like to thank the visitors, German and international ones, for their interest in our research and for their participation in the institute seminars. We further like to thank our scientific collaborators and the visiting scientists for coming to Dresden-Rossendorf in 2013 to share their knowledge and experience with us. We will continue to strongly encourage the collaborations and visits by scientists in the future. Special thanks are due to the Executive Board of the HZDR, the Ministry of Science and Arts of the Free State Saxony (SMWK), the Federal Ministry of Education and Research (BMBF), the Federal Ministry of Economics and Technology (BMWV), the Deutsche Forschungsgemeinschaft (DFG), the European Commission, and other organizations for their support.

The past year was also accompanied by considerable efforts in preparing material for the large HGF strategic program evaluation. The results of this evaluation by a high-ranked international review panel will be communicated in our annual report 2014.

Last but not least, I would like thanking Vinzenz Brendler for heading the Institute of Resource Ecology 18 months as an acting director. When I joined the institute in October 2013 I found the IRE in an extraordinary good condition and that is mainly to his credit!



Prof. Dr. Thorsten Stumpf
Director of the
Institute of Resource Ecology

Contents

SCIENTIFIC CONTRIBUTIONS

PART I: LONG-LIVED RADIONUCLIDES IN BIOLOGICAL SYSTEMS

Sorption of U(VI) and Np(V) on bacteriogenic Fe(III) oxyhydroxides from the Äspö Hard Rock Laboratory, Sweden	9
E. Krawczyk-Bärsch, K. Schmeide	
Laser fluorescence lifetime of uranyl species onto <i>Euglena mutabilis</i> determined with single photon avalanche diode and a multichannel event timer	10
N. Baumann, T. Arnold	
Cultivation of microorganisms live in the mine water of the former uranium mine Königstein, Germany.....	11
I. Zirnstein, S. Köppchen, I. Röske, T. Arnold	
Microbial community analysis of mine water from three abandoned uranium mines in East Germany	12
C. Gagell, T. Arnold, U. Jenk, K. Röske, I. Röske	
First insight into the impact of microorganisms on uranium sorption on selected minerals	13
C. Richter, K. Großmann, V. Brendler, C. Gagell	
The impact of the Opalinus clay isolate <i>Sporomusa</i> sp. MT-2.99 on the U(VI) speciation	14
L. Lütke, H. Moll, V. Bachvarova, S. Selenska-Pobell, G. Bernhard	
Cm(III)/Eu(III) speciation studies with the Opalinus clay isolate <i>Sporomusa</i> sp. MT-2.99	15
H. Moll, L. Lütke, V. Bachvarova, A. Cherkouk, S. Selenska-Pobell, G. Bernhard	
Interaction of Eu(III) with FaDu cells: Study of cell viability and Eu(III) uptake in the presence of Eu-152.....	16
S. Sachs	
Investigation of selenium reducing bacteria	17
S. Fischer, S. Fischer, C. Franzen, M. Vogel, R. Steudtner, J. Raff	
Encapsulation of <i>Bacillus</i> sp. B5T in sol-gel ceramics	18
M. Vogel, A. Pannier, U. Soltmann, J. Raff, K. Pollmann	
Metal binding capacities of calcium binding proteins Calmodulin and S-layer JG-A12.....	19
B. Drobot, F. Lehmann, H. Moll, J. Raff	
Interaction of the enzyme alpha-amylase with UO_2^{2+}	20
A. Barkleit, C. Hennig	
Interaction of europium with the S-layer protein of <i>Lysinibacillus sphaericus</i> JG-B53 studied by ICP-MS and TRLFS.....	21
M. Suhr, K. E. Viacava Romo, R. Steudtner, J. Raff, K. Fahmy, K. Pollmann	
Eu(III) binding to DNA origami.....	22
J. Oertel, L. Opherden, A. Barkleit, A. Keller, K. Fahmy	
Thermodynamic quantities of the complex formation between Nd(III) and malonate as a function of ionic strength.....	23
M. Müller, M. Acker, S. Taut	
Thermodynamics of the protonation of oxalic and malonic acid at various ionic strengths studied by micro titration calorimetry	24
F. Taube, M. Müller, M. Acker, S. Taut	
Isotope exchange studies on the reversibility of metal-humate complexation	25
H. Lippold	
EXAFS study of U(VI) with Schiff Bases in methanolic solution	26
K. Schulz, A. Günther, A. Rossberg, G. Bernhard	
Organo borate esters may serve as appropriate model compounds for inorganic borate complexes of trivalent actinides	27
J. Schott, J. Kretschmar, M. Acker, A. Barkleit, S. Taut, V. Brendler	
Data mining with artificial neural networks: aqueous U(VI) complexes with aliphatic (hydroxy-) carboxylic acids.....	28
A. Rossberg, K. Domaschke, C. Lucks, S. Tsushima	

PART II: LONG-LIVED RADIONUCLIDES IN FINAL DISPOSAL SYSTEMS

Uranyl(VI) speciation in strong alkaline solution	31
S. Tsushima, A. Rossberg, H. Moll, R. Steudtner, B. Drobot, K. Müller, K. Fahmy	
Specific surface speciation of uranium(VI) on iron (hydr)oxides	32
H. Foerstendorf, N. Jordan, K. Heim	
Uranium sorption on montmorillonite in four electrolyte systems of high ionic strength.....	33
K. Fritsch, K. Schneide	
In situ vibrational spectroscopic identification of Np(V) sorption reactions on ferrihydrite.....	34
K. Müller, J. Berger	
Np(V) retention by siderite.....	35
R. Steudtner, A. Maffert, A. C. Scheinost	
Incorporation of plutonium by magnetite under anoxic conditions.....	36
A. C. Scheinost, T. Dumas, A. Rossberg, D. Fellhauer, X. Gaona, M. Altmaier	
Uptake of Se(VI) by hematite.....	37
N. Jordan, S. Domaschke, H. Foerstendorf, A. C. Scheinost, C. Franzen, V. Zimmermann, S. Weiß, K. Heim	
Retention of selenate at the water-mineral interface in the context of salt dome repositories.....	38
C. Franzen, D. Hering, N. Jordan, S. Weiß, K. Heim	
Interaction of Ca ²⁺ and Mg ²⁺ with selenium oxyanions studied by ⁷⁷ Se NMR.....	39
J. Kretschmar, N. Jordan, E. Brendler, C. Franzen, V. Brendler	
Hexanuclear Ce(IV)-formate in aqueous solution and its solid state structure.....	40
C. Hennig, A. Ikeda-Ohno, W. Kraus, S. Weiß, P. Pattison, H. Emerich, P. M. Abdala, A. C. Scheinost	
EXAFS study of K-doped cobalt titanates for ethanol sensing	41
M. J. Lozano-Rodriguez, C. J. Belle, G. E. Wesch, S. Neumeier, A. C. Scheinost, U. Simon	
Environmental transport of TiO ₂ nanoparticles	42
S. Schymura, H. Hildebrand, K. Franke	
Solid-state properties and colloidal stability of thorium(IV)-silica nanoparticles	43
C. Hennig, S. Weiß, D. Banerjee, V. Honkimäki, E. Brendler, G. Cuello, A. Ikeda-Ohno, A. C. Scheinost, H. Zänker	
The nanocrystallinity of “amorphous” uranium(IV) oxyhydroxide	44
H. Zänker, S. Weiß, I. Ulbricht, R. Husar	
Dependence of morphology and dispersion of neptunium(IV) silica nanoparticles on silica content	45
R. Husar, S. Weiß, R. Hübner, H. Zänker	
Thermodynamic database for lanthanides: procedures and guidelines.....	46
V. Brendler, F. Bok, N. Jordan, A. Heller, M. Stockmann, C. Joseph, A. Barkleit, J. Schott, C. Richter	
Europium-TDB: review of thermodynamic data for Eu(III) complexation with inorganic ligands – First test results	47
F. Bok, V. Brendler	
Thermodynamic reference database THEREDA: 5. Test calculation cases of uranium(IV/VI) in the oceanic salt system including carbonates/CO ₂	48
A. Richter, F. Bok	
Two new radioactivity-scanners for 1D transport studies (LHS and IDDAS).....	49
T. Leipold, J. Hauser, K. Franke, J. Lippmann-Pipke	

PART III: NUCLEAR REACTOR SAFETY & TRANSMUTATION

The trigonal-geometry diffusion model of the reactor dynamics code DYN3D	53
S. Duerigen	
New coupling approach DYN3D-TRANSURANUS shows limitations of simplified fuel behavior modeling already at low burn-up.....	54
L. Holt, U. Rohde	
Development of a transport solver for DYN3D	55
D. Litskevich, B. Merk	

Uncertainty and sensitivity analysis for a large break accident simulation for a PWR	56
U. Rohde, Y. Kozmenkov	
Application of the system code ATHLET from nuclear engineering onto solar thermal power plants	57
A. Hoffmann	
Neutron fluence calculations in the cavity of a VVER-440/213 reactor and of surveillance specimens positions	58
J. Konheiser, A. Grahn	
Neutronic and thermal-hydraulic analysis of High Conversion Th-U233 PWR core	59
D. Baldova, E. Fridman	
Coolant mixing experiments at the ROCOM test facility for a main steam line break scenario.....	60
S. Kliem, R. Franz	
Conceptual design of a pressure tube light water reactor with variable moderator control (PTVM LWR)	61
R. Rachamin, E. Fridman, A. Galperin	

PUBLICATIONS

▣ Articles (peer-reviewed)	65
▣ Extended Abstracts, Reports, Contributions.....	69
▣ Lectures, Oral Presentations	70
▣ Posters	75
▣ Award	79
▣ Doctoral Theses	79
▣ Master, Diploma, Bachelor.....	80

SCIENTIFIC ACTIVITIES

▣ Seminars	83
▣ Workshops; (co)-organized by the IRE	84
▣ Teaching Activities.....	88

PERSONNEL

89

ACKNOWLEDGEMENTS

95

INDEX OF AUTHORS

100

SCIENTIFIC CONTRIBUTIONS (PART I)

**LONG-LIVED RADIONUCLIDES IN
BIOLOGICAL SYSTEMS**

Sorption of U(VI) and Np(V) on bacteriogenic Fe(III) oxyhydroxides from the Äspö Hard Rock Laboratory, Sweden

E. Krawczyk-Bärsch, K. Schmeide

At the Äspö Hard Rock Laboratory (Sweden), *Gallionella ferruginea* dominated biofilms associated with bacteriogenic iron oxides (BIOS) and groundwater were sampled from an in situ continuous flow cell which has been installed in a cavity of the main access tunnel at 2200 A site, 300 m below sea level [1]. In laboratory sorption experiments, $\text{UO}_2(\text{ClO}_4)_2$ and NpO_2ClO_4 were added to the BIOS biofilms in groundwater under aerobic conditions adjusting a final concentration of 1.9×10^{-5} M U(VI) and 3.27×10^{-5} M Np(V). At the end of the experiments, the groundwater/BIOS biofilm samples were ultra-centrifuged and analyzed. The analysis showed a substantial decrease of U and Np in the groundwater of approximately 85% and 95%, respectively.

The ferrous iron-oxidizing and stalk-forming bacterium *Gallionella ferruginea* is dominating the sorption process in the BIOS biofilm. The stalk represents an organic surface upon which Fe(III) oxyhydroxides can precipitate. Due to the high concentration of ferric iron in the BIOS biofilm, the portion of iron oxyhydroxides (ferrihydrite) amounts approximately to 70 wt-%. Under the given pH conditions, the uptake of U and Np depends predominantly on the high amount of ferrihydrite precipitated onto the stalks. Conclusively, the combination of this biological material and iron oxides creates an abundant surface area for adsorption of radionuclides.

EXPERIMENTAL. During the sampling campaign, BIOS biofilms and groundwater were removed from the flow cell located in a cavity of the main access tunnel at 2200 A site. Laboratory sorption experiments were performed under aerobic conditions. Two 50 mL tubes were each filled with 20 mL groundwater, including BIOS biofilms (0.25 g dry mass). $\text{UO}_2(\text{ClO}_4)_2$ was added to the suspension in the first tube, adjusting a final U(VI) concentration of 1.9×10^{-5} M (4500 $\mu\text{g/L}$). The suspension of the second tube was exposed to NpO_2ClO_4 to adjust a final Np(V) concentration of 3.27×10^{-5} M (7680 $\mu\text{g/L}$). After 20 days, the suspensions were centrifuged, and the supernatants were used for analysis. The samples were acidified and analyzed for cation determination by means of ICP-MS. The initial and final Np(V) concentration in solution was determined by liquid scintillation counting using α - β discrimination. For this, 100 μL of the supernatant was mixed with 5 mL of an Ultima Gold™ scintillation cocktail. The anions were determined by means of ion chromatography (IC).

RESULTS. The results show a substantial removal of U(VI) and Np(V) from the groundwater of approximately 85% and 95%, respectively. It can be assumed that the uptake depends predominantly on the amount of iron oxyhydroxides precipitated onto the stalks of *Gallionella ferruginea*. However, the precipitation of iron oxide on the surface of bacteria depends on the total supply of dissolved ferric iron and the availability of reactive sorption sites (i.e. carboxyl or phosphoryl groups) on the individual cells [2]. As reported in [1], up to 90 wt-% iron oxyhydroxides can be formed on the extracellular stalk material.

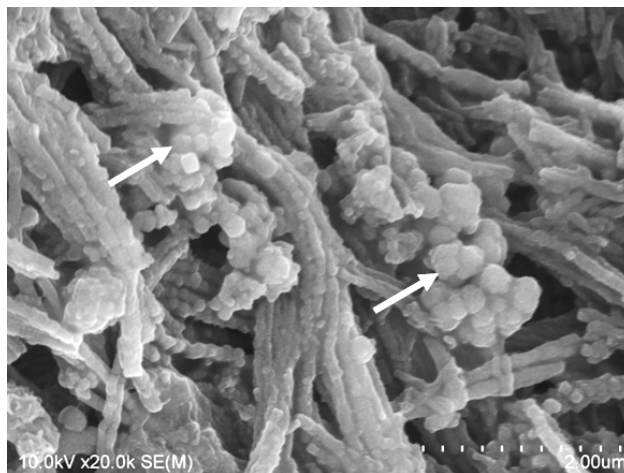


Fig. 1: SEM picture showing coatings of fine-grained iron-oxide precipitates (marked by white arrows) in the BIOS biofilms from Äspö HRL.

Due to the amount of ferric iron in the BIOS biofilm of our study, we assume that the portion of iron oxyhydroxides amounts to approximately 70 wt-%. The residual mass must be derived mostly from bacterial organic matter. Results obtained by powder X-ray diffraction of the dried BIOS biofilm clearly indicate the presence of a two-line ferrihydrite. As known from several studies [3,4], the sorption of U(VI) onto ferrihydrite between pH 5.4 and 8.2 can reach 95–99% in carbonate-free solution systems. The presence of the bacteriogenic iron-producing microbial community in the fracture water results in a high rate of iron precipitation, which is 60 times faster than iron precipitation in an abiotic system [5]. The combination of iron oxides and the biological material creates an abundant surface area for adsorption. Consequently, radionuclides which are not adsorbed by iron oxyhydroxides present in fractures will be immobilized by BIOS biofilms.

ACKNOWLEDGEMENTS. The research leading to these results has received funding from Euratom 7th Framework Programme FP7/2007-2011 under grant agreement n° 269658 (CROCK project). We thank Birgitta Kalinowski (SKB, Sweden) for her cooperation in biofilm and water sampling.

- [1] Anderson, C.R. et al. (2003) *Geobiology* **1**, 169–178.
- [2] Konhauser, K.O. (1997) *FEMS Microbiol. Rev.* **20**, 315–326.
- [3] Waite, T.D. et al. (1994) *Geochim. Cosmochim. Acta* **58**, 5465–5478.
- [4] Payne, T.E. et al. (1998) in: *Sorption of Metals by Geomediation*, pp. 75–97, Academic Press.
- [5] Sögaard E.G. et al. (2000) *Water Research* **34**, 2675–2682.

Laser fluorescence lifetime of uranyl species onto *Euglena mutabilis* determined with single photon avalanche diode and a multichannel event timer

N. Baumann, T. Arnold

Lifetime from the fluorescence of uranyl species onto *Euglena mutabilis* suspended in a water solution at pH 3 was measured. For the separation of the intensive, unwanted, and short living fluorescence, caused by organic substances from the interesting fluorescence of the uranyl species, a quasi-pulsing laser excitation was created from an 80 MHz MaiTai laser by periodic diffraction from the excitation beam. Fluorescence photons were detected with a Single Photon Avalanche Diode (SPAD) and evaluated by a multichannel event timer (HydraHarp).

Euglena mutabilis belongs to unicellular flagellate protists. Euglenoids are often used in laboratory as model organism. They are abundant in many inland waters and in particular *Euglena mutabilis* is often observed in environments with low pH values and high metal concentrations as in acid mine drainage (AMD) regions. Due to technical leaching of uranium ores with sulfuric acid AMD environments are found related to former mining and milling sites [1], also on the WISMUT uranium mining heap contact area "Gessenwiese" close to Ronneburg (Thuringia) [2]. The influence of *Euglena mutabilis* on the transport behavior of uranium in such AMD, environments is so far not understood. In this study, laser fluorescence life time of uranyl species immobilized by living, i.e. metabolically active *Euglena mutabilis* was measured for getting information regarding the binding form of respective species. For that measurement the so called Time-Correlated Single Photon Counting (TCSPC) method was used for the first time.

Laser induced fluorescence caused by organic substances like chlorophyll in general has a much shorter lifetime than the fluorescence caused by heavy metal ions, and is often very intensive. In case of quasi continuous laser excitation as supplied by the 80 MHz MaiTai HP laser, this unwanted and intensive fluorescence from organic substances is permanent present and so continuously covers up the interesting metal fluorescence. That's why the quasi continuous laser excitation was transformed to quasi pulsed excitation as described below.

EXPERIMENTAL. For achieving a pulsing laser excitation beam, the 80 MHz laser beam from the MaiTai HP laser was periodically interrupted by an alternated diffraction of the beam with an adjustable acousto-optic modulator (AOM, APE Berlin). The AOM is a TeO₂-crystal which can be alternately set in oscillation by an alternating applying HF voltage of approximately 100 MHz. In the vibrational status, the crystal diffracts the laser beam during transmitting the crystal.

AOM, SPAD and HydraHarp were coordinated and synchronized by delay generators. The correct timing of the quasi-pulsing from the excitation laser beam was controlled and visualized by using a photo diode and an oscillograph. The AOM was triggered with 100 kHz, one laser excitation spans 2000 ns, afterwards the SPAD detects the fluorescence photons within 8000 ns. The amplified fluorescence photons were chronologically ordered in a TCSPC histogram between periodic excitation by the HydraHarp. For drawing the life time curve and calculating

the life times, the software package SymPhoTime (PicoQuant Berlin) was applied. The accuracy control of the complex life time measuring system was made with a reference solution of 5×10^{-5} M uranium perchlorate ($T = 1.95 \pm 0.05 \mu\text{s}$, $n = 7$).

As a first attempt, the measurement was made by separating the short living, but intensive and unwanted, fluorescence originated from organic substances like chlorophyll, from the longer living and interesting fluorescence caused from heavy and radioactive metal ion species like uranium (VI) species, via their different life times. *Euglena mutabilis* were in contact with a 10^{-5} M uranium perchlorate solution at pH 3 for 5 days, after that the *Euglena mutabilis* were separated from the uranium solution by a centrifuge and then stirred up again within a perchlorate solution with the same pH value. The measurement was made with permanently stirring the *Euglena mutabilis* suspension in a quartz glass cuvette.

RESULTS. The bi-exponential decay of the bulk fluorescence signal revealed that fluorescence is composed of a very short living part and a longer living content. The short living part is interpreted as originated from organic substances e.g. chlorophyll or protein, the longer living part of >10000 ns is interpreted as originated from the uranyl species onto of the *Euglena mutabilis* cells. Previously carried out investigations on *Euglena mutabilis* cells in contact with uranium [1] have shown that uranium is coordinated with carboxyl and/or with phosphate groups, a distinction was not possible. Our results indicate that uranium - because of the long fluorescence lifetime of $>10 \mu\text{s}$ [3] - is more likely coordinated to phosphate.

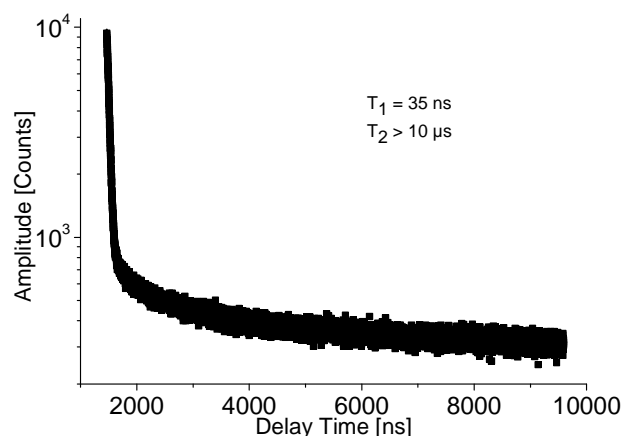


Fig. 1: Life time curve from the fluorescence signal from euglena mutabilis suspension gained by a HydraHarp and SymPho Time software package.

ACKNOWLEDGEMENTS. Authors are grateful to S. Brockmann for preparing *Euglena mutabilis* suspensions, and BMBF project no. 02NUK015F for financial support.

- [1] Brockmann, S. et al. (2014) *Radiochim. Acta*, accepted.
- [2] Baumann, N. et al. (2014) *Environ. Sci. Pollut. Res.*, in press.
- [3] Baumann, N. et al. (2008) *Environ. Sci. Technol.* **42**, 8266–8269.

Cultivation of microorganisms live in the mine water of the former uranium mine Königstein, Germany

I. Zirnstein, S. Köppchen, I. Röske,¹ T. Arnold

¹Institute of Applied Microbiology, TU Dresden, Dresden, Germany

Using different nutrient solutions under different conditions (e.g. temperature, pH, chemical composition of culture media), microorganisms from mine water of the uranium mine Königstein were cultured and isolated. Iron-oxidizing and sulfur oxidizing bacteria are dominating the cultures. Some of them were chosen to check their uranium tolerance. It was found that the eukaryotic species *Rhodospiridium toruloides* were grown on culture media with up to 6 mM $\text{UO}_2(\text{NO}_3)_2$.

Microbes affect the mobility of actinides [1]. Microorganisms from sites of former uranium mining areas have to be investigated regarding their interaction mechanisms with soluble actinides. The mine water from former uranium mine Königstein has been used to isolate different microbial strains.

EXPERIMENTAL. For determining the cell number of metabolic active microorganisms (LZZ) in the mine water the colonies (KbE) on different culture media were counted. For cultivation, different plate-count-agar-media (PCA) and different conditions were tested: plate-count-agar and Königstein-plate-count-agar (sterile Königstein mine water instead of MilliQ). The media differ in pH 2 or 7, carbon source: glucose or yeast extract, temperature: 28 °C or 45 °C, oxygen: aerob or anaerob. Additionally, specific culture solutions for metabolic groups (e.g. sulfur-oxidizing bacteria, iron-oxidizing bacteria, sulfate-reducing bacteria, arsenic-tolerant bacteria, manganese-tolerant bacteria) were used. Uranium tolerance of some isolates were tested by plating isolates on PCA with pH 7 and uranium concentrations from 0.5 to 10 mM $\text{UO}_2(\text{NO}_3)_2$.

RESULTS. The Königstein mine water contains 5.2×10^5 cells/mL including all microbial cells – living and dead. For determination of metabolic active microorganisms, up to 4.8×10^2 KbE/mL were analyzed at anaerobic conditions and up to 3.3×10^3 KbE/mL mine water had grown aerobic.

The Königstein mine water is dominated by bacteria e.g. *Acidithiobacillus sp.*, *Acidocella sp.*, *Thiomonas sp.*, *Acidiphilium sp.*, analyzed by molecular genetic methods (16S rDNA PCR, pyrosequencing). Almost all dominant bacteria were isolated and cultured in the lab (see Tab. 1). The most culture media were populated by the iron-oxidizing bacteria *Acidithiobacillus ferrooxidans*. In addition to different bacteria species, eukaryotes esp. fungi and yeasts could isolate. One eukaryotic representative called *Rhodospiridium toruloides* has grown on agar plates in the presence of 6 mM $\text{UO}_2(\text{NO}_3)_2$. After cell lysis of the yeast, a uranium concentration of 1.7 mg uranium/g_{cell dry mass} were measured inside the cells by ICP-MS analyses. This result is supported by scanning electron microscopy (SEM) measurements. SEM pictures of *Rhodospiridium toruloides* cells obtained from a uranium culture medium showed regions with high contrast in the cells which were attributed to elements of high atomic weight. EDX measurements of these regions identified uranium in or at the yeast cells (data not shown).

Tab. 1: The microbial species, that were isolated from former uranium mine water with the uranium concentration, they tolerate at different nutrient solutions.

Species	Uranium tolerance
Iron-oxidizing bacteria	
<i>Acidocella sp.</i>	–
<i>Acidithiobacillus ferrooxidans</i>	≤ 0.5 mM
Iron-reducing bacteria	
<i>Acidiphilium sp.</i>	–
Sulfur-oxidizing bacteria	
<i>Thiomonas arsenivorans</i>	–
<i>Sulfobacillus sp.</i>	≤ 2 mM
<i>Acidithiobacillus thiooxidans</i>	–
<i>Thiomonas cuprina</i>	≤ 0.5 mM
<i>Thiomonas sp.</i>	≤ 1 mM
Methylophilic bacteria	
<i>Methylobacterium sp.</i>	≤ 1 mM
Other bacteria	
<i>Arthrobacter sp.</i>	≤ 1 mM
<i>Streptomyces sp.</i>	–
<i>Sediminibacterium sp.</i>	–
<i>Bacillus licheniformis</i>	–
<i>Paenibacillus sp.</i>	≤ 1 mM
<i>Mycobacterium sp.</i>	≤ 0.5 mM
unclassified bacteria	≤ 2 mM
Eukaryotes	
<i>Rhodospiridium toruloides</i>	≤ 6 mM
<i>Exophilia sp.</i>	–
unclassified yeasts/fungi	≤ 1 mM

ACKNOWLEDGEMENTS. This work was supported by the Bundesministerium für Bildung und Forschung (BMBF), Project No 02NUK015F. The authors are grateful to A. Ritter for ICP-MS measurements and E. Christalle for SEM/EDX analyses. Thanks to S. Röder from Wismut GmbH to take samples.

[1] Gadd, G. M. (2010) *Microbiology* **156**, 609–643.

Microbial community analysis of mine water from three abandoned uranium mines in East Germany

C. Gagell, T. Arnold, U. Jenk,¹ K. Röske,² I. Röske³

¹Wismut GmbH, Chemnitz, Germany; ²Institute of Medical Microbiology and Hygiene, TU Dresden, Dresden, Germany; ³Institute of Microbiology, TU Dresden, Dresden, Germany

The mine water of three abandoned, underground uranium mines (Pöhla, Schlema, Zobes) in East Germany was analyzed regarding microbial community structure by pyrosequencing. Despite of different remediation stages and water chemistry of the investigated mines, similar microbial groups were identified. The microbial communities are mainly dominated by sulphur-oxidizing members of Beta- and Epsilonproteobacteria. However, biofilm samples from the mine waters show a different community structure.

EXPERIMENTAL. 10 L mine water was vacuum filtrated through a 0.2 µm cellulose acetate membrane, and mine biofilm was cultivated for three month in situ on activated carbon carrier. The total DNA of the samples was extracted by means of the PowerWater[®] DNA Isolation Kit (MoBio) according to manufacturer's instructions and an optimized phenol/chloroform extraction, respectively. For identification of bacteria, the V3-V4 region of the 16S rRNA gene was amplified using a barcoded U341F primer (5'-xxxxxx-CCTACGGGGRSGCAGCAG-3', [1]) and R4 primer (5'-TACNVGGGTATCTAATC-3', [2]). The resulting amplicons were analyzed by agarose gel electrophoresis, purified and sequenced using the GS FLX Titanium series chemistry by Eurofins MWG Operon (Germany). The analysis of the sequences was performed by the software package MOTHUR 1.15.0 [3].

RESULTS. The pyrosequencing approach for the identification of bacteria yielded in total 10984, 521, 12459, 322, 9097 and 247 sequences for Pöhla mine water (PMW), Pöhla mine biofilm (PMB), Schlema mine water (SMW), Schlema mine biofilm (SMB), Zobes mine water (ZMW) and Zobes mine biofilm (ZMB), respectively. The quality checked sequences were grouped into 29, 12, 27, 14, 32 and 17 bacterial classes for PMW, PMB, SMW, SMB, ZMW and ZMB, respectively. However, as shown in Fig. 1, the microbial communities of the mine waters were dominated by only two classes, Beta- and Epsilonproteobacteria. High sequence homologies were found for *Sulfuritalea* belonging to the Betaproteobacteria, *Sulfuricurvum* and *Sulfurimonas*, members of the Epsilonproteobacteria. These bacteria have been found in deep-sea hydrothermal fields where they oxidize reduced sulphur compounds [4,5]. Further, sequences representing methane-metabolizing Gammaproteobacteria, e.g. *Methylomonas* and *Methylobacter*, were detected. A different bacterial community was found for the mine biofilms. Instead of Beta- and Epsilonproteobacteria, the Deltaproteobacteria became the dominant class. The subclassification on genus level is difficult. The deltaproteobacterial sequences show homologies (although only low with 26%) to the genus *Desulfocapsa* and *Geobacter* (for ZMB). In general, the members of the Deltaproteobacteria show a high metabolic diversity including sulphate-reducing (e.g. *Desulfocapsa*) and iron- and uranium-reducing bacteria such as *Geobacter*. It is therefore tempting to speculate that the investigated mine biofilms could be involved in uranium reduction/immobilization under

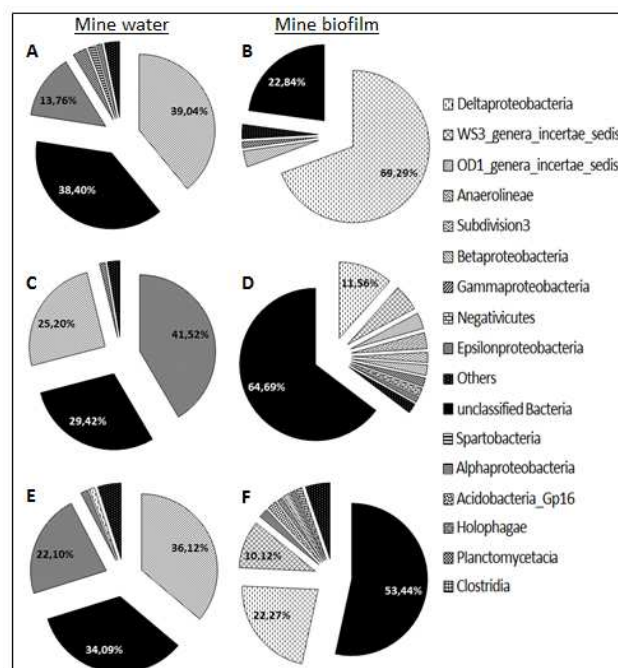


Fig. 1: Bacterial communities of water and biofilms of flooded underground uranium mines. Diagrams show the relative distribution of bacterial classes based on 16S rRNA gene analysis by pyrosequencing. A, C and E show results for Pöhla, Schlema and Zobes mine water, respectively. B, D, and F represent results for Pöhla, Schlema and Zobes mine biofilm, respectively.

natural conditions. However, the interaction of uranium with the mine biofilms has to be investigated.

- [1] Hansen, M.C. et al. (1998) *FEMS Microbiol. Ecol.* **26**, 141–149.
- [2] Zhang, T. et al. (2012) *ISME J.* **6**, 1137–1147.
- [3] Schloss, P.D. et al. (2009) *Appl. Environ. Microbiol.* **75**, 7537–7541.
- [4] Nagawa, S. et al. (2005) *Environ. Microbiol.*, **7**, 1619–1632.
- [5] Akerman, N.H. et al. (2013) *Front. Microbiol.* **4**, 185.

First insight into the impact of microorganisms on uranium sorption on selected minerals

C. Richter, K. Großmann, V. Brendler, C. Gagell

Investigations on quartz, orthoclase and muscovite proved that these natural minerals contain microorganisms. They can influence the sorption behavior of heavy metals onto the mineral surfaces. In this context it is important to analyze sorption data to estimate the influence of microorganisms. If necessary, pre-treatment of the minerals can minimize these effects to a significant degree.

EXPERIMENTAL. To stimulate bacterial growth 0.2 g of quartz (Q), orthoclase (O) and muscovite (M) were transferred into 15 mL tubes and incubated in 10 mL of two different culture media: standard NB and R2A medium [1]. All experiments were performed as triplicates. The measurement of the optical density at 600 nm (OD_{600}) at two time steps allowed monitoring the growth of microorganisms. To prepare the samples for the measurement, they were shaken and after sedimentation (30 s) 1 mL of the supernatant was transferred to a cuvette. The first measurement was done directly after adding the culture media to the mineral. The second measurement was performed after three weeks of incubation. In the meantime, the samples were shaken at 30 °C to promote the growth of microorganisms. The cuvettes were placed into a UV-vis spectrophotometer (Ultrospe 1000, Pharmacia Biotech) and the OD_{600} was measured. Samples with culture medium but without mineral were set as references. To investigate how these microorganisms influence the uranium sorption, batch experiments were performed under various growth-inhibiting conditions (see Fig. 1). There, 0.5 g mineral were suspended in 10 mL $NaClO_4$ and pH was adjusted to 7. After three months of equilibration, uranium(VI) (10^{-6} M) was added and sorbed for one week. Afterwards the samples were centrifuged at $2800 \times g$ for one hour and 1 mL of the supernatant of each sample was analyzed by ICP-MS.

RESULTS. The determined optical density for the minerals in both culture media is shown in Tab. 1. It also gives the difference in OD_{600} (ΔOD) between start (OD_0) and an incubation time of 3 weeks (OD_{3w}) which served as a measure of the growth of microorganisms. For all three minerals, the samples show an increase in OD with time. These results indicate that both (very different) nutrient conditions favored the growth of microorganisms attached to the mineral samples. For orthoclase the increase in OD is lower than for quartz or muscovite. Probably, the microorganisms on orthoclase are less cultivable than on the other minerals. Both culture media deliver different nutri-

ents, thus promoting the growth of different microbial species. This may explain the differences between the OD values for the same mineral in both culture media. Moreover, the samples were also used for cultivation on agar plates (prepared from the culture media). This experiment confirmed the results based on OD. For all minerals, cultivable microorganisms can be observed as colonies, again with smaller populations on orthoclase compared to quartz and muscovite. These results show that typically microorganisms will be present during experiments with natural mineral. For that reason the minerals have to be pre-treated (for details see Yan et al. [2]), e.g. by autoclaving. Alternatively, the effect of microorganisms has to be kept in mind for interpreting the results.

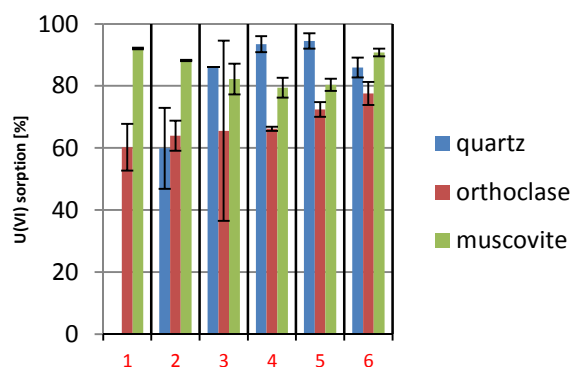


Fig. 1: U(VI) sorption according to the influence of microorganisms.
 1 not autoclaved, daylight (reference case);
 2 not autoclaved, darkness;
 3 autoclaved, darkness;
 4 autoclaved, Laminar flow box, daylight;
 5 autoclaved, Laminar flow box, darkness;
 6 not autoclaved, sodium azide added.

The results of the batch experiments indicate that the various treatments clearly affect the microbial influence on uranium sorption (Fig. 1). In the case of orthoclase, the biggest change is induced by the sodium azide treatment. In case of quartz, the use of laminar boxes has the largest consequences. But in both cases the changes have the same direction: destroying the microbes also stops them actively suppressing uranium sorption. In case of muscovite, the combination of laminar flow box, autoclaving and darkness effects sorption the most – but in the opposite direction. Here, the microbes obviously enhance sorption (dead or alive).

These findings show again that on the three investigated minerals different microorganisms are present, and that their effect is difficult to predict. Thus, a separate investigation of microbial effects is recommended for each mineral. In addition, any autoclaving may directly change the mineral surface, e.g. by creating new or altering existing sorption sites.

Tab. 1: Optical Density OD_{600} of samples with quartz, orthoclase and muscovite in a NB and R2A culture medium.

mineral	OD_0 (t = 0)	OD_{3w} (t = 3 weeks)	ΔOD^*
quartz	0.002 ± 0.002	0.681 ± 0.131	0.68 ± 0.13
NB orthoclase	0.021 ± 0.002	0.145 ± 0.132	0.12 ± 0.13
NB muscovite	0.278 ± 0.003	0.710 ± 0.155	0.43 ± 0.16
quartz	0.003 ± 0.002	0.416 ± 0.234	0.41 ± 0.24
R2A orthoclase	0.014 ± 0.004	0.371 ± 0.255	0.36 ± 0.25
R2A muscovite	0.253 ± 0.025	1.014 ± 0.269	0.76 ± 0.26

* $OD_{3w} - OD_0$.

[1] Foght, J. et al. (2005) in: *Monitoring and Assessing Soil Bioremediation. Soil Biology Vol. 5*, p. 261–280, Springer, Berlin.
 [2] Yan, G. et al. (2000) *Water SA*, **26**, 119–123.

The impact of the Opalinus clay isolate *Sporomusa* sp. MT-2.99 on the U(VI) speciation

L. Lütke,¹ H. Moll, V. Bachvarova,² S. Selenska-Pobell, G. Bernhard

¹Institut für Radioökologie und Strahlenschutz (IRS), Leibniz Universität Hannover, Hannover, Germany; ²Department of Developmental Biology / Center for Medical Biotechnology, University of Duisburg-Essen, Germany

Potentiometric titration in combination with Time-resolved Laser-induced Fluorescence Spectroscopy (TRLFS) was employed to study the binding of U(VI) onto cells of the novel Mont Terri isolate *Sporomusa* sp. MT-2.99 with respect to the U(VI) surface complexes formed and their stability constants.

Among the prominent processes influencing the actinide migration, there is growing attention to the influence of indigenous microorganisms. The investigated bacterial strain, *Sporomusa* sp. MT-2.99, has been isolated recently from Opalinus clay core samples collected from a borehole of the Mont Terri URL, Switzerland [1].

EXPERIMENTAL. *Sporomusa* sp. MT-2.99 was cultured anaerobically in R2A medium at 30 °C. Culture purity was ensured by light microscopy and *in situ* PCR with subsequent RFLP. Potentiometric titration was employed to characterize the bacterial surface functional groups and formed U(VI) complexes. HYPERQUAD analysis [2] was performed to determine the respective pK_a values and stability constants as described previously [3]. TRLFS was used for verification of the pH-dependent U(VI) speciation at the cell surface, for details see [4].

RESULTS. For evaluation of the potentiometry data a commonly applied three-site model was used to model the cell surface functional groups. The analysis yielded the following pK_a values (densities in mmol/g_{dry weight}): 4.80 ± 0.06 (0.53 ± 0.08 mmol/g_{dry weight}), 6.68 ± 0.06 (0.35 ± 0.03 mmol/g_{dry weight}), and 9.01 ± 0.08 (0.48 ± 0.05 mmol/g_{dry weight}). The respective surface functional groups are attributable to carboxyl, phosphate and amine moieties [5]. The titration curve of U(VI) and cells and the HYPERQUAD fit is shown in Fig. 1.

The fit was based on the pK_a values and site densities of the bacteria and the log β values of relevant uranyl hydrolytic species. Extracted U(VI) surface complexes and stability constants using HYPERQUAD are given in Tab. 1. The determined stability constants indicate that U(VI) is coordinated by the surface functional groups with moderate to high thermodynamic stability. Based on these constants the pH-dependent U(VI) species distribution in

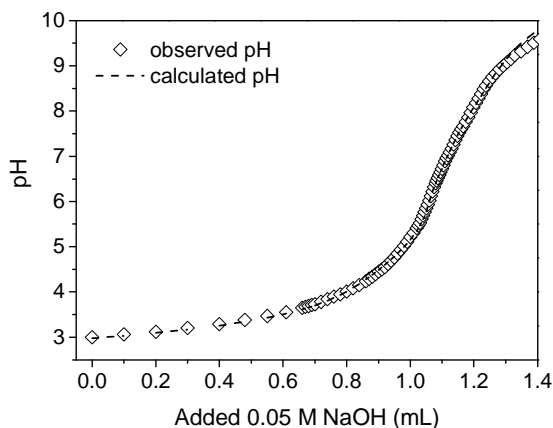


Fig. 1: Titration of 1×10^{-4} M UO_2^{2+} and 0.3 g/L cells in 0.1 M NaClO_4 with 0.05 M NaOH under N_2 atmosphere. Data (\diamond), fit (---).

Tab. 1: Calculated U(VI) surface complexes and stability constants.

Complex	xyz*	log β (± SD)
R-COO-UO ₂ ⁺	110	4.75 ± 0.98
R-O-PO ₃ -UO ₂	110	8.58 ± 0.04
R-O-PO ₃ H-UO ₂ ⁺	111	13.07 ± 0.06
(R-O-PO ₃) ₂ -UO ₂ ²⁻	120	13.30 ± 0.09

*: ratio metal : ligand : proton.

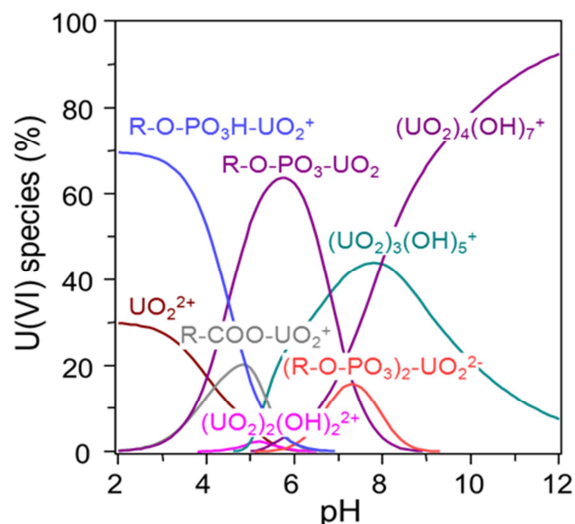


Fig. 2: U(VI) species distribution in presence of *Sporomusa* sp. cells in dependence on pH. $[\text{U(VI)}] = 1 \times 10^{-4}$ M, $[\text{dry biomass}] = 0.2$ g/L. CO_2 -free system.

presence of the bacteria using environmentally relevant concentrations was calculated with HySS 2009 (Fig. 2). The pH-dependent U(VI) speciation in presence of the cells shows that in the acidic pH range U(VI) is primarily coordinated by protonated phosphoryl surface groups. In the neutral pH range (pH 6–7), U(VI) is mainly bound via deprotonated phosphoryl sites. Using TRLFS the different phosphoryl complexes were distinguishable by their different lifetimes and appearance in dependency on pH. Like it was found for *P. fluorescens* [3] with 2.31 μs the R-O-PO₃H-UO₂⁺ complex has a significantly longer lifetime than the corresponding deprotonated complex with 0.27 μs. To validate the apparent minor influence of carboxylic site coordination further data analysis needs to be done since the respective complex stability constant shows quite a high standard deviation.

ACKNOWLEDGEMENTS. The authors thank the BMWi for financial support (contract no.: 02E10618) and the BGR for providing the clay samples.

- [1] Bachvarova, V. et al. (2009) *Report FZD-530*, p. 18.
 [2] Gans, P. et al. (1996) *Talanta* **43**, 1739–1753.
 [3] Lütke, L. et al. (2012) *Dalton Trans.* **41**, 13370–13378.
 [4] Lütke, L. et al. (2013) *Dalton Trans.* **42**, 6979–6988.
 [5] Cox, J. S. et al. (1999) *Environ. Sci. Technol.* **33**, 4514–4521.

Cm(III)/Eu(III) speciation studies with the Opalinus clay isolate *Sporomusa* sp. MT-2.99

H. Moll, L. Lütke,¹ V. Bachvarova,² A. Cherkouk, S. Selenska-Pobell, G. Bernhard

¹Institut für Radioökologie und Strahlenschutz (IRS), Leibniz Universität Hannover, Hannover, Germany; ²Department of Developmental Biology / Center for Medical Biotechnology, University of Duisburg-Essen, Germany

In this work, we demonstrate that the binding of Cm(III) and Eu(III) ions to the *Sporomusa* sp. cell wall occurs via hydrogen phosphoryl, carboxyl and deprotonated phosphoryl groups. This result was achieved by the use of time-resolved laser-induced fluorescence spectroscopy (TRLFS) and potentiometric titrations.

The unknown speciation of Cm(III)/Eu(III) with cells of *Sporomusa* sp. MT-2.99 was systematically analyzed by TRLFS and potentiometric titrations (for Eu³⁺) [1]. The strain of the Gram-negative genus *Sporomusa* was recently isolated from Opalinus clay core samples collected from a borehole of the Mont Terri URL, Switzerland [2]. The provided stability constants of Cm(III)/Eu(III) complexes with bacterial surface functional groups can be used to model their speciation for instance in the vicinity of a nuclear waste repository.

EXPERIMENTAL. *Sporomusa* sp. MT-2.99 cells were cultured anaerobically in R2A medium at 30 °C. TRLFS measurements were performed under N₂ atmosphere in 0.1 M NaClO₄ at 25 °C. The Cm(III)/Eu(III) speciation change was investigated at different biomass concentrations as a function of pH. Experimental details about the laser system can be found in [3]. The titrations were carried out under N₂ atmosphere. CO₂-free 0.05 M NaOH was used as titrant. Titration curves were evaluated using the program HYPERQUAD 2008 [4].

RESULTS. The titration curve of solely *Sporomusa* sp. cells was successfully fitted with a three-site model with HYPERQUAD (Fig. 1). The respective surface functional groups can be attributed to carboxyl, phosphate and amine moieties. The calculated pK_a values and site densities of the binding sites are summarized in [5].

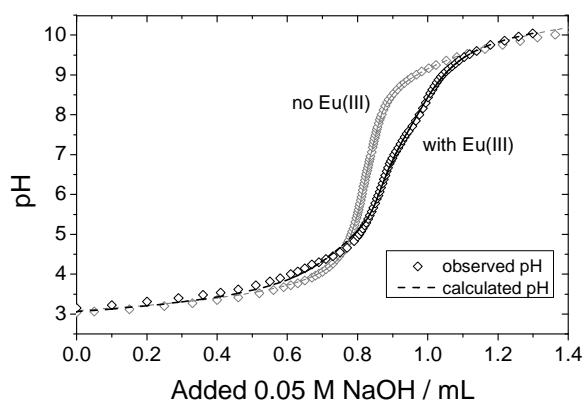


Fig. 1: Titration of 300 mg_{dry weight}/L cells in the absence and presence of 100 μM Eu³⁺ in 0.1 M NaCl titrated with 0.05 M NaOH and fit.

The Eu(III) titration curve could be modeled with a very good fit result when the bacterial surface complexes R-COO-Eu²⁺, R-O-PO₃H-Eu²⁺, and R-O-PO₃-Eu⁺ were considered (see Fig. 1). The respective calculated stability constants are summarized in Table 1.

In addition to potentiometric titrations, Cm(III)/Eu(III) TRLFS measurements were performed. The dependencies found in the TRLFS spectra shown in Fig. 2 suggested the occurrence of two individual Cm³⁺-*Sporomusa* sp. spe-

Tab. 1: Calculated Cm(III)/Eu(III) surface complexes and stability constants.

Complex	xyz ^a	log β
R-COO-Cm ²⁺	110	8.06 ± 0.61 ^b
R-O-PO ₃ H-Cm ²⁺	111	13.90 ± 0.90 ^b
R-COO-Eu ²⁺	110	6.66 ± 0.48 ^b
R-O-PO ₃ H-Eu ²⁺	111	13.38 ± 0.48 ^b
R-COO-Eu ⁺	110	6.89 ± 0.62 ^c
R-O-PO ₃ -Eu ⁺	110	7.71 ± 0.33 ^c
R-O-PO ₃ H-Eu ²⁺	111	15.49 ± 0.19 ^c

^a ratio metal : ligand : proton, ^b from TRLFS,

^c from potentiometric titrations.

cies between pH 1.9 and 8.1 having emission maxima at ca. 600 nm (phosphoryl bound Cm), and 601.4 nm (carboxyl bound Cm). The spectroscopic speciation determined for Cm(III) could be confirmed with Eu(III) (data not shown).

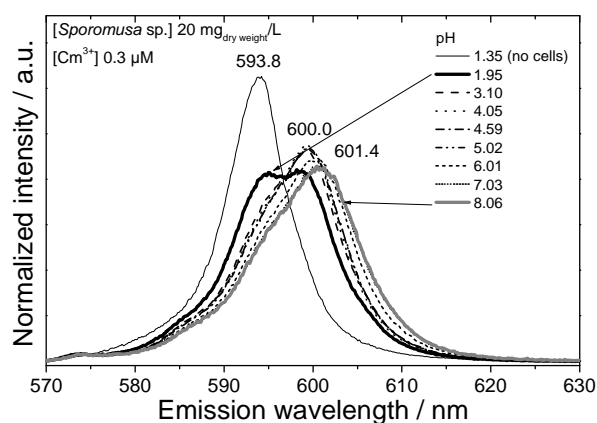


Fig. 2: Cm(III) TRLFS spectra in the *Sporomusa* sp. system as a function of pH.

Our results suggest that Eu(III)/Cm(III) complexes with the surface functional groups of the *Sporomusa* sp. cell envelope dominating their respective speciation over a broad pH and biomass concentration range. Overall, the considered surface functional groups show a moderate to strong interaction with Eu(III) and Cm(III).

ACKNOWLEDGEMENTS. This work was funded by BMWi under contract number 02E10618. The authors thank the BGR for providing the clay samples.

[1] Moll, H. et al. (2014) *Geomicrobiol. J.*, submitted.

[2] Bachvarova, V. (2009) *Report FZD-530*, p. 18.

[3] Moll, H. et al. (2008) *Biometals* **21**, 219–228.

[4] Gans P. et al. (1996) *Talanta* **43**, 1739–1753.

[5] Lütke, L. et al. (2014) this report, p. 14.

Interaction of Eu(III) with FaDu cells: Study of cell viability and Eu(III) uptake in the presence of Eu-152

S. Sachs

The impact of $^{152}\text{Eu(III)}$ on the viability of FaDu cells and on the Eu(III) uptake into the cells was studied and compared to results obtained with Eu(III) of natural isotopic composition. Results of such studies may contribute to the assessment of low dose radiation effects.

In case of the release of long-lived radionuclides, for instance actinides, into the environment, their interactions in the ecosphere may be quite diverse. The in-depth understanding of relevant processes is necessary to assess how radionuclides may affect human beings. Objective of our work is the study of interaction processes of actinides with mammalian cells. The cytotoxicity of Eu(III), as analog for trivalent actinides, onto FaDu cells (human squamous cell carcinoma cell line) and its uptake into the cells as a function of the Eu(III) concentration and speciation has already been studied [1–3]. In the present work, the differentiation between chemotoxic and radiotoxic effects of Eu(III) on FaDu cells is studied for the first time. The Eu(III) cytotoxicity onto FaDu cells is studied using ^{152}Eu (β -emitter, electron capture) and Eu in natural isotopic composition ($^{\text{nat}}\text{Eu}$) in parallel ($^{152}\text{Eu}/^{\text{nat}}\text{Eu}$). Furthermore, the $^{152}\text{Eu}/^{\text{nat}}\text{Eu}$ uptake into the cells is estimated. Results are compared to those obtained with $^{\text{nat}}\text{Eu}$.

EXPERIMENTAL. FaDu cells were grown in Dulbecco's modified eagle medium (DMEM; w/o sodium pyruvate, with stable glutamine, 4.5 g/L D-glucose; Biochrom) supplemented with 10% fetal bovine serum (FBS; Sigma), 0.7 mM non-essential amino acids, 20 mM HEPES, penicillin/streptomycin (100 U/mL/100 $\mu\text{g}/\text{mL}$), and 1 mM sodium pyruvate (all from Biochrom) as described in [1]. After subcultivation, cells were seeded in 96-well (3×10^3 cells per well) or 6-well plates (8.55×10^4 cells per well) to study the cytotoxicity of Eu(III) [1] or its uptake [3], respectively. After 48 h of incubation (37°C , 5% CO_2 , 95% rH), the nutrient medium was removed and $^{\text{nat}}\text{Eu}$ or $^{152}\text{Eu}/^{\text{nat}}\text{Eu}$ in complete cell culture medium ($[\text{Eu}]_0$: 14, 1000 μM) was added to the cells ($\text{pH } 7.43 \pm 0.02$). For preparation of these solutions, a 2×10^{-2} M EuCl_3 stock solution ($^{\text{nat}}\text{Eu}$) and a 6×10^{-4} M Eu solution spiked with ^{152}Eu (Amersham; 0.1 M HCl; 0.22 MBq/mL; $^{152}\text{Eu}/^{\text{nat}}\text{Eu}$) were applied. Aliquots of these solutions were diluted with sterile de-ionized water and complete cell culture medium to the initial Eu(III) concentrations. These solutions were sterile-filtered (0.2 μm filter; Saarstedt) and analyzed by ICP-MS or liquid scintillation counting (LSC). In all experiments with $^{152}\text{Eu}/^{\text{nat}}\text{Eu}$ the specific activity was kept constant (545 ± 37 Bq/0.1 mL). After an exposure time of 24 and 48 h, the cell viability was analyzed by the MTT (3-(4,5-dimethylthiazol-2-yl)-2,5-diphenyl tetrazolium bromide) test [4] as described in [1]. The uptake of Eu(III) into the cells was determined after 24 h of exposure. The respective cell reprocessing (cell washing, trypsinization, counting, and lysis) is described in [3]. The Eu(III) content of all solutions after cell reprocessing was analyzed by ICP-MS ($^{\text{nat}}\text{Eu}$) or LSC ($^{152}\text{Eu}/^{\text{nat}}\text{Eu}$).

RESULTS. The viability of FaDu cells after 24 and 48 h of exposure to $^{152}\text{Eu}/^{\text{nat}}\text{Eu}$ is shown in Fig. 1 in comparison to mean viability values obtained after cell exposure to $^{\text{nat}}\text{Eu}$ (present work and [1,3]). As already described in [1], the viability of FaDu cells decreases with increasing Eu(III) concentration starting at about 800 μM . Furthermore, it is slightly decreased with increasing exposure time. The same trends can be observed in the experiments with the isotopic mixture of $^{152}\text{Eu}/^{\text{nat}}\text{Eu}$. Under consideration of the experimental uncertainties, the comparison of the data shows that the Eu(III) cytotoxicity onto the cells is not significantly influenced by the presence of ^{152}Eu .

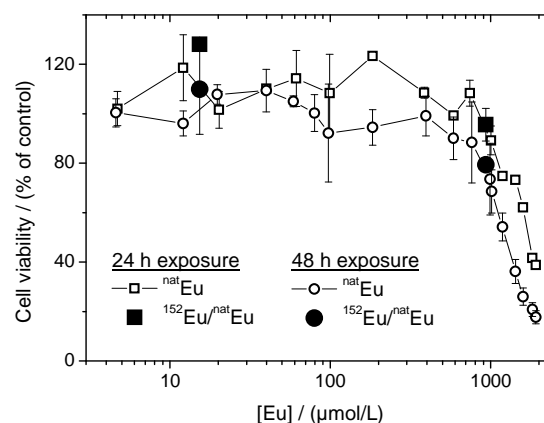


Fig. 1: Viability of FaDu cells after exposure to $^{\text{nat}}\text{Eu}$ and $^{152}\text{Eu}/^{\text{nat}}\text{Eu}$.

The Eu(III) uptake into the cells was estimated to be 0.02 ± 0.004 and 0.43 ± 0.20 nmol/ 10^6 cells after exposure to 12 and 691 μM $^{\text{nat}}\text{Eu}$, respectively, as well as 0.003 ± 0.002 and 0.71 ± 0.20 nmol/ 10^6 cells after exposure to 16 and 987 μM $^{152}\text{Eu}/^{\text{nat}}\text{Eu}$, respectively. The data obtained with the lower $[\text{Eu}]_0$ vary, which can be probably ascribed to the relatively high experimental uncertainties under the applied conditions. Under consideration of the standard deviations and the fact that the Eu(III) uptake into the cells is increased with increasing initial Eu(III) concentration [3], the uptake data obtained with the higher $[\text{Eu}]_0$ correspond to each other and those reported in [3]. Thus, the uptake of Eu(III) into the cells seems to be unaffected by the presence of ^{152}Eu .

In the presence of ^{152}Eu , no additive radiotoxic effect on the cell viability and no significant effect on the Eu(III) uptake into the cells was detectable. Thus, under the applied conditions, the radiotoxic effect of $^{152}\text{Eu(III)}$ seems to be negligible compared to the chemotoxic effect of Eu(III). However, in the presence of higher radiation doses different results may be expected as already discussed, e.g., for the impact of Np on mammalian cells [5].

ACKNOWLEDGEMENTS. The author thanks S. Heller and J. Seibt for performance of the experiments, A. Ritter for ICP-MS analyses, and A. Barkleit for LSC analysis of the $^{152}\text{Eu}/^{\text{nat}}\text{Eu}$ stock solution.

- [1] Sachs, S. et al. (2012) *Report HZDR-013*, p. 12.
- [2] Heller, A. et al. (2012) *Report HZDR-013*, p. 13.
- [3] Sachs, S. et al. (2013) *Report HZDR-030*, p. 26.
- [4] Mosmann, T. (1983) *J. Immunol. Methods* **65**, 55–63.
- [5] Boulahdour, H. (1995) *Int. J. Radiat. Biol.* **68**, 55–61.

Investigation of selenium reducing bacteria

S. Fischer, S. Fischer,¹ C. Franzen, M. Vogel, R. Steudtner, J. Raff

¹Institute of Biology, TU Dresden, Dresden, Germany

The ability of several bacteria strains to reduce toxic selenite (Se^{IV}) and selenate (Se^{VI}) to non-toxic elementary selenium (Se⁰) was investigated at high concentrations under aerobic conditions. Furthermore, the formation of selenium particles was observed.

Presently, selenium is an important technology element, has interesting photo-optical and semiconducting physical properties and is relevant for various industrial applications, e.g. for the production of solar cells, photographic exposure meters and microelectronic circuits [1,2].

In the oxic environment it forms the water-soluble oxyanions selenate [SeO₄²⁻] and selenite [SeO₃²⁻]. The reduced species Se(0), Se(-I) and Se(-II) mainly form colloidal particles or hardly soluble precipitates. Hence, it is possible to separate and recycle the reduced selenium species [3]. Beside physicochemical parameters the interactions with microorganisms influence the selenium oxidation state. It was shown, that the bacterium *Azospirillum brasilense* reduce Se(IV) to Se(0) submicron- and nanoparticles, which might be of interest for bioremediation as well as for nanobiotechnology [4].

EXPERIMENTAL. 17 gram-positive bacterial strains (*Bacillus/Lysinibacillus* sp.), which were isolated from the uranium mining waste pile “Haberland” nearby Johanngeorgenstadt (Saxony), and 16 gram-positive as well as gram-negative bacterial reference strains from the German Collection of Microorganisms and Cell Cultures (DSMZ) were cultivated overnight at 30 °C in conical flasks containing 30 mL of their respective cultivation media [5]. In the screening procedure, aliquots of pre-cultures and either Se(IV) or Se(VI) were added to fresh medium and transferred in multiwell plates, to get an OD₆₀₀ of 0.8 and a selenite/selenate concentration of 100 mM. The samples were placed in a 30 °C shaking (100 rpm) incubator for 12 days under aerobic conditions. Each screening included blank samples as control, namely Se(IV) and Se(VI) without bacteria in cultivation media. Afterwards, a reddening was optically interpreted as a first evidence for formation of Se(0) [6]. Characteristic samples were investigated by means of light microscopy.

RESULTS. After incubation for 12 days, the samples were optically analyzed whereat the red color indicates the formation of Se(0) particles. In Tab. 1 middle column, bacterial strains are listed which showed a reddening within 4 to 6 days after inoculation with Se(IV). Some of

Tab. 1: Several results screening bacteria strains with 100 mM Se(IV) and Se(VI).

Name of bacteria strain	Se(IV)	Se(VI)
JG-A12	++	-
JG-A13	+	-
JG-B5T	++	(+) ?
JG-MM-7B	++	-
JG-B7	++	-
JG-B41	+	-
JG-B62	+	-
JG-C30	++	-
<i>Shewanella oneidensis</i> (MR 1)	+	-

++ definite reddening, + slight reddening, - no definite reddening.

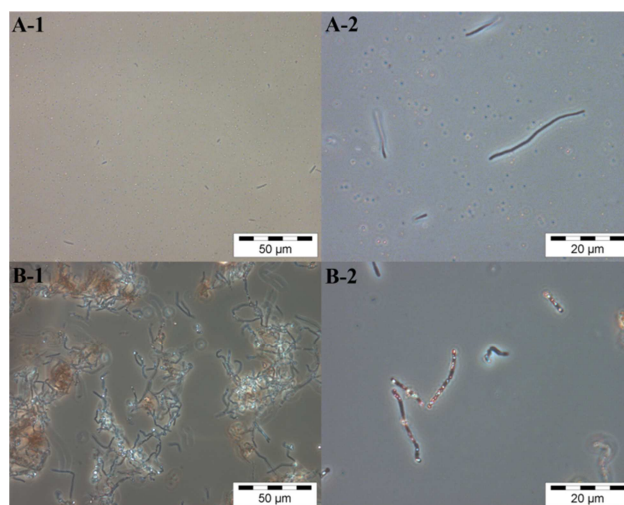


Fig. 1: Light microscopic pictures of JG-B5T (A-1 & A-2) and JG-B41 (B-1 & B-2) after incubation with 100 mM Se(IV).

the strains investigated showed only a slight reddening after 11 days.

Light microscopic pictures of two bacterial isolates JG-B5T (A-1 & A-2) and JG-B41 (B-1 & B-2), recorded 12 days after incubation of 100 mM Se(IV), indicate the formation of Se(0) submicron- or nanoparticles in the samples of JG-B5T whereas larger Se(0) precipitates seem to be formed in case of JG-B41 (Fig. 1). Probably different pathways exist for the reduction of Se(IV) depending on the bacteria strain. This will be investigated in the future.

In case of Se(VI), only the bacterial isolate JG-B5T showed a very slight reddening after 6 days under aerobic conditions (Tab. 1, right column). Further investigations are necessary to verify this observation. The other bacterial strains show normal growth in presence of Se(VI). However, they are obviously not able to reduce Se(VI) to Se(0) because a reddening of the samples was not observed.

CONCLUSION. The present study shows that microorganisms are able to reduce or tolerate soluble selenium oxyanions in concentrations up to 100 mM under aerobic conditions. In the next steps three to four of these strains will be analyzed in detail regarding their interaction with Se(IV) as well as Se(VI). Additionally, formed Se(0) particles will be characterized in detail.

This work probably helps to further close the cycle of matter of selenium which will in turn improve the production of raw materials for industry and technology as well as to reduce water pollution.

ACKNOWLEDGEMENTS. Thanks to Sabine Matys for providing some bacterial strains.

[1] Oremland, R. S. et al. (2004) *Appl. Environ. Microbiol.* **70**, 52–60.

[2] Dhanjal, S. et al. (2010) *Microb. Cell Fact.* **9**, 52.

[3] Fernandez-Martinez, A. et al. (2009) *Rev. Environ. Sci. Biotechnol.* **8**, 81–110.

[4] Steudtner, R. et al. (2012) *HZDR Report-030*, p. 25.

[5] Assumed from the Leibniz Institute DSMZ – German Collection of Microorganisms and Cell Cultures.

[6] Hunter, W. et al. (2009) *Curr. Microbiol.* **58**, 493–498.

Encapsulation of *Bacillus* sp. B5T in sol-gel ceramics

M. Vogel, A. Pannier,¹ U. Soltmann,¹ J. Raff, K. Pollmann²

¹GMBU e.V., Dresden, Germany; ²Helmholtz Institute Freiberg for Resource Technology, Freiberg, Germany

Encapsulation of whole bacterial cells for water treatment using advanced technologies is the objective of this research. Bacterial cells of *Bacillus* sp. B5T were successfully encapsulated in sol-gel ceramics and show an increased uranium binding compared to biomass free ceramics.

This study focuses on the development of innovative biohybrid materials for biotechnological applications, e.g. for the removal of toxic metals from water. *Bacillus* sp. B5T was chosen which was isolated from a uranium mining waste pile in Saxony and has by far the highest uranium binding capacity of all isolates. As immobilization technique for the production of a biocomposite materials sol-gel technique was used. The bacteria were encapsulated in sol-gel ceramics forming porous networks [1]. The produced biocomposite material was evaluated according to stability and uranium removal efficiency in model and natural uranium containing solutions.

EXPERIMENTAL. *Bacillus* sp. B5T was cultivated in nutrient broth medium (12 g/L, Mast Group Ltd., Merseyside, UK) in a 50 L bioreactor under stirring and aeration. Cells were harvested at the end of exponential growth phase by centrifugation, washed and resuspended in Tris-buffer (pH 7.4) until encapsulation. The procedure of biomass encapsulation in ceramics by sol-gel technique was already described [1]. For production of bioceramics (biocer), three different silicon oxide sols were used differing in the solid matter content (smc) as follows: sol 1 15% smc, sol 2 4.3% smc and sol 3 40% smc. The biomass content of all biocers was 20% of smc. Ceramics without biomass were prepared for control experiments. The grain size of the bioceramic material after grinding and classification was 1–3 mm.

Uranium batch sorption experiments were performed with 10 mg (bio)ceramic in a volume of 15 ml aqueous uranyl solution (5 μM U(VI) in 0.9% NaClO_4 , pH 4.5) or natural uranium contaminated water from “Gessenheup” (1.5 μM U(VI), pH 4.1) under shaking (150 rpm). After different time intervals, samples for ICP-MS analysis of uranium concentration in solution were taken.

RESULTS. Three different biocers were tested for their stability with biomass contents between 10% and 25%. Over a period of 4 month, the biocers were shaken in water with 300 rpm. All biocers were stable over the investigated time period, and for uranium sorption tests an adequate amount of each biocer (Fig. 1) with 20% biomass content was produced. To investigate the influence of the matrix itself on the sorption process, also ceramics without biomass were used.

As can be seen in Fig. 2, all biocers sorb U(VI) from aqueous model solution within 24 h. However, biocer 3 possess highest binding rates for U(VI), binding 65% of U(VI) applied initially. Biocer 1 and 2 bind only 14% and 37% of the initially applied uranium(VI).

As shown in Fig. 1, the ceramic material itself binds also uranium and accounts for a maximum of 26% sorbed U(VI). Nevertheless, the influence of the biomass on the



Fig. 1: Ceramics without (a-c) and with 20% biomass (d-f). Biocer 1(a & d), biocer 2 (b & e) and biocer 3 (c & f).

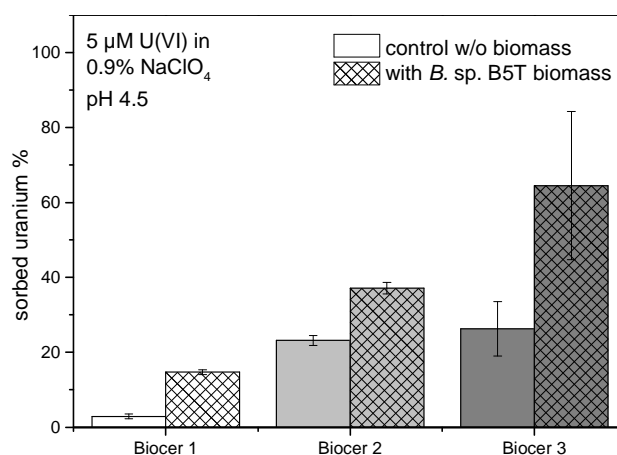


Fig. 2: Uranium sorbed from model solution (5 μM U(VI) in 0.9% NaClO_4 , pH 4.5) by different biocers within 24 h.

uranium removal from aqueous model solution was clearly demonstrated.

With natural occurring uranium contaminated water from the “Gessenheup” (Thuringa), the sorption behavior of the biocers (data not shown) is comparable to those of the uranium model solution. Again, biocer 3 shows the highest U(VI) binding capacity (21.5%). In comparison to the model solution, the overall sorption from “Gessenheup water” within 24 h was much lower because of another U-speciation.

CONCLUSION. The study on the three different biocers showed that the biohybrid material can be used for the removal of U(VI) from artificial as well as from natural occurring contaminated water. As biocer 3 has the best binding behavior in the two batch experiments, this biocer will be used for further studies on sorption capacity and regeneration potential in column reactors using geogenically contaminated waters.

ACKNOWLEDGEMENTS. The authors thank the BMBF-MOST German-Israeli Water Technology Research Fund (WT1103/02WA1223).

[1] Raff, J. et al. (2003) *Chem. Mater.* **51**, 240–244.

Metal binding capacities of calcium binding proteins Calmodulin and S-layer JG-A12

B. Drobot, F. Lehmann,¹ H. Moll, J. Raff

¹Helmholtz-Institute Freiberg for Resource Technology, Freiberg, Germany

A high affinity of Calmodulin (CaM) for lanthanides (Lns) is demonstrated. The affinity of S-layer JG-A12 is significant lower. For both protein-Eu(III)-complexes, specific binding is indicated due to different luminescence properties.

Calcium binding proteins are thought to be useful for filtering and recycling processes of rare earth elements due to their selectivity to bind trivalent lanthanides [1]. Furthermore, CaM is an important protein of the calcium signal cascade in eukaryotes. The activation of CaM by trivalent metals [2] disturbs essential cellular processes. For an assessment of chemotoxicity of trivalent metal ions (e.g. Eu^{3+} or Ce^{3+}), a fundamental understanding of the interaction is important. Hence, the metal binding capacities of recombinant expressed mammalian calmodulin (CaM) and *Lysinibacillus sphaericus* JG-A12 surface layer (S-layer) protein were tested.

EXPERIMENTAL. After purification, 10 mg/mL protein was solved in 0.1 M NaCl at pH 6. Lanthanides (CeCl_3 , EuCl_3 , and DyCl_3) were added to a final concentration of 1 mM and adjusted to pH 6. After 1 h incubation, proteins with bound metal were separated either by centrifugation (S-layer) or by ultrafiltration (CaM). The binding capacities were tested by ICP-MS and luminescence spectroscopy.

RESULTS. ICP-MS results are illustrated in Fig. 1. Because of the molecular mass of CaM (16.8 kDa) and S-layer (126 kDa), the protein concentrations differ from $\sim 600 \mu\text{M}$ (CaM) to $\sim 80 \mu\text{M}$ (S-layer). Thus, the ratio of metal per protein for the S-layer is higher while less metal is bound. Based on the assumption of 4 Ca^{2+} binding sites for CaM and 10 to 12 for S-layer, both proteins seem to be half saturated. Although heavy metals like uranium, cadmium and platinum are efficiently bound by JG-A12 [3], the affinity to tested Lns is significantly lower than for CaM. After removal of metal protein complexes, luminescence spectroscopy of the remaining solution was performed. Ln luminescence is detected in all CaM sam-

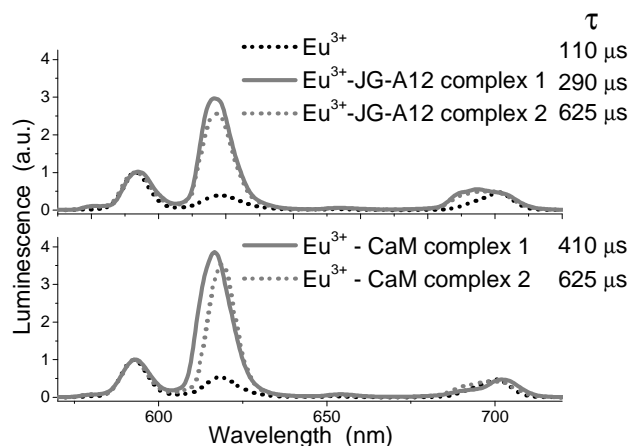


Fig. 2: Extracted single complex spectra from TRLFS measurements at pH 6. For both proteins two complexes were identified.

ples whereas for JG-A12 only a decrease is observed. These results (not shown) are in good agreement with ICP-MS.

Eu(III) TRLFS studies combined with PARAFAC deconvolution suggest the existence of two complexes for each protein (see Fig. 2). For Eu-CaM luminescence, lifetimes of 260 up to 440 μs were reported, which correspond to two coordinating water molecules in the first coordination sphere [4]. The observed long lifetime of 625 μs for CaM and S-layer suggests only one water molecule. This is in good agreement with the coordination of Ca^{2+} by the EF-hand motif where one essential water molecule is involved [5]. The shorter lifetimes provide evidence for more water molecules in the first coordination sphere. This indicates an unspecific Eu(III) binding. Based on the protein structure, amino hydroxyl and carboxyl groups are involved in coordination.

OUTLOOK. For a better understanding of the formed complexes further luminescence spectroscopic experiments are planned. Activation studies of CaM with trivalent lanthanides and actinides and additional FT-IR and NMR experiments should complete this work.

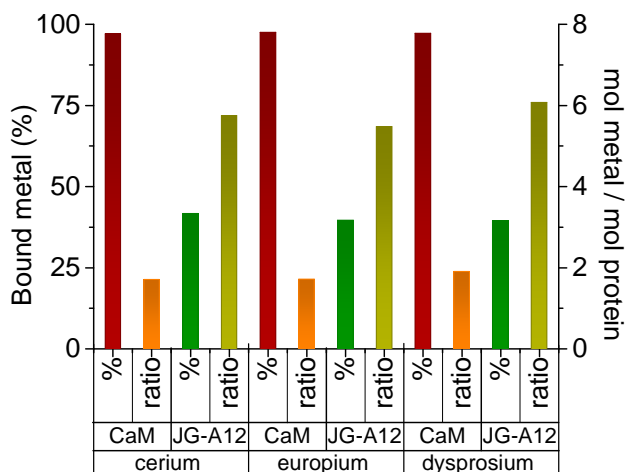


Fig. 1: Ln-binding-capacity of CaM and S-layer (10 mg/ml protein pH 6). Amount of bound metal shown as % of 1 mM Ln solution (left scale). Ratio of Ln per Protein (right scale).

[1] Buccigross, J. M. et al. (1986) *Biochem. Biophys. Res. Commun.* **138**, 1243–1249.
 [2] Thompson Amann, B. et al. (1992) *J. Biochem. Biophys. Methods* **25**, 207–217.
 [3] Pollmann, K. et al. (2006) *Biotechnol. Adv.* **24**, 58–68.
 [4] Horrocks, W.D. Jr. et al. (1988) *Biochemistry*. **27**, 413–419.
 [5] Lewit-Bentley, A. et al. (2000) *Curr. Opin. Struct. Biol.* **10**, 637–643.

Interaction of the enzyme alpha-amylase with UO_2^{2+}

A. Barkleit, C. Hennig

UO_2^{2+} forms with α -amylase in solution three complexes with carboxylate and amino coordination which was presumed from potentiometric titration and TRLFs, whereas in solid state, supposed from EXAFS, coordination with carbonyl and carboxylate groups prevails.

The protein α -amylase (α -1,4-glucan-4-glucanhydrolase; EC 3.2.1.1.) catalyzes the hydrolysis of the α -1,4 glycosidic linkages of polysaccharides like starch or glycogen. In animals and humans, it is one of the major enzymes in salivary and pancreatic secretions. In case of oral ingestion of contaminated food or radioactive substances the transport and metabolism of metal ions is strongly influenced by proteins. However, the interactions between uranyl and α -amylase have never been investigated so far.

EXPERIMENTAL. Porcine pancreatic α -amylase (Amy, 57 kDa, 50 negatively charged residues (COO^-), 48 positively charged residues (NH_3^+), 1 Ca^{2+} [1]) was purchased from Sigma. The pK_a values of α -amylase and the complex formation with UO_2^{2+} were determined potentiometrically (0.1 g L^{-1} Amy, 0.1 mM UO_2^{2+} , 0.1 M NaClO_4 , pH 3-10). The complexation was also investigated with TRLFs (0.01-0.1 g L^{-1} Amy, 0.01 mM UO_2^{2+} , 0.1 M NaClO_4 , pH 3-6). Structural aspects were studied with EXAFS (frozen solid samples, pH 3.5 and 6.0, UO_2^{2+} :Amy 1:1 and 5:1).

RESULTS. Potentiometric titration of α -amylase results in $\text{pK}_{a1}(\text{COOH}) = 5.2 \pm 0.1$ and $\text{pK}_{a2}(\text{NH}_3^+) = 10.2 \pm 0.1$. For the UO_2^{2+} - α -amylase mixture two carboxyl coordinated uranyl complexes and at higher pH one with an additional amino coordination could be identified. Stability constants of these complexes were determined to be $\log \beta_{110} = 5.8 \pm 0.1$, $\log \beta_{120} = 10.6 \pm 0.1$ (COO^- coordination) and $\log \beta_{121} = 20.0 \pm 0.1$ (additional NH_2^- coordination).

The luminescence spectra of aqueous solutions of UO_2^{2+} with α -amylase (Fig. 1) show in the pH range between 3 and 6, compared to the UO_2^{2+} aqua ion, a red shift of the emission maxima, combined with an increase of the luminescence intensity at pH 3 followed by a decrease of the luminescence intensity with rising pH. The time-resolved

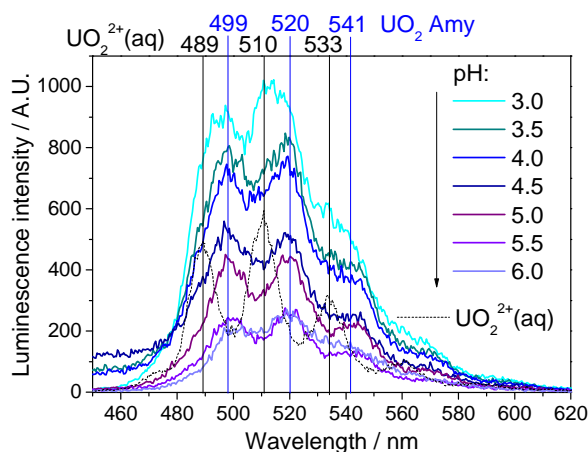


Fig. 1: Luminescence spectra of 10^{-5} M uranyl with 0.1 g α -amylase in dependence of pH.

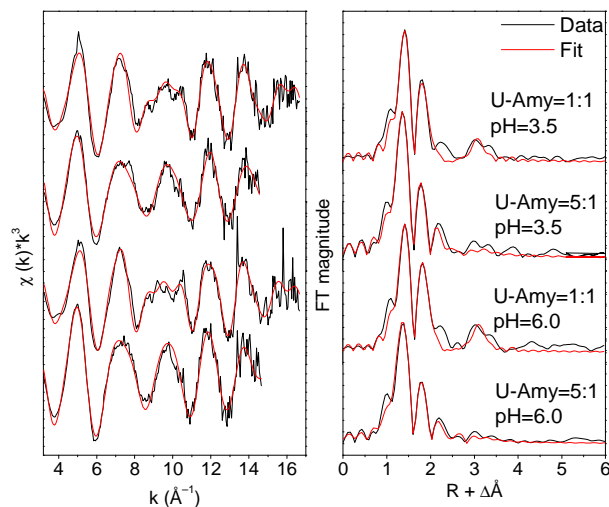


Fig. 2: Left: Raw U L_{III} -edge k^3 weighted EXAFS spectra of uranyl complexes with α -amylase including the best theoretical fits. Right: Corresponding Fourier transforms.

luminescence spectra show two different luminescence lifetimes ($t_1 = 7 \pm 1 \mu\text{s}$, $t_2 = 22 \pm 2 \mu\text{s}$) which are both longer than that of the UO_2^{2+} aqua ion ($t = 1.6 \pm 0.3 \mu\text{s}$). The TRLFs measurements indicate the formation of three dominating binding forms in the UO_2^{2+} - α -amylase system in solution. Two complexes show luminescence properties, and probably a third one which does not luminesce and therefore causes the decrease of the luminescence intensity with rising pH. These findings confirm the results obtained by potentiometry under similar experimental conditions.

The solid samples studied with EXAFS show two different coordination forms. The coordination sphere in the uranyl equatorial plane seems to be independent from the pH but only dependent from the uranyl to protein ratio (Fig. 2, Tab. 1). The short U- O_{eq} distances at equimolar ratio can be interpreted as a four-fold coordination with carbonyl groups. The split equatorial shell for the samples with higher uranyl ratio can be interpreted as a mixed coordination with monodentate carbonyl groups (shorter U- O_{eq1} distances) and bidentate carboxylate groups (longer U- O_{eq2} distances). These coordination forms differ from those obtained in solution with potentiometric titration and TRLFs, possibly due to the different concentration ratios in the solid and liquid samples.

Tab. 1: Summary of the structural parameters determined with EXAFS.

Sample	Shell	N	R / Å
UO_2^{2+} : Amy = 1 : 1, pH = 3.5	U- O_{eq}	3.1(2)	2.28(1)
	U-C	/3.1	3.47(1)
UO_2^{2+} : Amy = 5 : 1, pH = 3.5	U- O_{eq1}	2.8(8)	2.30(2)
	U- O_{eq2}	1.9(4)	2.48(2)
UO_2^{2+} : Amy = 1 : 1, pH = 6.0	U-C	/1.0	2.84(2)
	U- O_{eq}	3.4(3)	2.28(1)
UO_2^{2+} : Amy = 5 : 1, pH = 6.0	U-C	/3.4	3.48(1)
	U- O_{eq1}	3.1(6)	2.33(2)
	U- O_{eq2}	1.1(6)	2.52(2)
	U-C	/0.6	2.93(2)

All samples: shell U=O: N = 2*, R = 1.79(1) Å. / linked parameter. * fixed parameter.

[1] Artimo, P. et al. (2012) *Nucleic Acids Res.* **40**(W1), W597–W603.

Interaction of europium with the S-layer protein of *Lysinibacillus sphaericus* JG-B53 studied by ICP-MS and TRLFS

M. Suhr, K. E. Viacava Romo, R. Steudtner, J. Raff, K. Fahmy, K. Pollmann¹

¹Helmholtz Institute Freiberg for Resource Technology, Freiberg, Germany

In this study the sorption of europium with a surface layer (S-layer) protein as one component of the cell wall was investigated. The S-layer was isolated from the Gram-positive bacterial strain *Lysinibacillus sphaericus* JG-B53 recovered from the uranium mining waste pile Haberland (Johanngeorgenstadt, Saxony). For the verification of the metal sorption, inductively coupled plasma mass spectrometry (ICP-MS) was used. To determine the existence of inner sphere complexes with functional groups involved in the Eu^{3+} interaction within the biosorbent, time-resolved laser-induced fluorescence spectroscopy (TRLFS) was used. Because of the chemical similarity of lanthanides and trivalent actinides obtained results can serve also to predict the interaction with e.g. Am^{3+} or Cm^{3+} .

The importance of heavy metal removal, recovery and separation from environmental contaminated sites has been increased in the last years. The high potential of biomaterials e.g. bacteria and their single compounds to remove heavy metals promoted the search for novel biosorbents for improved remediation methods. Such metal biosorbents are S-layer proteins that are wide spread bacterial structures and which are part of the cell envelope of many bacteria and nearly all archaea [1]. In case of the S-layer of *Lysinibacillus sphaericus* JG-B53 high amounts of Pd(II), Au(III), U(VI) and Eu(III) can be bound [2,3].

EXPERIMENTAL. *Lysinibacillus sphaericus* JG-B53 was cultivated (aerobic, $T = 30^\circ\text{C}$, $\text{pH} = 7.0$) in nutrient broth media (3 g/L meat extract, 5 g/L peptone). The proteins were isolated according to an adapted method [4,5] from the harvested exponential growth phase cells. Finally, the purified and freeze dried proteins were diluted in sterile filtrated 0.9% sodium chloride solution ($\text{pH} = 6.0$) to a final concentration of 1 g/L and are used for batch sorption experiments and TRLFS studies. An initial metal concentration of 1 mM ($\text{EuCl}_3 \cdot 6\text{H}_2\text{O}$, 99%) was added for the studies. Samples for ICP-MS measurements (PerkinElmer SCIEX ELAN 6100/9000, PerkinElmer, Germany) were taken within 48 h and the metal binding rate was determined in acidic pH values to avoid adsorption effects to tube wall. The metal concentration was determined in triplets in the supernatant after centrifugation (15.000 g, 30 min, 4°C). The TRLFS spectra of Eu^{3+} were recorded using Nd:YAG laser system (Minilite laser, Continuum, USA) with an excitation wavelength at 266 nm with an averaged pulse energy of 300 μJ . The TRLFS measurements were performed after 1 h and 24 h incubation at room temperature.

RESULTS. The batch sorption experiments (Fig. 1a) demonstrated a fast and stable Eu^{3+} binding to S-layer proteins within the first minutes and a sorption maximum of 0.06 mmol/L (~ 10 mg/L) within 48 h. The data evaluations of TRLFS spectra (Fig. 1b) indicate two lifetimes, a short and a long lifetime. In table 1 the fluorescence lifetime, the fluorescence wavelength from the two energy transitions towards ${}^7\text{F}_1$ and ${}^7\text{F}_2$, the ratio between their intensities and the remaining water molecules upon com-

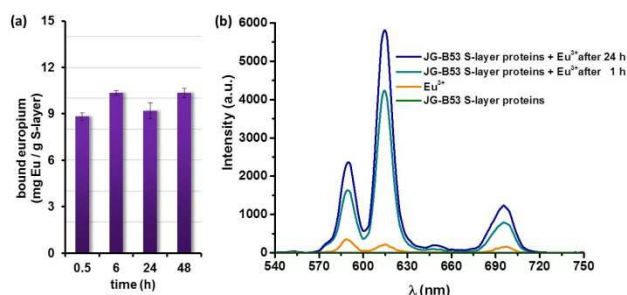


Fig. 1: (a) Bound Eu^{3+} using 1 g/L S-layer of *Lysinibacillus sphaericus* JG-B53 measured by ICP-MS; (b) Fluorescence spectra of Eu^{3+} , pure S-layer proteins, Eu^{3+} complexed by S-layer proteins from *Lysinibacillus sphaericus* JG-B53 after 1 h and 24 h.

Tab. 1: Summary of lifetime, fluorescence wavelengths (${}^7\text{F}_1$ and ${}^7\text{F}_2$), intensities ratio and remaining water molecules for the S-layer of *Lysinibacillus sphaericus* JG-B53.

Bio-Sorbent	time (h)	τ (μs)		Emission peak (nm)		Ratio (I_2/I_1)	$n_{\text{H}_2\text{O}} \pm 0.5$
		1	2	${}^7\text{F}_1$	${}^7\text{F}_2$		
JG-B53	1	159.9 ± 17	20.8 ± 8.7	589	614	2.6	6
S-Layer	24	213.2 ± 24.5	80.2 ± 11.3	589	615	1.4	4

plexation are summarized. In Fig. 1b, it is shown that the Eu^{3+} fluorescence increased after its complexation by S-layer proteins after 1 h and even more after 24 h. This indicates that the sorption equilibrium has not been reached yet.

The lifetimes shown in Tab. 1 of ~ 159.5 – 213.2 μs indicate that 3–5 water molecules are replaced upon inner sphere coordination with the S-layer protein, that is functional groups of the amino acids side chains or the peptide backbone. The longer and shorter lifetimes can be attributed to a binding to carboxyl and hydroxyl groups present in the S-layer protein respectively. The water-accessible carboxyl groups of the S-layer [6] are prime candidates for this coordination. The increase of both luminescence intensity and lifetime indicates the increasing coordination of Eu^{3+} by the biosorbent over time without increasing Eu^{3+} uptake [7].

CONCLUSIONS. ICP-MS measurements show a high binding of Eu^{3+} to the S-layer and TRLFS results indicate that this strong interaction is mainly due to carboxyl and hydroxyl groups. These findings allow an estimation of the complexation behavior of the investigated strain and an identification of the specific binding sites.

ACKNOWLEDGEMENTS. Thanks to Aline Ritter for her valuable help of the many ICP-MS measurements.

- [1] Sleytr, U.B. et al. (2001) *Progr. Surf. Sci.* **68**, 231–278.
- [2] Raff, J. et al. (2006) *Nucl. Eng. Int.*, **51**, 34–36.
- [3] Suhr, M. (2014) in preparation.
- [4] Raff, J. et al. (2003) *Chem. Mater.* **15**, 240–244.
- [5] Lederer, F.L. et al. (2013) *Microbiology* **159**, 1097–1108.
- [6] Fahmy, K. et al. (2006) *Biophys. J.* **91**, 996–1007.
- [7] Planck, G.V. et al. (2003) *Anal. Chim. Acta* **478**, 11–22.

Eu(III) binding to DNA origami

J. Oertel, L. Opherden,^{1,2} A. Barkleit, A. Keller,¹ K. Fahmy

¹Institute of Ion Beam Physics and Materials Research, HZDR, Dresden, Germany; ²TU Dresden, Germany

The folding of DNA into arbitrary two- and three-dimensional shapes, called DNA origami, represents a powerful tool for the synthesis of functional nanostructures. This work presents the first approach toward the paramagnetic functionalization of DNA origami nanostructures. By utilizing post-assembly coordination with Eu³⁺ ions, paramagnetic and luminescent DNA origami were obtained.

The DNA origami technique [1] enables the fast, high-yield synthesis of arbitrarily shaped 2D and 3D nanostructures. Since its introduction in 2006, this technique has attracted enormous interest in various research fields [2], e.g. for the controlled arrangement of proteins in studies of chemical reactions at the single molecule level. The intrinsic diamagnetic properties of DNA origami have attracted attention because they allow aligning biomolecules in solution, facilitating for instance nuclear magnetic resonance (NMR) structure determination of large macromolecules through residual dipolar couplings [3]. DNA is diamagnetic at room temperature [4] while trivalent europium is a classic Van-Vleck paramagnet [5]. Although Eu³⁺ is nonmagnetic in its ground state ⁷F₀, the first excited magnetic state ⁷F₁ becomes populated at sufficient thermal energies which results in an effective magnetic moment [5]. Therefore, Eu³⁺ coordination can be used to efficiently align Eu³⁺-coordinated DNA molecules in an external magnetic field in NMR studies [6]. In this work, we combine for the first time the synthesis of differently shaped DNA origami (triangles and six-helix bundles) with a lanthanide-mediated "paramagnetic decoration" without inducing significant structural alterations.

EXPERIMENTAL. The DNA origami nanostructures were assembled in 10 mM MgCl₂ as described previously [7]. The TRLFS measurements for Eu³⁺ were carried out with a pulsed flash lamp pumped Nd:YAG-OPO laser system from Continuum as described previously (excitation at 394 nm, time window of 1 ms) [8]. Static and time-resolved luminescence spectra of Eu³⁺ were recorded in the range of 565–650 nm (1200 lines mm⁻¹ grating, 0.2 nm resolution, 2000 accumulations) and 440–780 nm (300 lines mm⁻¹ grating, 0.7 nm resolution, 200 accumulations). A JASCO J-815 CD spectrometer equipped with a GMW 3470 electromagnet was used for CD and MCD spectroscopic measurements. Eight spectra were averaged from 185 to 320 nm (200 nm/min). MCD spectra were obtained by subtracting CD spectra recorded with a magnetic field of 2.25 T applied parallel and antiparallel to the optical path, thereby removing the non-magnetic CD signals.

RESULTS. The Eu³⁺ coordination was studied by luminescence spectroscopy (not shown). Atomic force microscopy (AFM) and circular dichroism (CD) spectroscopy revealed an intact nanostructure and DNA conformation (not shown). Using magnetic circular dichroism (MCD) (Fig. 1A), we have identified magnetically induced chirality of electronic transitions that are unique to the DNA origami and were not seen in genomic DNA. These MCD bands are specifically affected by Eu³⁺ binding in a superstructure-dependent fashion reflecting different inter-

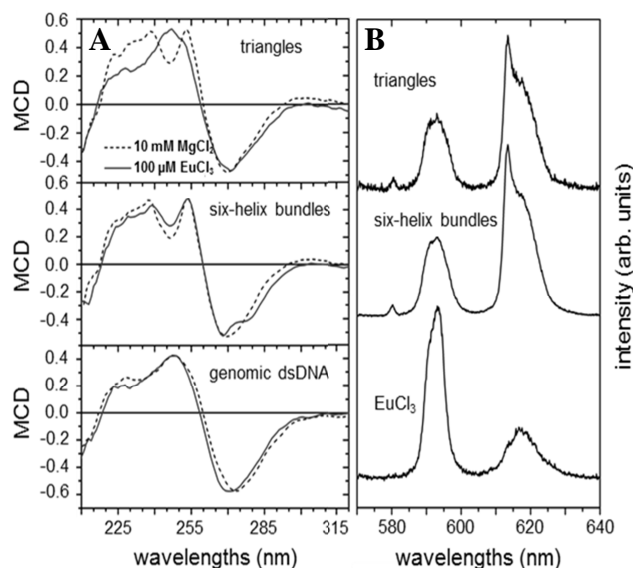


Fig. 1: (A) MCD spectra of triangular DNA origami, six-helix bundles, and genomic dsDNA in 10 mM MgCl₂ and 100 μM EuCl₃ solution. The Eu/phosphate ratio was $\delta = 0.14$ (triangles, genomic dsDNA) and $\delta = 0.07$ (six-helix bundles). (B) TRLFS spectra of 100 μM Eu³⁺ complexed with triangular DNA origami ($\delta = 0.14$) and DNA origami six-helix bundles ($\delta = 0.07$). For comparison the spectrum of pure EuCl₃ (bottom).

double strand geometries of the lanthanide-binding sites. DNA triangles lose MCD features in the 220–260 nm range, helical bundles gain structure in the 260–300 nm range when decorated with Eu³⁺. Such anisotropies are essential for magnetic alignment and agree with the partial displacement of water (up to 5–6 H₂O) from the Eu³⁺ hydration shell and with the rise of the symmetry-forbidden ⁵D₀-⁷F₀ transition at ~580 nm within the two DNA origami structures as derived from time-resolved laser fluorescence spectroscopy (TRLFS) (Fig. 1B). Comparing two differently shaped DNA origami, we showed that the lanthanide affects the magnetic properties of DNA in a superstructure-dependent fashion. The integrity of the structure was evidenced by AFM images. This simple approach opens new routes toward the magnetic manipulation of DNA origami nanostructures independently of covalent modifications. The magnetic alignment of a "lanthanide-decorated" DNA origami is superior over diamagnetically aligned DNA structures and may serve functions in nanostructure manipulation as well as in spectroscopic structural investigations.

- [1] Rothmund, P.W.K. (2006) *Nature* **440**, 297–302.
- [2] Tørring, T. *et al.* (2011) *Chem. Soc. Rev.* **40**, 5636–5646.
- [3] Bellot, G. *et al.* (2013) *Nat. Protoc.* **8**, 755–770.
- [4] Nakamae, S. *et al.* (2005) *Phys. Rev. Lett.* **94**, 248102.
- [5] Takikawa, Y. *et al.* (2010) *J. Phys. Chem. Solids* **71**, 1592–1598.
- [6] Beger, R.D. *et al.* (1998) *Magn. Reson.* **135**, 256–259.
- [7] Keller, A. *et al.* (2012) *ACS Nano* **6**, 4392–4399.
- [8] Moll, H. *et al.* (2008) *BioMetals* **21**, 219–228.

Thermodynamic quantities of the complex formation between Nd(III) and malonate as a function of ionic strength

M. Müller,¹ M. Acker,¹ S. Taut¹

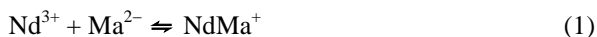
Central Radionuclide Laboratory, TU Dresden, Dresden, Germany

The complexation of Nd(III) with malonate was studied by isothermal titration calorimetry at various ionic strengths. Thermodynamic data (log K, $\Delta_R H$, $\Delta_R S$) are presented for the NaCl medium.

Thermodynamic data are required for long term safety assessment of radioactive waste disposal. Up to now, there is a great lack of data concerning the long lived actinides, especially for higher ionic strengths. Our work is focused on the organic matter present in groundwater, and we chose malonic acid as a model ligand for small organic molecules as well as for complex building structural units of humic acids. The isothermal titration calorimetry allows the measurement of heat which is released or absorbed during a chemical reaction. The heat gives direct information about the complex stability and enthalpy. The method is an alternative for the indirect determination of $\Delta_R H$ with an extended van t'Hoff equation. In this work, thermodynamic data for the complexation of Nd(III), which serves as an analogue for trivalent actinides, with malonic acid are presented for various ionic strengths.

EXPERIMENTAL. Measurements were performed with 5×10^{-3} M NdCl₃ and 0.1 m CH₂(COONa)₂ solution. The ionic strength was adjusted by adding adequate amounts of NaCl. The pH was adjusted to 5.4 using a RossTM combination pH electrode. The experimental pH values were corrected for ionic strength effects according to [1]. A MicroCal iTC₂₀₀ (GE Healthcare) was used for the calorimetric measurement. Its sample cell has a volume of 200 μ L (Nd³⁺), while the syringe volume is 40 μ L (malonate). The ligand is injected to the sample cell in precise amounts, and constant stirring provides fast mixing. Isothermal conditions (25 °C) were kept during the measurement and the change in the applied power is detected in comparison to a reference cell. Ionic strength and pH were kept constant during titration.

RESULTS. The complex formation of Nd³⁺ with malonate is endothermic and results in positive titration peaks indicating generation of heat for keeping isothermal conditions (inset graph of Fig. 1). The integrated heat curves in Fig. 1 get lower with increasing ionic strength, shifting ΔH towards zero. At the investigated concentration range, the formation of the first complex species is predominantly. However, higher complex species appear in small amounts (less than 20%) and have to be involved in data analysis. Moreover, the protonation of ligand was included in the speciation model by using ionic strength dependent data from [2]. The thermodynamic data were calculated from the curves by least square fitting using the program HypDH (Protonic software) [3]. The conditional data for the reaction



were extrapolated to zero ionic strength by linear SIT regression [4]. The results are listed in Tab. 1. Log K, $\Delta_R H$ and $\Delta_R S$ decrease with increasing ionic strength. The calculation of Gibbs free energy from standard state data results in $\Delta_R G^\circ = -17.5$ kJ/mol. The reaction is slightly en-

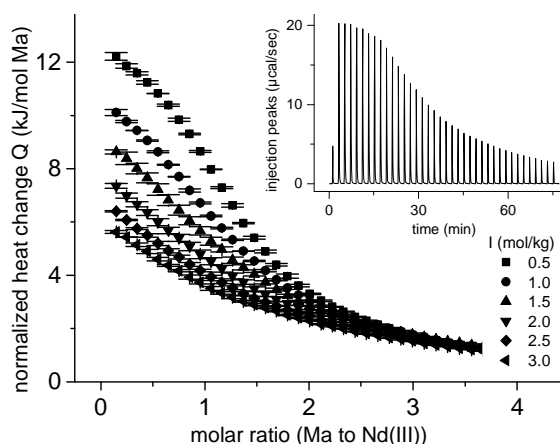


Fig. 1: Integrated titration points for Nd(III)-malonate complexation at various ionic strengths. Inset graph: Heat uptake during Nd(III) complexation with malonate at T = 25 °C and I = 0.5 m.

Tab. 1: Thermodynamic data of Nd(III)-malonate complexation at various ionic strengths. The conditional data with experimental errors were extrapolated to I = 0 by SIT plot (results given with standard error of fit).

I (mol/kg)	log K	$\Delta_R H$ (kJ/mol)	$\Delta_R S$ (J/Kmol)
0.5	3.21 ± 0.1	12.36 ± 0.01	103 ± 2
1.0	2.99 ± 0.11 (3.63 ± 0.03)*	11.23 ± 0.04 (14.0 ± 0.1)*	95 ± 2 (116.5 ± 0.7)*
1.5	2.91 ± 0.11	10.27 ± 0.05	91 ± 2
2.0	2.84 ± 0.13	9.56 ± 0.08	88 ± 3
2.5	2.73 ± 0.21	9.1 ± 0.11	83 ± 4
0 (SIT)	5.29 ± 0.06	14.74 ± 0.23	108 ± 1.5

* For the Eu(III)-malonate complex in NaClO₄ from [5].

trophy driven. The determined thermodynamic data log K, $\Delta_R H$ and $\Delta_R S$ at I = 1 m are a little bit lower in comparison to the literature values for Eu³⁺ in NaClO₄ [5]. The intercept of the SIT regression line corresponds to the sum of interaction coefficients $\Delta \epsilon$. It was determined to be -0.13 ± 0.03 . The result has the same magnitude as the $\Delta \epsilon$ for the 1:1 Cm(III)-oxalate complex, which is reported to be -0.24 ± 0.13 (Skerencak-Frech (2013) [6]). Fröhlich et al. (2013) reported a $\Delta \epsilon$ of -0.17 ± 0.01 for the analogous Cm(III)-acetate complex [7].

ACKNOWLEDGEMENTS The project is funded by BMWi (contract number: 02E11021).

- [1] Altmaier, M. (2003) *Geochim. Cosmochim. Acta* **67**, 3595–3601.
- [2] DeRobertis, A. et al. (1999) *J. Chem. Eng. Data* **44**, 262–270.
- [3] Gans, P. et al. (2008) *J. Sol. Chem.* **37**, 467–476.
- [4] Guillaumont, R. et al. (2003) *Chemical Thermodynamics 5*, Elsevier, Amsterdam.
- [5] Kitano, H. et al. (2006) *Radiochim. Acta* **94**, 541–547.
- [6] Skerencak-Frech, A. et al. (2013) *oral presentation*, INE Seminar December 2013, KIT, Universität Heidelberg.
- [7] Fröhlich, D. R. et al. (2014) *Dalton Trans.* in press, DOI:10.1039/c3dt52989d.

Thermodynamics of the protonation of oxalic and malonic acid at various ionic strengths studied by micro titration calorimetry

F. Taube,¹ M. Müller,¹ M. Acker,¹ S. Taut¹

¹Central Radionuclide Laboratory, TU Dresden, Dresden, Germany

For the first time, isothermal micro titration calorimetric (ITC) experiments were performed in order to determine thermodynamic data for the protonation of oxalic and malonic acid in NaCl medium at different ionic strengths. The standard molar protonation enthalpy ΔH_1° , the equilibrium constant $\log_{10} K_1^\circ$, and the interaction coefficient $\Delta\epsilon$ for the first protonation step of both carboxylic acids were calculated applying the Specific Ion Interaction Theory (SIT).

Natural organic matter (like humic acids) is relevant for radionuclide migration in natural environment. To predict these migration patterns, small organic model ligands such as oxalic and malonic acid are useful for both qualitative and quantitative interpretations. However, there is a lack of thermodynamic data of their protonation reactions at higher ionic strengths.

ITC is a powerful tool for the direct determination of enthalpy values and equilibrium constants for chemical reactions.

EXPERIMENTAL. The experiments were carried out with the isothermal microcalorimeter MicroCal iTC₂₀₀ (GE Healthcare) at 25 °C. Different samples of 5×10^{-3} m and 1×10^{-2} m sodium oxalate as well as 2.5×10^{-3} m sodium malonate with start pH values between 6.6 and 7.1 and various ionic strengths (adjusted by NaCl) were prepared. At regular time intervals of 180 s a small volume (1 or 2 μ L) of HCl solutions (0.05 m, 0.075 m or 0.025 m) with identical ionic strength was added to the sample and the heat effect at each titration point was detected. The integrated titration peaks were corrected for dilution heat of the titrant and were analyzed by least squares fitting (HypDH program, Protonic software) [1].

RESULTS. Figure 1 depicts the calorimetric curves of oxalate (left) and malonate (right) protonation in dependency of the ionic strength. The oxalate protonation is an endothermic reaction at low ionic strength which alters to a slightly exothermic one at higher ionic strength near 3 m. Under the chosen experimental conditions, only the first protonation step was detected.

The heat curves of malonate protonation reflect the two protonation steps. The first one is endothermic and the second one exothermic. Both steps tend to be more exothermic with increasing ionic strength.

The linearized SIT-plots (equation described in [4,5]) of the determined conditional stability constants and enthalpy values are shown in Fig. 2. The results of the linear regression are listed in Tab. 1. The values for oxalate protonation are in very good agreement with literature, for malonate the values for $\log_{10} K^\circ$ and ΔH° are slightly smaller, the value for $\Delta\epsilon$ significantly higher than literature values [5,6]. Here, more measurements are necessary to validate these values.

The results show that Micro-ITC can be successfully used for a direct determination of thermodynamic data of small organic ligand at different ionic strength.

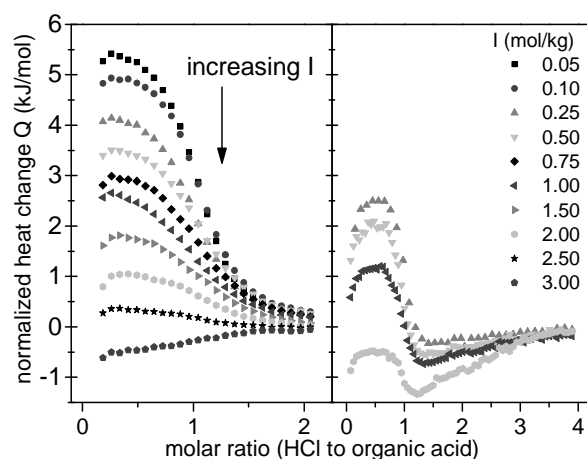


Fig. 1: Calorimetric titration curves of 5×10^{-3} m oxalate (left) and 2.5×10^{-3} m malonate (right) with HCl. Heat changes were normalized to the HCl concentration.

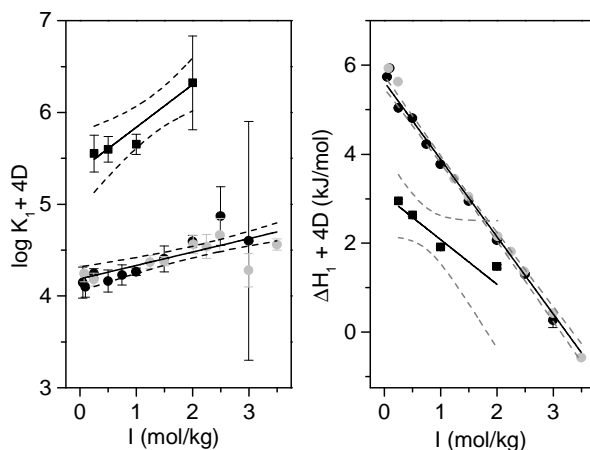


Fig. 2: SIT plots $\log K$ (left) and ΔH (right). The dots belong to 5×10^{-3} m (black) and 1×10^{-2} m (grey) oxalate. Datasets were fitted together. Squares belong to 2.5×10^{-3} m malonate. D: Debye-Hückel term D.

Tab. 1: Standard state thermodynamic parameters for the first protonation step of oxalate and malonate (errors from linear regression).

	$\log_{10} K_1^\circ$	$\Delta\epsilon$ (kg/mol)	ΔH_1° (kJ/mol)	Ref
$\text{Ox}^{2-} + \text{H}^+ \rightleftharpoons \text{HOx}^-$	4.19 ± 0.05	-0.13 ± 0.03	5.60 ± 0.07	p.w.
	4.28 ± 0.01	-0.13 ± 0.01	6.80 ± 0.5	[2]
	4.24 ± 0.01	-0.11 ± 0.01		[3]
$\text{Ma}^{2-} + \text{H}^+ \rightleftharpoons \text{HMa}^-$	5.37 ± 0.10	-0.47 ± 0.06	3.48 ± 0.22	p.w.
	5.7 ± 0.009	-0.12 ± 0.004	5.0	[5,6]

ACKNOWLEDGEMENTS. The project is funded by BMWi (contract number 02E11021).

- [1] Gans, P. et al. (2008) *J. Sol. Chem.* **37**, 467–476.
- [2] Kettler, R. M. (1991) *J. Sol. Chem.* **20**, 905–927.
- [3] Hummel, W. et al. (2005) *Radiochim. Acta* **93**, 719–725.
- [4] Guillaumont, R. et al. (2003) *Chemical Thermodynamics 5*, Elsevier, Amsterdam.
- [5] DeRobertis, A. et al. (1999) *J. Chem. Eng. Data* **44**, 262–270.
- [6] DeStefano, C. et al. (2001) *J. Chem. Eng. Data* **46**, 1417–1424.

Isotope exchange studies on the reversibility of metal-humate complexation

H. Lippold

The mobility of toxic or radioactive metals in the sub-surface hydrosphere is essentially determined by complexation with humic matter. For geochemical speciation and transport modeling, it is presumed that interaction processes are reversible, since equilibria need to respond to changing conditions. However, slow kinetic effects have been reported that lead to a growing resistance towards complex dissociation, in particular for higher-valent metals [1–3]. In this study, isotope exchange experiments were performed in order to gain direct insight into the dynamics of metal-humate complexation equilibria, also considering possible ageing effects.

EXPERIMENTAL. The conception of the isotope exchange experiments is illustrated in Fig. 1. Purified Aldrich humic acid (HA) was used as humic material. The rare earth metal terbium (M) was used as an analogue of trivalent actinides. $^{160}\text{Tb(III)}$ as a radioisotope was produced by neutron activation at the TRIGA Mark II reactor of Mainz University. By introducing it into pre-equilibrated Tb/HA systems where all available binding sites are occupied, the dynamic or static character of the complexation equilibrium can be elucidated.

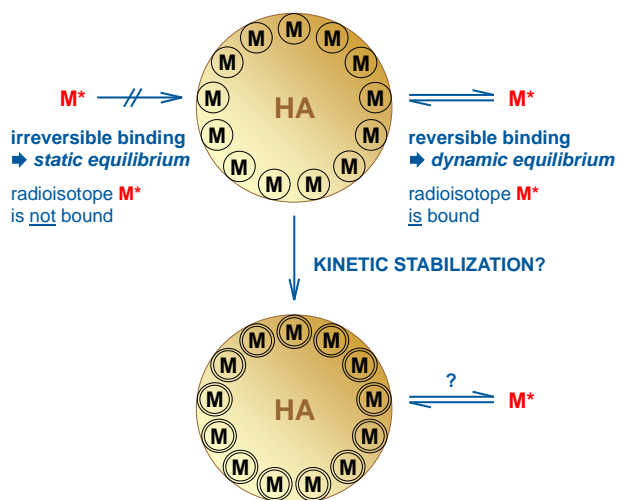


Fig. 1: Probing the equilibrium characteristics of metal-humate complexation by isotope exchange, considering possible stabilization processes (M: metal, HA: humic acid).

Humic acid (500 mg L^{-1} in 0.1 M NaClO_4 , pH 4.0) was contacted with Tb(III) at a range of concentrations up to saturation ($0.3\text{--}2.4 \text{ mM}$). The systems were completed by adding a small amount of the radiotracer $^{160}\text{Tb(III)}$ (1 nM), either instantaneously or subsequently after different time periods of pre-equilibration (1 d, 7 d, 28 d, 90 d). Equilibration times after tracer addition were kept constant at 1 d. The solutions (4 mL) were rotated end-over-end during these periods. Owing to charge compensation at the colloid surfaces, humic acid flocculates completely on loading with higher-valent metals. Thus, Tb(III) is distributed in solid/liquid systems, and adsorbed or exchanged amounts can be determined from the decrease in the concentration of the radiotracer in the supernatant after centrifugation.

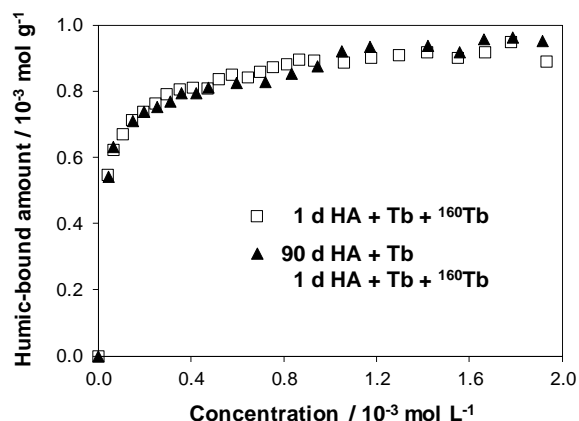


Fig. 2: Isotherms of adsorption of Tb(III) onto flocculated humic acid, obtained with ^{160}Tb as a radiotracer, which was added simultaneously together with non-radioactive Tb(III) (squares) or subsequently after a pre-equilibration period of 90 d (triangles).

RESULTS. In Fig. 2, square symbols show an adsorption isotherm obtained in conventional experiments (tracer added together with non-radioactive Tb). At equilibrium concentrations higher than 1 mM , a plateau value is reached, indicating that more binding sites are not available under the given conditions. The triangle symbols show an adsorption isotherm that was measured in a two-step procedure; ^{160}Tb was introduced after Tb/HA systems had already been pre-equilibrated for 90 d. Results obtained for shorter times of pre-equilibration were similar.

Obviously, both isotherms coincide, i.e., the tracer represents the solid/liquid distribution of total Tb, even though it is confronted with saturated surfaces. It is thus evident that there is a permanent exchange between dissolved and humic-bound Tb. An unhindered dynamic equilibrium exists, and there are no indications of limited reversibility even after extended periods of contact.

Stabilization processes in respect of complex dissociation were reported for a variety of metals, such as Al(III), Eu(III), Am(III), Th(IV) or U(VI), on time scales that are comparable to the pre-equilibration periods in this study [1–3]. Since the tracer exchange process includes a dissociation step, one may conclude that increases in complex inertness are not a general phenomenon occurring across all higher-valent metals. However, another aspect that needs further consideration is that ageing effects were observed at much lower metal concentrations in the nM range. Possibly, these effects are restricted to the strongest binding sites, which are occupied first.

ACKNOWLEDGEMENTS. This work was funded by the German Federal Ministry of Economics and Technology (BMWi), project agency PTKA-WTE, contract no. 02 E 10971. Technical support by the University of Mainz, Institute of Nuclear Chemistry, is gratefully acknowledged.

- [1] Artinger, R. et al. (1998) *J. Contam. Hydrol.* **35**, 261–275.
- [2] King, S. J. et al. (2001) *Phys. Chem. Chem. Phys.* **3**, 2080–2085.
- [3] Geckeis, H. et al. (2002) *Environ. Sci. Technol.* **36**, 2946–2952.

EXAFS study of U(VI) with Schiff Bases in methanolic solution

K. Schulz, A. Günther, A. Rossberg, G. Bernhard

The UV-vis complexation studies of uranium(VI) with different Schiff Bases reveal the formation of 1:2 complexes under the given experimental conditions. This complex structure was also confirmed by EXAFS spectroscopy.

EXPERIMENTAL. Different Schiff Bases, shown in Fig. 1, were added to an 0.001 M uranium(VI) solution. The concentration of the Schiff Base was 0.005 M for NBA, HBAP and HPIC and 0.001 M for NK50 and NK83, respectively. For all samples the ionic strength was set to 0.1 M (NaClO_4). The complexation studies were performed in methanol at 120 mV. EXAFS measurements were carried out at the ROBL beamline (BML20) at the ESRF, Grenoble. UL_3 -edge spectra of methanolic samples were collected in fluorescence mode using a 13-element-germanium detector. The spectra were analyzed with EXAFSPAK and FEFF8.2. The calculation of the theoretical EXAFS spectra was based on X-ray crystal data of uranium(VI) with 2-(2'-hydroxyphenyl)-benzoxazole [1].

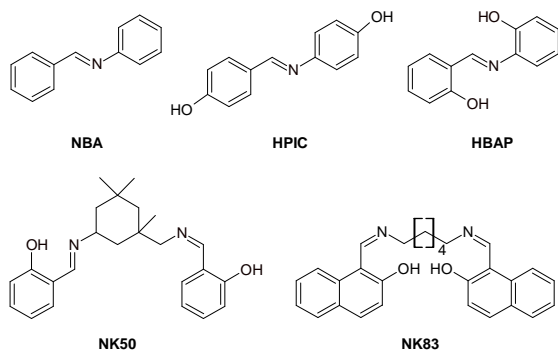


Fig. 1: Structure of the Schiff Bases N-Benzylideneaniline (NBA), 2-(2-Hydroxybenzylideneamino)-phenol (HBAP), Alpha-(4-hydroxyphenylimino)-p-cresol (HPIC) and two synthesized macrocyclic N,O-donor ligands (NK50 and NK83).

RESULTS. The k^3 -weighted UL_3 -edge EXAFS spectra (left panel) and the corresponding Fourier-transforms (FT, right panel) are shown in Fig. 2. The radial distance between uranium(VI) and the axial oxygen (O_{ax}) atoms remains almost constant in all samples at $1.78 \pm 0.01 \text{ \AA}$ with a coordination number of two. The equatorial plane is split in two nitrogen atoms and three oxygen atoms. The measured U-N distances of the uranium(VI) Schiff Bases complexes are in average $2.49 \pm 0.02 \text{ \AA}$. The averaged U-O distance is $2.28 \pm 0.02 \text{ \AA}$. The U-N distance is longer than the U-O distance.

The possible complex structures are shown in Fig. 3. The EXAFS data indicate a complex stoichiometry of 1:2 for NBA, HPIC and HBAP. The Schiff Bases NBA and HPIC probably bind monodentate via the nitrogen. The three oxygen atoms in equatorial plane are attributed to three solvent molecules. HBAP coordinates bidentately to uranium(VI) via nitrogen and oxygen. In the case of HBAP a distinction of the equatorial oxygen atoms (ligand or solvent) is not possible. Similar complex stoichiometry, as shown in Fig. 3, can also be found in the literature characterized with elementary analysis, IR and NMR [2].

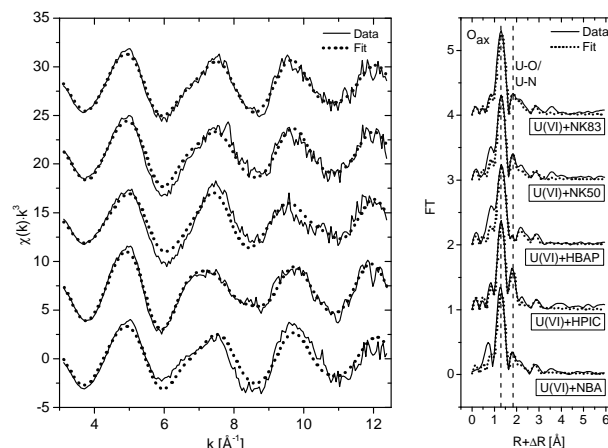


Fig. 2: UL_3 -edge k^3 -weight EXAFS spectra and the corresponding Fourier Transforms (FT) of uranium(VI) with different Schiff Bases at 120 mV.

The macrocyclic N,O-donor ligands (NK50 and NK83) favor bidentate coordination. In the literature [3], there is evidence, that such large molecules can bind two metal ions (see Fig. 3 lower molecule). Surprisingly, the proposed structure could not be confirmed by our EXAFS measurements.

The complex structures derived from the EXAFS spectra and the still have to be confirmed by DFT calculations.

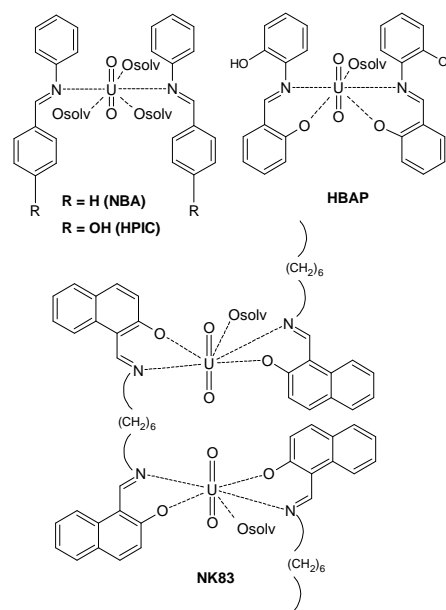


Fig. 3: Possible complex structures of uranium(VI) with basic Schiff Bases NBA, HPIC, HBAP and with macrocyclic N,O-donor ligands, for example NK83.

ACKNOWLEDGEMENTS. This work was supported by the Federal Ministry of Education and Research under contract number 02NUC014B. We would like to thank Norman Kelly (TU Dresden) for the synthesis of macrocyclic N,O-donor ligands NK50 and NK83.

- [1] Back, D. F. et al. (2010) *Inorg. Chim. Acta.* **363**, 807–812.
- [2] Biradar, N. S. et al. (1977) *Monatshfte f. Chemie.* **108**, 525–532.
- [3] El-Tabl, A. S. et al. (2003) *J. Coord. Chem.* **56**, 1113–1122.

Organo borate esters may serve as appropriate model compounds for inorganic borate complexes of trivalent actinides

J. Schott, J. Kretschmar, M. Acker,¹ A. Barkleit, S. Taut,¹ V. Brendler

¹Central Radionuclide Laboratory, TU Dresden, Dresden, Germany

The formation of a salicylato borate ester was investigated by means of ¹¹B-Nuclear Magnetic Resonance (NMR) spectroscopy. The complexation of Eu(III) by the salicylato borate ester was studied by ¹¹B-NMR spectroscopy and TRLFS (time-resolved laser-induced fluorescence spectroscopy). A complexation constant of $\log \beta_{11} \sim 2$ was determined.

So far, there is insufficient data on the complexation constant (or at least its order of magnitude) between trivalent actinides, An(III), e.g. Am(III), and borates [1]. However, in a repository borates will be provided from different sources, e.g. host rock components and glass coquilles. Consequently, the relevance of (poly)borates to mobilize An(III) under the conditions of a nuclear waste repository has to be investigated for the respective safety and risk assessment. Since the tetra-coordinated boron center ([B(4)]) in (poly)borates is negatively charged, it is assumed to represent the preferential site of metal coordination. But the determination of a stability constant for Eu(III), a chemical analog for An(III), and (poly)borates proves to be difficult due to the pH and concentration (total boron) dependent B(OH)₃-(poly)borate equilibrium. To overcome the speciation difficulties, organo borate esters, also possessing the [B(4)] unit and occurring in the acidic pH range, are used as a structural analog for inorganic (poly)borates.

EXPERIMENTAL. For ¹¹B-NMR spectroscopy solutions containing 10 mM salicylate, 200 mM boric acid, B(OH)₃, and varying Eu(III) concentration (0–100 mM) were prepared at pH 5. For TRLFS measurements samples with variable B(OH)₃ and salicylate concentration were prepared under ambient conditions at pH ~4.4 and *I* = 0.1 M before adding 3 × 10⁻⁵ M Eu(III). The samples were titrated from pH ~4.4 down to pH ~2 by adding appropriate amounts of HClO₄. After each titration step, a static Eu spectrum was recorded.

RESULTS. The formation of the salicylate borate ester can be verified by ¹¹B-NMR spectroscopy showing the signals (δ_{obs}) of boric acid and the borate ester at chemical shifts of 19.3 and 2.8 ppm, respectively (Fig. 1, spectrum a). In presence of Eu(III), the signal of the borate ester shifts downfield proving a direct interaction between Eu(III) and the salicylato borate ester (Fig. 1, spectra b–f). Considerable changes in bulk susceptibility caused by the high Eu(III) concentrations also influence the B(OH)₃ signal, but a direct interaction can be excluded. From the position of δ_{obs} of the organo borate ester the mole fraction (x_i) of free and Eu(III) bound organo borate ester can be deduced (Table 1). With these information, a complexation constant for the Eu(III) salicylato borate ester complex of $\log \beta_{11} = 1.98$ can be determined. A similar complexation constant has been determined for inorganic Eu(III) (poly)borates ($\log \beta_{11} = 2.02$). Apparently, the complexation behavior of organo borate esters and inorganic (poly)borates concerning Eu(III) is comparable. In addition, a stability constant ($\log \beta_{11} = 1.77$) for the Eu(III) salicylato borate ester complex was calculated

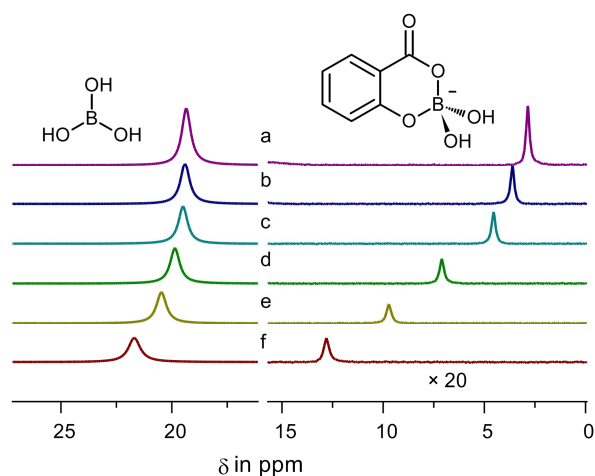


Fig. 1: ¹¹B-NMR spectra of solutions containing 200 mM boric acid, 10 mM salicylate and varying Eu(III) concentrations.

Tab. 1: Eu(III) concentration dependent chemical shift δ_{obs} and mole fractions x_i of free and bound salicylate borate ester.

Spectrum	c_{Eu} [mM]	$c_{\text{salicylate}}$ [mM]	$c_{\text{B(OH)3}}$ [mM]	$\delta_{\text{obs,corr.}}$ [ppm]	$x_{i,\text{free}}$ [%]	$x_{i,\text{bound}}$ [%]
a	0			2.8	100	0
b	2			3.6	91.2	8.8
c	5			4.4	80.6	19.4
d	20	10	200	6.6	53.0	47.0
e	50			8.6	27.8	72.2
f	100			10.5	4.3	95.7
extrapol.	"∞"			10.8	0	100

from the TRLFS titration data. The TRLFS spectra of Eu(III) salicylate in presence or absence of B(OH)₃ are clearly different (Fig. 2), indicating the removal of free salicylate due to the formation of the borate ester and a borate ester induced Eu(III) complexation different from the Eu(III) salicylate complexation.

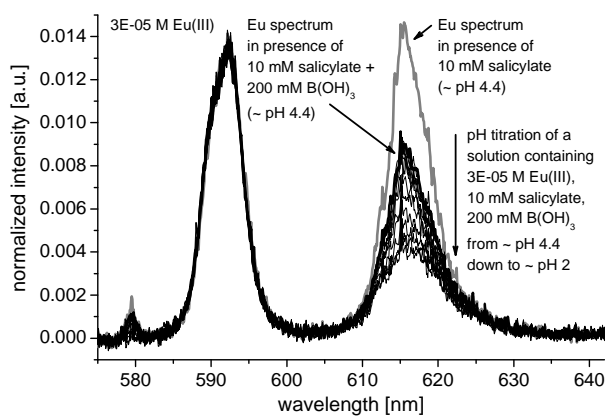


Fig. 2: Eu TRLFS pH titration spectra; comparison of Eu salicylate spectrum in absence and presence of B(OH)₃.

ACKNOWLEDGEMENTS. This work is funded by BMWi under contract number 02E11021.

[1] Borkowski, M. et al. (2010) *Radiochim. Acta* **98**, 577–582.

Data mining with artificial neural networks: aqueous U(VI) complexes with aliphatic (hydroxy-) carboxylic acids

A. Rossberg, K. Domaschke,¹ C. Lucks,² S. Tsushima

¹Life Science Inkubator Sachsen GmbH & Co. KG, Dresden, Germany; ²Federal Office for Radiation Protection – BFS, Berlin, Germany

Artificial neural networks, such as self-organizing maps (SOM) [1], are used to visualize and analyze the inherent topological structure of high dimensional data. We supplemented the SOM algorithm to include spectral mixtures described by the Beer-Lambert law.

Given a high dimensional input space, i.e. a set of spectra, SOM is able to transform this space into a lower dimensional space, while preserving – under certain conditions – the topological structure of the input space. Typically, the input space is transformed to a 2-dimensional space in which the spectra are clustered due to their spectral similarities, hence, the analysis and interpretation of high dimensional relationships in the data is simplified. This “standard” SOM, as an unsupervised learning algorithm, does not involve physical models during the training. Here, we present a way to account for spectral mixtures, described by the Beer-Lambert law, in the training period of SOM, transforming SOM into a kind of supervised learning algorithm [2].

EXPERIMENTAL. Sixty UL_{III}-edge EXAFS spectra from 13 structurally different aliphatic ((di-)hydroxy-) carboxylic acids (acetic-, succinic-, tartaric-, lactic-, 3-hydroxybutyric-, citric-, formic-, malic-, maleic-, malonic-, oxalic-, propionic-, and tricarballic acid) were measured at different pH, uranium and ligand concentrations [3]. The ligands are chosen in such a way that they would allow a structural analysis of the complexes by using the exclusion principle, i.e. by comparing the spectra in respect to the pH, concentration, presence, absence, number, position and the type of the functional group(s). Due to the high number of different constellations in this highly correlated system (different ligands may also form similar complexes), simple inspection by eye and other tools will possibly lead to different solutions and is therefore prone to misinterpretation. SOM is expected to be better adapted and more specialized for this task.

RESULTS. For SOM, the number of spectroscopic different complexes must be defined. We assumed 11 aqueous uranium complexes for which the fractions (Fig. 1a) and the spectra were calculated by a SOM consisting of 40×40 neurons (circles in Fig. 1a). Each neuron contains a spectrum, 11 fractions, the pH-value and information about the ligand structure. According to the spectral similarity, the structurally different complexes are well clustered and arranged. Note, the numbers 1–60 are assigned to the measured spectra, while numbers > 60 refer to the isolated spectra of the pure complexes. The positions of all spectra correspond to the locations for which each spectrum give the best match with the content of the neurons. Now, additional information can be exploited, like a): “Which complex is formed at which pH?”, or b): “Which part of the ligand structure is responsible to form a special complex?” For example; answer for a): As higher the pH, the higher are the fractions of the complexes 61 and 62 (compare Fig. 1b with Fig. 1a). Similar fractions of complex 69 occur at different pH (maleic acid (50, pH 5.06), malonic acid (53, pH 3.50)). The presence of

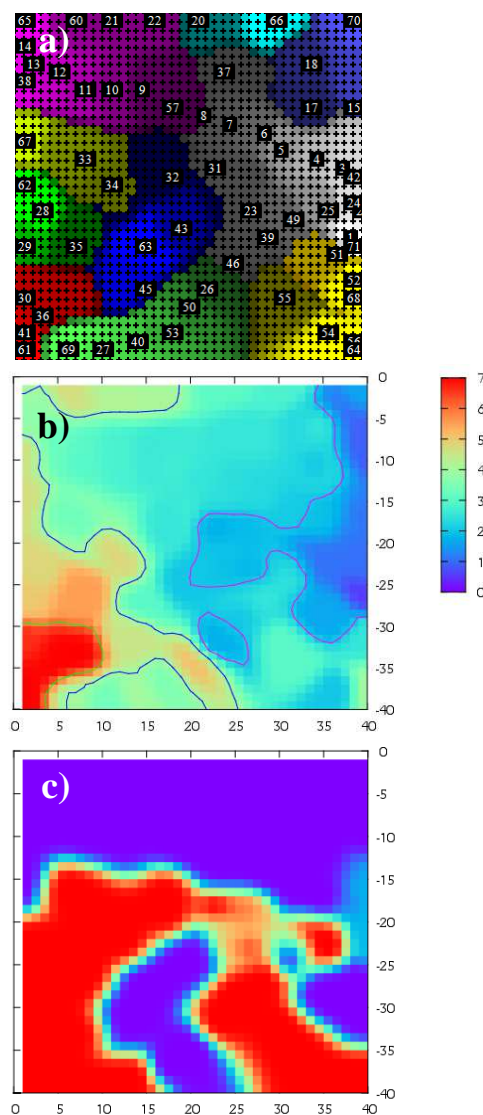


Fig. 1: 40×40 self-organizing map: Fractions of 11 different complexes (a). As brighter the colour, the higher the fraction. Note, there are only 10 colours. Distribution of the pH (b) and the ligands with OH group in α -position to the COOH group (red, c).

complex 69 at different pH could be explained by the different pK_{a2} values of these two acids. Answer for b): Complexes 61, 62 and 69 are formed if the ligands have an OH group in α -position, hence, when they can form chelates (tartaric-, lactic-, citric-, malic acid) (compare Fig. 1c with Fig. 1a).

Complex 69 can be also formed if only two COOH are present in the ligand (maleic-, malonic acid). Structural analysis shows that complex 61 and 62 are trimeric species with slightly different structure and that complex 69 is a dimeric species. The mathematics behind this special SOM is still under investigation. These preliminary results, however, nicely demonstrate the capabilities of SOM.

[1] Kohonen, T. (1990) *Proc. IEEE* **78**, 1464–1480.

[2] Domaschke, K. et al. (2014) *Proc. ESANN*, submitted.

[3] Lucks, C. (2013) Ph.D. Thesis, TU Dresden, Germany.

SCIENTIFIC CONTRIBUTIONS (PART II)

**LONG-LIVED RADIONUCLIDES IN
FINAL DISPOSAL SYSTEMS**

Uranyl(VI) speciation in strong alkaline solution

S. Tsushima, A. Rossberg, H. Moll, R. Steudtner, B. Drobot, K. Müller, K. Fahmy

The speciation of U(VI) in highly alkaline solution was studied by DFT calculations as well as by X-ray absorption (XANES) spectroscopy [1].

CALCULATIONS. Density functional theory (DFT) calculations were performed using Gaussian 09 program at the B3LYP level in the aqueous phase using CPCM model. Small core effective core potential and the corresponding basis set was used for U. Valence triple zeta plus polarization basis was used for O and H.

EXPERIMENTAL. The test solutions S1 and S5 were prepared from appropriate amounts of UO_3 and tetramethylammonium hydroxide (TMA-OH, Sigma-Aldrich) under inert gas atmosphere to get a final total concentration of 50 mM UO_2^{2+} , and 1.0 M or 3.0 M TMA-OH for S1 and S5, respectively. For sample S1, the solid was dissolved in water, whereas for sample S5 the solid was dissolved in methanol. The test solutions were kept in dark under N_2 atmosphere.

RESULTS. First we studied by DFT calculations whether the hydrolysis of $\text{UO}_2(\text{OH})_4^{2-}$ yields $\text{UO}_2(\text{OH})_5^{3-}$ or $\text{UO}_3(\text{OH})_3^{3-}$. As shown in Fig. 1, the Gibbs energy as well as the activation energy is lower to form $\text{UO}_3(\text{OH})_3^{3-}$ than $\text{UO}_2(\text{OH})_5^{3-}$ suggesting the formation of $\text{UO}_3(\text{OH})_3^{3-}$.

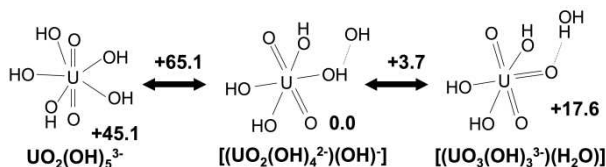


Fig. 1: Equilibrium among $[(\text{UO}_2(\text{OH})_4^{2-})(\text{OH})^-]$, $\text{UO}_2(\text{OH})_5^{3-}$, and $[(\text{UO}_3(\text{OH})_3^{3-})(\text{H}_2\text{O})]$. Relative Gibbs energy and activation Gibbs energy at the B3LYP level are given in kJ mol^{-1} .

We studied experimentally samples S1 and S5 using XANES. It is clear from the previous study [2] that $\text{UO}_2(\text{OH})_4^{2-}$ predominates in S1. In S5, we expected the presence of the further hydrolyzed species $\text{UO}_2(\text{OH})_5^{3-}$ or $\text{UO}_3(\text{OH})_3^{3-}$. However, it is also likely that deprotonated methanol (MeO^-), instead of OH^- , could be partly coordinated to uranium. The resulting stoichiometry of the species can be described as $\text{UO}_2(\text{MeO})_m(\text{OH})_n^{2-}$ ($m+n=4$, $m>0$) and $\text{UO}_3(\text{MeO})_k(\text{OH})_l^{3-}$ ($k+l=3$, $k>0$).

We measured uranium L_{III} edge XANES spectra of these samples, the results are shown in Fig. 2. As mentioned already, $\text{UO}_2(\text{OH})_4^{2-}$ comprises nearly 100% of S1. In S5, there is a mixture of the species $\text{UO}_2(\text{MeO})_m(\text{OH})_n^{2-}$ and $\text{UO}_3(\text{MeO})_k(\text{OH})_l^{3-}$. In the previous NMR study by Moll et al. [2], the authors used the same solution as S5 but measured the spectra at 258 K. Moll et al. concluded that the sample is a 3:1 mixture of $\text{UO}_2(\text{OH})_4^{2-}$ and $\text{UO}_2(\text{OH})_5^{3-}$ although we suspect that it is a mixture of $\text{UO}_2(\text{MeO})_m(\text{OH})_n^{2-}$ and $\text{UO}_3(\text{MeO})_k(\text{OH})_l^{3-}$. In the present investigation, XANES measurements of S5 was performed at lower temperature (200 K) compared to Moll et al. (258 K). The fraction of the further hydrolyzed species $\text{UO}_3(\text{MeO})_k(\text{OH})_l^{3-}$ must be therefore greater than 25% found by Moll et al., because methanol has a significantly higher dielectric constant at lower temperature. Correspondingly, the presence of the higher charged species is

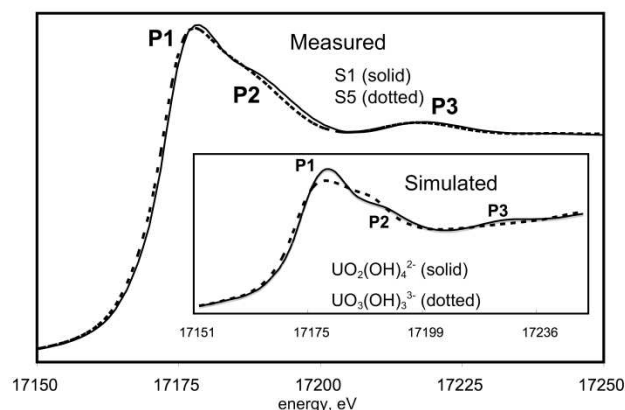


Fig. 2: Uranium L_{III} -edge XANES spectra of 50 mM U(VI) in 1.0 M TMA-OH aqueous solution at room temperature (S1) and in 3.0 M TMA-OH methanol/water mixture at 200 K (S5). The inset shows the simulated spectra of $\text{UO}_2(\text{OH})_4^{2-}$ and $\text{UO}_3(\text{OH})_3^{3-}$.

expected to be more pronounced under conditions of a higher dielectric constant.

From Fig. 2, it can be seen that the U L_{III} absorption edge (P1) of S5 is slightly shifted to lower energy (~ 0.5 eV) compared to that of S1. Such a shift can be interpreted as U(VI) reduction to U(V) or U(IV). However, the samples were kept in dark under N_2 atmosphere immediately after the preparation to avoid photochemical reduction. Also, when S5 was measured at room temperature, the energy shift was not observed. Therefore, the shift of P1 indicates a speciation change of U(VI), rather than a change in the oxidation state. In a previous study on Pa(V) by Le Naour et al. [3], the authors found a similar energy shift of the Pa L_{III} absorption edge in going from Pa^{5+} ion to PaO_3^+ ion. As demonstrated in the Pa case, formation of an additional oxo bond to the actinide center provokes a shift of the absorption edge, hence the shift of the absorption edge in going from S1 to S5 is in accordance with our hypothesis that there is an additional oxo bond formation in the species in S5, namely formation of $\text{UO}_3(\text{MeO})_k(\text{OH})_l^{3-}$. To confirm this hypothesis, we simulated the XANES spectra (U L_{III} -edge) of $\text{UO}_2(\text{OH})_4^{2-}$ and $\text{UO}_3(\text{OH})_3^{3-}$ using the FEFF9 program as shown in the inset of Fig. 2. The structures of $\text{UO}_2(\text{OH})_4^{2-}$ and $\text{UO}_3(\text{OH})_3^{3-}$ were taken from the DFT results. The simulations result in a slight shift (~ 1 eV) of the absorption edge (P1) of $\text{UO}_3(\text{OH})_3^{3-}$ as compared to $\text{UO}_2(\text{OH})_4^{2-}$. Also, the shoulder P2 in $\text{UO}_2(\text{OH})_4^{2-}$ is shifted to lower absorption energy in $\text{UO}_3(\text{OH})_3^{3-}$, and the shoulder P3 in $\text{UO}_2(\text{OH})_4^{2-}$ is not apparent in $\text{UO}_3(\text{OH})_3^{3-}$. The overall features of the simulated XANES spectra of $\text{UO}_2(\text{OH})_4^{2-}$ and $\text{UO}_3(\text{OH})_3^{3-}$ match with the measured spectra of S1 and S5, respectively.

ACKNOWLEDGEMENTS. We acknowledge generous access to the computing resources at The Center for Information Services and High Performance Computing, Dresden University of Technology, Dresden, Germany.

- [1] Moll, H. et al. (2014) *Inorg. Chem.*, in press.
 [2] Moll, H. et al. (2000) *Radiochim. Acta* **88**, 411–415.
 [3] Le Naour, C. et al. (2005) *Inorg. Chem.* **44**, 9542–9546.

Specific surface speciation of uranium(VI) on iron (hydr)oxides

H. Foerstendorf, N. Jordan, K. Heim

The surface speciation of uranium(VI) on ferrihydrite (Fh) and maghemite (γ -Fe₂O₃; Mh) was comparatively investigated by vibrational spectroscopy. While stable inner-sphere complexes are predominantly formed on Fh, a high reversibility of the sorption complexes on Mh was observed suggesting the preferential formation of U(VI) outer-sphere complexes.

The detailed knowledge of the surface speciation of actinide ions is indispensable for the verification of the equations of chemical reactions and thus for a reliable description of their migration behavior in the near and far field of a future waste disposal site. Such molecular information of the sorption processes is provided by in situ ATR FT-IR spectroscopy.

EXPERIMENTAL. The detailed description of the preparation of the mineral films as stationary phase in the spectroscopic experimental setup and the acquisition of the spectral data is described elsewhere [1,2].

RESULTS. From the sorption spectra recorded under inert gas conditions (Fig. 1A) and as well in ambient atmosphere (Fig. 1B), the band of the $\nu_3(\text{UO}_2)$ mode is observed at lower frequencies (903 cm⁻¹) for the Fh phase in comparison to Mh (912 cm⁻¹). A comparison of the frequencies of the $\nu_3(\text{UO}_2)$ mode from uranyl surface species on different mineral surfaces might not be appropriate because intrinsic surface properties may dominate the stretching vibration of the sorbed ion. However, with respect to the evidenced formation of inner-sphere complexes at the Fh surface [3], the higher frequency of the uranyl band in the Mh spectrum indicates the formation of a different kind of surface species.

This suggestion is approved by the spectra of the desorption processes (Fig. 1C). In contrast to the spectrum of the Mh phase, where extensive U(VI) desorption is observed, the spectrum of the Fh phase reflects nearly no release of uranyl ions during the desorption process corroborating the tight binding of the uranyl ions to the Fh phase. Furthermore, the desorption spectrum of Mh clearly demonstrate the release of the same species already prevailing during the sorption process (Fig. 1B). This can be derived from the band positions and intensities which are nearly identical in the spectra of the sorption and desorption processes on Mh [2].

From the spectra obtained under ambient conditions, a similar carbonate surface speciation can be suggested for both iron bearing phases due to the concurrent band positions above 1200 cm⁻¹, even though the relative intensities of the carbonate bands are significantly lower in the sorption spectrum of Mh (Fig. 1B). Nevertheless, the homology of the frequencies of the $\nu_3(\text{CO}_3)$ modes observed for both mineral phases suggests a similar carbonate speciation in both sorption systems: the presence of ternary U(VI)carbonato surface species where the carbonate ions are bidentately coordinated to the uranyl units and the presence of a monodentate carbonate species coordinated to the respective mineral phase. The low intensities of these bands in the Mh spectra might be due either to a less extensive formation of ternary surface complexes or to the outer-spheric character of the U(VI) surface complex. It is

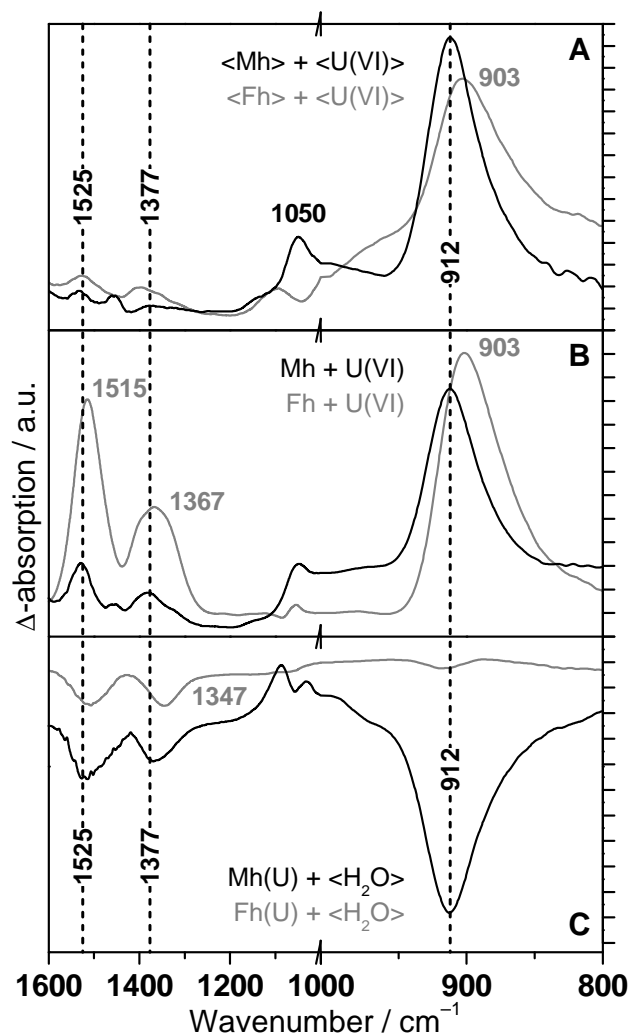


Fig. 1: IR spectra of the U(VI) sorption processes under inert gas conditions (A) and in ambient atmosphere (B) onto Mh (black lines) and ferrihydrite (Fh, grey lines) and subsequent desorption processes (C). Solid phases or solutions equilibrated under inert gas conditions are given in angle brackets. Positive and negative bands represent the surface species after and before induced sorption (A and B) or induced desorption (C), respectively. Ordinate scaling is 2.5 mOD/tick. Indicated frequencies are in cm⁻¹.

also conceivable that the band intensities of such carbonate ligands correlate with the distance from the surface and, thus, appear with reduced intensities in a ternary outer-sphere complex. An unequivocal explanation cannot be given presently.

Contrary to former observations on Fh and hematite, which evidenced the significant formation of uranyl carbonato surface complexes, such complexes are occurring with a considerable less specificity on Mh. Hence, for the assessment of retardation of uranium under oxidizing conditions in aquifers, maghemite is expected to be of minor relevance compared to other iron oxides or hydroxide phases.

[1] Foerstendorf, H. et al. (2012) *J. Colloid Interface Sci.* **377**, 299–306.

[2] Foerstendorf, H. et al. (2014) *J. Colloid Interface Sci.* **416**, 133–138.

[3] Rossberg, A. et al. (2009) *Environ. Sci. Technol.* **43**, 1400–1406.

Uranium sorption on montmorillonite in four electrolyte systems of high ionic strength

K. Fritsch, K. Schmeide

Sorption studies of U(VI) on montmorillonite in NaCl, CaCl₂, KCl and MgCl₂, which are present in pore waters of North German clay deposits, have been performed. While the NaCl and KCl systems show the classic ionic strength effect, sorption in CaCl₂ and MgCl₂ is at least partly determined by secondary phase formation.

North German clay deposits are considered for deep-level nuclear waste repositories. In the relevant depths, the ionic strength of the pore waters of these clay deposits ranges from below 2 M up to 3.5 M increasing with depth [1]. Therefore, it is necessary to determine the sorption of radionuclides on clays in high ionic strength electrolytes.

EXPERIMENTAL. Montmorillonite was used as substrate after purification according to literature [2,3]. The sorption and leaching experiments were conducted under the following conditions: S/L = 4.00 ± 0.01 g L⁻¹, background electrolyte NaCl, CaCl₂, KCl or MgCl₂, c = 0.1...3 M, pH = 4...10, room temperature, presence and absence of CO₂, c_{U(VI)} = 1 × 10⁻⁶ M (initial U(VI) concentration for isotherms: 1 × 10⁻⁸ ... 1 × 10⁻⁵ M), sorption time 5 to 6 days; additional experimental conditions for the desorption experiments: 5 desorption steps (7 days each).

RESULTS. U(VI) sorption in NaCl and KCl looks very similar due to the similar nature of the ions. There is an ionic strength effect below pH 6 for ionic strengths below 2 M. For higher pH values and higher ionic strengths, no ionic strength effect is observable. The sorption maximum at high ionic strength lies at slightly below pH 7. The sorption isotherm at pH 5.31 – where the ionic strength effect and therefore outer-sphere complexation is predominant – shows non-linear sorption behavior for an ionic strength of 2 M NaCl, where the exponent n_F is smaller than 1 (see Fig. 1). Setting n_F = 1 leads to lg k_F being equal to lg K_d, which in this case is 3.72 ± 0.06. This value is consistent with the results from the corresponding batch experiments (data not shown). Sorption in the CaCl₂ and MgCl₂ systems is at least partly governed by secondary phase formation. Depending on pH and other factors (like U(VI) concentration and absence or presence of CO₂), uranium compounds precipi-

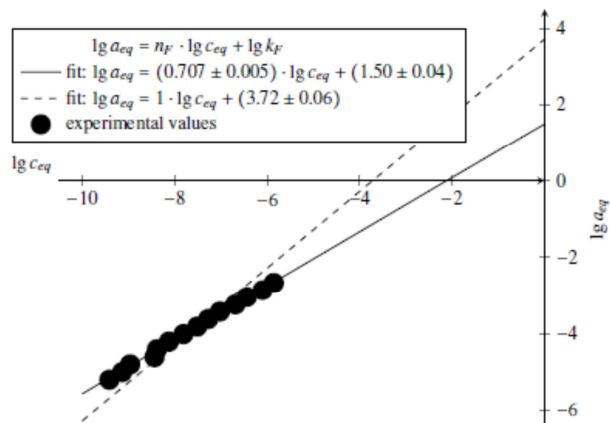


Fig. 1: U(VI) sorption isotherm (Freundlich isotherm) on montmorillonite in 2 M NaCl at pH 5.31 in absence of CO₂.

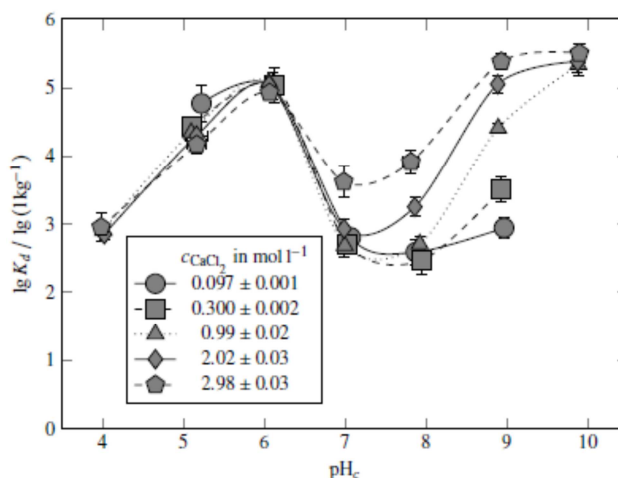


Fig. 2: U(VI) sorption on montmorillonite in CaCl₂ in dependence on ionic strength and pH (p_{CO₂} = 10^{-3.5} atm).

tate. In presence of CO₂, carbonates form and depending on the pH, precipitation of hydroxide occurs. There is also evidence for the formation of insoluble silicate compounds. This helps to explain the correlation between ionic strength and U(VI) sorption in the alkaline pH range that is observed in the CaCl₂ system and the high apparent sorption that is exhibited by the MgCl₂ system (in the latter, precipitates are so preeminent that they are visible to the naked eye). In the acidic pH range, these two systems showed no effect of the ionic strength above an electrolyte concentration of 0.1 M.

Desorption experiments in NaCl and CaCl₂ at pH 5–7 [4] gave further insight in the sorption processes at work. In NaCl, the sorption was shown to be completely reversible over all 5 steps for c = 0.1 and 0.6 M, whereas at 3 M the K_d increased with each desorption step. In CaCl₂, sorption reversibility was dependent on pH rather than ionic strength, though in this case only concentrations of 0.1 and 0.3 M CaCl₂ were used. At pH 5, sorption is fully reversible, while at pH 6 and 7, the K_d of the sorption step was consistently lower than the K_d of the following desorption steps, which means that some irreversible U(VI) deposition happened between those two steps. Currently, determination of the surface complexes involved is under way.

ACKNOWLEDGEMENTS. This work was funded by the BMWi (No. 02 E 10971).

- [1] Brewitz, W. et al. (1982) *Eignungsprüfung der Schachtanlage Konrad für die Endlagerung radioaktiver Abfälle*. GSF-T 136.
- [2] Poinssot, C. et al. (1999) *Nagra Technical Report 99-04*.
- [3] Bradbury, M., Baeyens, B. (2009) *Geochim. Cosmochim. Acta*, **73**, 990–1003.
- [4] Zehlke, L. (2013) *Durchführung von Sorptions- und Desorptionsversuchen von Uran(VI) an Montmorillonit*, Bachelor thesis, TU Dresden.

In situ vibrational spectroscopic identification of Np(V) sorption reactions on ferrihydrite

K. Müller, J. Berger

The Np(V) sorption onto ferrihydrite has been studied in situ by application of ATR FT-IR spectroscopy. The formation of a single inner-sphere complex has been derived.

Amorphous iron oxides play a decisive role in regulating the mobility of contaminants in rock and soil formations particularly because of their tendency to form coatings on mineral surfaces [1]. In this work, Np(V) sorption on amorphous ferrihydrite (Fh) is investigated in the presence and absence of carbonate.

EXPERIMENTAL. Suspensions of Fh were prepared in an N₂ atmosphere and subsequently characterized as described previously [2]. The BET specific surface area was found to be 162 m²/g. The isoelectric point determined by zeta potential is at pH 9.4. For sorption experiments, Np(V) concentration was set to 50 μM at an ionic strength of 0.1 M adjusted by NaCl at pH 8. All measurements were performed with D₂O (Sigma Aldrich, isotope purity > 99%) The ATR FT-IR accessory and the procedure for the in situ sorption measurement were described in detail previously [3].

RESULTS. The IR spectra obtained in the absence of carbonate are shown in Fig. 1. The bands observed in the spectrum of the conditioning stage preferentially represent bands of the mineral phase which potentially might contribute to the spectra recorded during the subsequent sorption and flushing processes.

Upon Np(V) sorption several bands increase with time. The band at 785 cm⁻¹ is assigned to the antisymmetric stretching vibrational mode (ν₃) of the sorbed neptunyl ion. The IR spectrum obtained from an aqueous solution at 50 μM Np(V), 0.1 M, pH 6 shows the absorption of ν₃(Np^VO₂) at 818 cm⁻¹. The red shift of ν₃ to 785 cm⁻¹ can be assigned to an inner-sphere monomeric sorption complex, as previously reported for hematite and other mineral oxides [3]. The band at 1025 cm⁻¹ is due to rearrangement processes at the mineral oxide surface upon sorption and are similarly observed for interactions on hematite [3]. In the flushing stage, a weakly bound species is re-

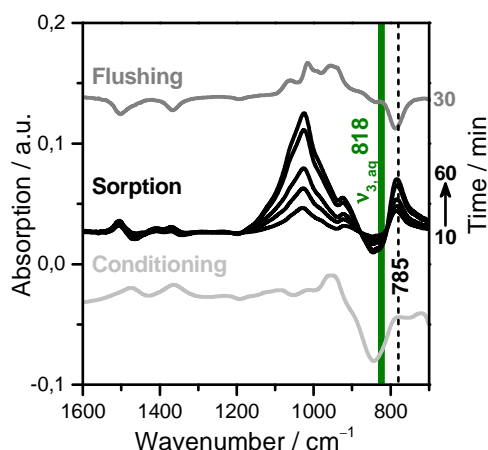


Fig. 1: ATR FT-IR spectra of 50 μM Np(V) sorbed onto Fh at pH 8, 0.1 M NaCl, D₂O, N₂. Spectra are equally scaled. Indicated values are in cm⁻¹.

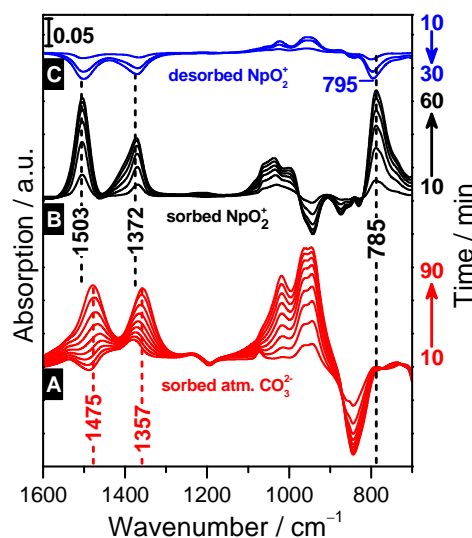


Fig. 2: ATR FT-IR spectra of 50 μM Np(V) sorbed onto Fh at pH 8 with atmospherically added carbonate, 0.1 M NaCl, D₂O, N₂. Spectra are equally scaled. Indicated values are in cm⁻¹.

leased from the stationary phase, reflected by a negative band at 790 cm⁻¹ in the respective spectra.

The IR spectra obtained in the presence of atmospheric equivalent added carbonate are shown in Fig. 2. During the conditioning stage, bands are observed at 1475 and 1357 cm⁻¹ representing the doubly degenerated C-O stretching mode (ν₃) of the CO₃²⁻ ions split into the anti-symmetric and symmetric modes upon coordination to the mineral's surface. According to their frequencies, they can be interpreted in terms of a monodentate binding of the carbonate ions to the Fh phase [2]. During the Np(V) sorption stage, these bands are shifted to 1503 and 1372 cm⁻¹ indicating the formation of a ternary Np(V) carbonate complex with bidentately coordinated carbonate ions [2]. The ν₃(NpO₂) modes of the sorption species at 785 cm⁻¹ are not further shifted in comparison to those obtained in N₂ atmosphere. This was already found for Np(V) carbonate complexation on gibbsite [4]. During the flushing a Np(V) carbonate complex, possibly NpO₂CO₃⁻, is released with ν₃(NpO₂) observed at 795 cm⁻¹ [4].

In summary, the IR spectra evidence the formation of a single Np surface species, most probably a mononuclear bidentate complex, formed irrespectively of the presence of atmospherically derived CO₂. The character of the carbonate surface species correlates with the presence of the actinyl ions and changes from a monodentate to a bidentate binding upon Np(V) sorption.

ACKNOWLEDGEMENTS. The authors are grateful to C. Eckardt, S. Weiß. The funding of this work by Deutsche Forschungsgemeinschaft (MU 3207/1-1) is greatly acknowledged.

- [1] Dixon, J. B. et al. (1989) *Minerals in soil environments*, Soil Science Soc. of America, Madison, Wis.
- [2] Foerstendorf, H. et al. (2012) *J. Colloid Interface Sci.* **377**, 299–306.
- [3] Müller, K. et al. (2009) *Environ. Sci. Technol.* **43**, 7665–7670.
- [4] Gückel, K. et al. (2013) *Environ. Sci. Technol.* **47**, 14418–14425.

Np(V) retention by siderite

R. Steudtner, A. Maffert, A. C. Scheinost

Fe(II)-bearing secondary mineral phases, forming e. g. as corrosion products on steel containers, may greatly improve the retention of redox-sensitive radionuclides in nuclear waste repositories. Here, we show the mechanisms of Np(V) uptake by siderite ($\text{Fe}^{\text{II}}\text{CO}_3$), a phase relevant in CO_2 -rich systems. The high retention capacity across the stability field of siderite is explained by reduction of Np(V) to Np(IV) and subsequent precipitation as NpO_2 nanoparticles.

EXPERIMENTAL. The mineral siderite was synthesized as described in [1]. Sorption experiments were conducted with an initial Np(V) concentration of $2 \times 10^{-5} \text{ mol L}^{-1}$ in solutions with an ionic strength of 0.1 M. The retention of Np was studied in batch experiments as function of the pH, the solid-to-liquid ratio, the sorption time and with two background electrolytes (NaCl or Na_2CO_3). Mineral synthesis and sorption experiments were performed under strictly anoxic conditions in a glovebox at $< 2 \text{ ppm O}_2$. For calculation of the retention coefficient (R_d in mL g^{-1}), the remaining Np concentration in the supernatant was determined by liquid scintillation counting. We investigated the oxidation state of the Np species retained by siderite with XANES (X-ray absorption near-edge structure) spectroscopy, and their local structure with EXAFS (Extended X-ray absorption fine-structure).

RESULTS. The siderite formed is extremely oxidation-sensitive and unstable below pH 7. Its identity was confirmed by Raman spectroscopy, based on two hot bands around 300 and 1085 cm^{-1} . These signals are in very good agreement with the Raman database (RRUFF Project [2]). Formation of the Fe(II) hydroxo carbonato phase chukanovite ($\text{Fe}^{\text{II}}_2(\text{CO}_3)(\text{OH})_2$) could be excluded.

The Np(V) retention in the stability window of siderite is slightly reduced by CO_3 -species, but shows little variation with pH (Fig. 1). It is therefore evident that both surface charge (note PZC at 10.3) and changes of aqueous Np(V) speciation with pH have little influence on the Np uptake behavior.

The XANES spectra of the sorption samples show an edge energy of 17605.7 to 17606.2 eV, as determined by the knot of the second derivatives, in line with Np(IV).

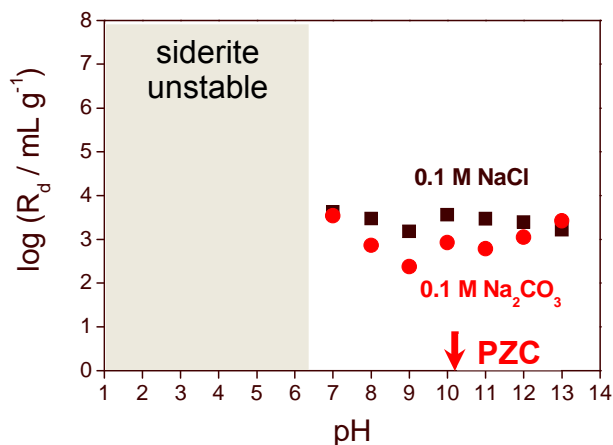


Fig. 1: pH sorption edges of Np(V) onto siderite. $s/l = 1 \text{ g L}^{-1}$, $I = 0.1 \text{ M}$, $[\text{Np(V)}]_{\text{initial}} = 2 \times 10^{-5} \text{ M}$, after 1 w, in N_2 atmosphere.

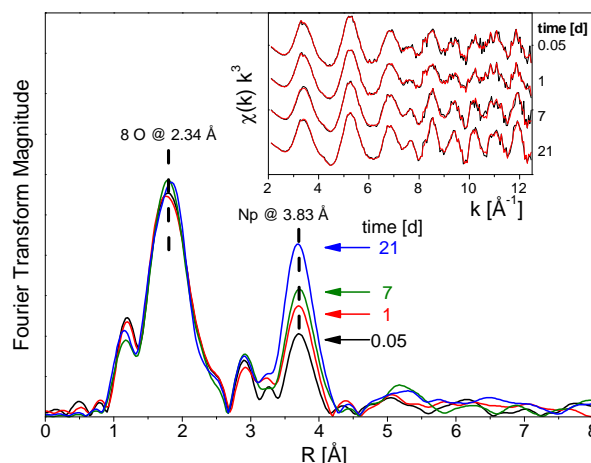


Fig. 2: Fourier transform magnitude spectra of siderite-reacted Np as function of the sorption time at pH 8, $s/l = 1 \text{ g L}^{-1}$, $I = 0.1 \text{ M}$, $[\text{Np(V)}]_{\text{initial}} = 2 \times 10^{-5} \text{ M}$, N_2 .

The complete reduction of Np(V) to Np(IV) at the siderite surface is further confirmed by the EXAFS-derived single shell coordination of about 8 oxygen atoms at a distance of 2.34 to 2.37 Å (Fig. 2). There is also a Np-Np shell visible, with a distance of 3.82 to 3.84 Å. This distance is in line with that of NpO_2 [3,4]. Coordination numbers, however, are much smaller (2.3 to 4.3) than the expected 12 neighbors of the cubic space group which indicates formation of nanoparticles. These nanoparticles grow with increasing equilibration time from 2 hours to 3 weeks (Fig. 2), in line with Ostwald ripening.

The reduction of Np(V) to Np(IV) and the subsequent precipitation as NpO_2 -like nanoclusters explains the small influence of pH and aqueous speciation as observed macroscopically in the batch experiments. In summary, siderite has high retention capacities for aqueous Np(V). Even at high pH and in presence of carbonate – conditions relevant for nuclear waste repositories – the $\log R_d$ value are ≥ 3.5 .

ACKNOWLEDGEMENTS. This work is part of the IMMORAD project, funded by BMWi through contract 02NUK019D.

- [1] Jönsson, J. et al. (2008) *Chem. Geol.* **255**, 173–181.
- [2] Downs, R. T. (2006) *Program and Abstracts of the 19th General Meeting of the International Mineralogical Association.*
- [3] Allen, P. G. et al. (1997) *Inorg. Chem.* **36**, 4676–4683.
- [4] Zachariasen, W. H. (1949) *Acta Crystallogr.* **2**, 388–390.

Incorporation of plutonium by magnetite under anoxic conditions

A. C. Scheinost, T. Dumas, A. Rossberg, D. Fellhauer,¹ X. Gaona,¹ M. Altmaier¹

¹Institute for Nuclear Waste Disposal, Karlsruhe Institute of Technology, Karlsruhe, Germany

Fe(II)-bearing secondary mineral phases, forming as corrosion products on steel containers, may greatly improve the retention of redox-sensitive radionuclides in nuclear waste repositories. Here we show that Pu(III) can be hosted by the magnetite structure in spite of its size incompatibility through rapid coprecipitation, but that it is expelled and re-adsorbed by aging.

Magnetite, which forms under anoxic conditions on the surface of corroding steel containers, is able to reduce a range of elements, including radionuclides of high relevance in the context of nuclear waste disposal, e.g. Se, Tc, U, Np, Pu [1]. Aqueous Pu(V) is rapidly reduced by nanoparticulate magnetite to Pu(III), which then forms stable, tridentate sorption complexes (³C) on the {111} faces of magnetite [2]. Trivalent lanthanides have been shown to substitute for Fe(III) in magnetite, although their ionic radii are about 1.4 times larger than that of Fe(III) (1.15–1.17 vs. 0.79 Å in six-fold coordination) [3]. To investigate if such an incorporation is also possible for Pu(III) with a similar ionic radius as the lanthanides, we conducted coprecipitation experiments.

EXPERIMENTAL. Pu-magnetite coprecipitation experiments were conducted at the KIT-INE laboratories (Karlsruhe, Germany) using well characterized (UV-vis), single-valent ²⁴²Pu(V) and ²⁴²Pu(III) stock solutions prepared electrochemically to obtain Pu loadings of 1000 and 3500 ppm. The two coprecipitates were investigated by X-ray absorption spectroscopy before and after Fe^{II}-induced aging [4]. Pu-L_{III} edge XANES (X-ray Absorption Near-Edge Structure) and EXAFS (Extended X-ray Absorption Fine-Structure) spectra were collected under cryogenic conditions (15 K) in fluorescence mode using a 13-element high-purity Ge energy-dispersive detector at the Rossendorf Beamline at ESRF, Grenoble (France).

RESULTS. UV-vis spectroscopy showed an immediate reduction of Pu(V) to Pu(III) in the initial Fe(II)/Fe(III) chloride solution. After formation of the black magnetite precipitate, Pu(III) concentration in solution was below 10⁻⁹ M. XANES spectroscopy confirmed the trivalent oxidation state of solid phase-associated Pu (not shown). EXAFS spectroscopy was then used to investigate the molecular structure of incorporated Pu(III) in the fresh precipitates as well as after Fe(II)-induced aging. The EXAFS spectra analyzed by Iterative Transformation Factor Analysis (ITFA) revealed two different spectral components. Component 1 (Fig. 1, top) represents Pu(III) in a highly distorted magnetite Oh site. Component 2 (Fig. 1, bottom) represents the tridentate Pu(III) sorption complex also observed during sorption experiments. ITFA was then used to derive their relative amounts, the proportion of the incorporated Pu(III) decreased from about 75% to 40% with Fe(II)-induced aging, while the proportion of sorbed Pu(III) increased correspondingly (Fig. 2). Our results suggest, therefore, that Pu can be incorporated by magnetite, but will convert to sorbed species on the long time scales relevant for nuclear waste disposal.

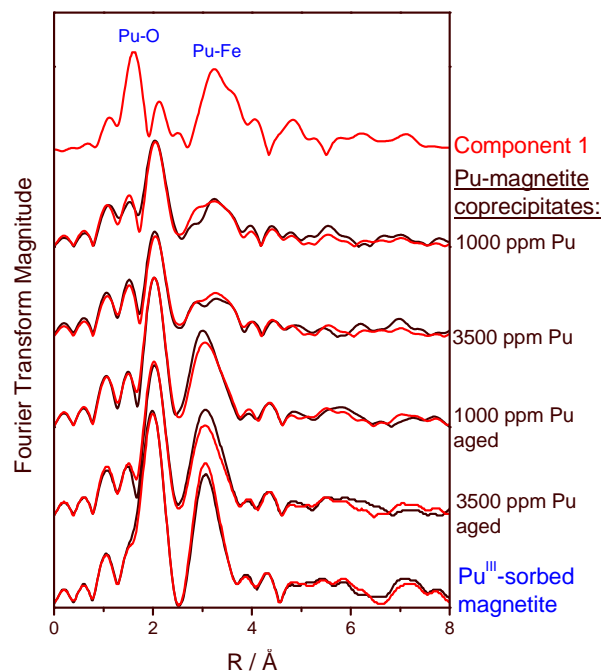


Fig. 1: Pu L_{III} edge EXAFS spectra of Pu/Fe coprecipitates before and after aging, and of sorbed Pu^{III}. Black lines are experimental data, red lines are ITFA-reproductions by two components.

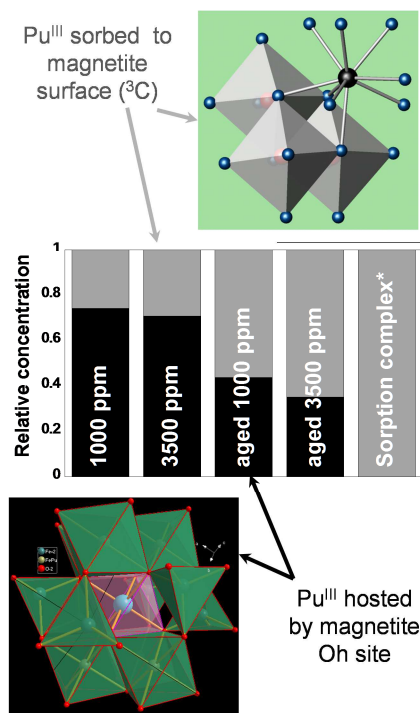


Fig. 2: Speciation of Pu/Fe coprecipitates, before and after aging as derived by ITFA from the EXAFS spectra shown above. Fractions of Pu^{III} ³C sorption complex are shown in gray, fractions of Pu^{III} incorporated by magnetite are shown in black.

- [1] Scheinost, A. C. *et al.* (2008) *J. Contam. Hydrol.* **102**, 228–245.
 [2] Kirsch, R. *et al.* (2011) *Environ. Sci. Technol.* **45**, 7267–7274.
 [3] Moon, J. W. *et al.* (2007) *Extremophiles* **11**, 859–867.
 [4] Boland, D. *et al.* (2011) *Environ. Sci. Technol.* **45**, 1327–1333.

Uptake of Se(VI) by hematite

N. Jordan, S. Domaschke,¹ H. Foerstendorf, A. C. Scheinost, C. Franzen, V. Zimmermann, S. Weiß, K. Heim

¹Fakultät Mathematik und Naturwissenschaft, Hochschule Zittau/Görlitz, Germany

Uptake of Se(VI) onto hematite was studied. Elevated temperature (up to 60 °C) reduced hematite retention capacities, through changes in its surface properties. *In situ* ATR FT-IR measurements revealed the formation of bidentate outer-sphere (OS) complexes (C_{2v} symmetry) during the sorption process, as formerly noticed for maghemite. EXAFS evidenced the additional presence of inner-sphere (IS) complexes in binuclear corner-sharing geometry. The ratio between OS/IS complexes was influenced by the Se surface loading.

Performance assessments of nuclear waste disposals evidenced the long-lived fission product ⁷⁹Se to be one of the most important contributors to the overall radiotoxicity. Hematite (α -Fe₂O₃) is a ubiquitous iron oxide in the environment and one of the corrosion products of stainless steel canisters. Here, batch and spectroscopic studies characterized the interaction of Se(VI) with hematite, which was so far not thoroughly investigated.

EXPERIMENTAL. Commercial hematite (US Research Nanomaterials) was used. The specific surface area was 41.1 m² g⁻¹ and absence of other Fe phases was verified by Mössbauer, XRD and IR. The detailed description of the performance of batch sorption studies, zeta potential measurements and *in situ* ATR FT-IR sorption experiments is given elsewhere [1].

RESULTS. Uptake of Se(VI) by hematite is at maximum in the acidic pH range and decreases with increasing pH (Fig. 1) and ionic strength (data not shown). EXAFS evidenced the absence of heterogeneous reduction of Se(VI) at the hematite surface (data not shown).

Elevated temperature (up to 60 °C) reduces the sorption of Se(VI) by hematite (Fig. 1) and consequently increases its mobility. Similar results were observed for anatase (TiO₂) [2].

Higher temperature neither changed the selenium aqueous speciation nor increased the solubility of hematite (data not shown). However, both the p*H*_{IEP} and zeta potential of hematite were significantly decreased upon increasing temperature (Fig. 2).

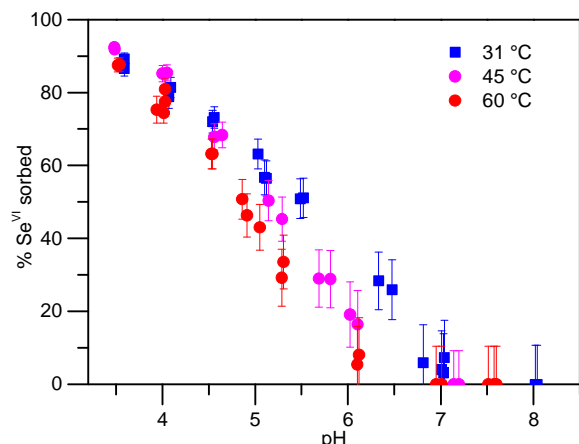


Fig. 1: Sorption edges of Se(VI) onto hematite. $m/v = 0.75 \text{ g L}^{-1}$, 0.1 M NaCl, $[\text{Se}^{\text{VI}}]_{\text{initial}} = 10^{-5} \text{ M}$, 2 days of shaking at three different temperatures (under N₂).

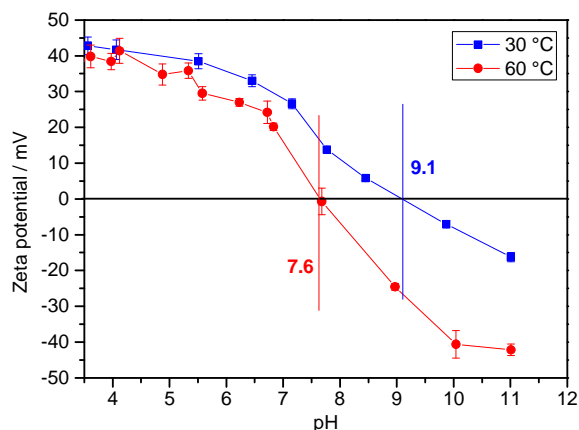


Fig. 2: Zeta potential of hematite at 30 and 60 °C. $m/v = 0.75 \text{ g L}^{-1}$, 0.1 M NaCl, 2 days of shaking (under N₂).

IR measurements (Fig. 3) revealed a fast formation of outer-sphere (OS) complexes, easily removed by flushing with NaCl solution. The tetrahedral symmetry (T_d) of the aqueous SeO_4^{2-} ions was reduced to C_{2v} upon OS complexation. The formation of OS bidentate complexes (C_{2v} symmetry) was again noticed as for maghemite [1,3]. However, EXAFS (data not shown) revealed the additional presence of a small portion (~20%) of bidentate corner-sharing inner-sphere (IS) complexes, in addition to OS complexes. The fraction amount of IS complexes was decreasing upon increasing Se surface loading.

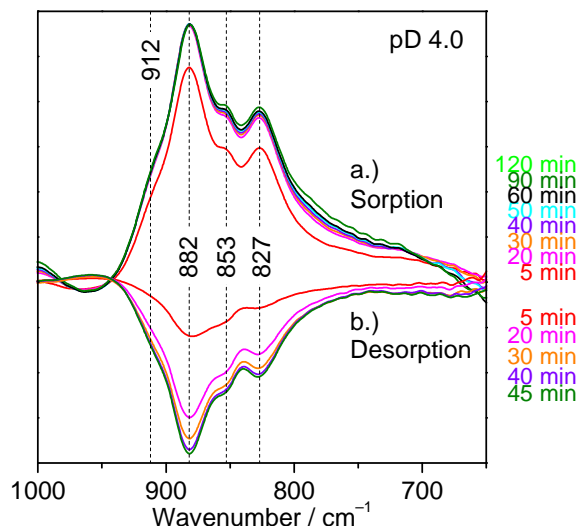


Fig. 3: (a) *In situ* ATR FT-IR spectra. (a) 500 μM sorbed on α -Fe₂O₃ (b) desorbed from α -Fe₂O₃ (D₂O, pD 4.0, 0.1 M NaCl, N₂). Indicated values are in cm⁻¹.

ACKNOWLEDGEMENTS Authors thank Heidrun Neubert and Aline Ritter for their support for batch experiments and ICP-MS measurements, respectively.

- [1] Jordan, N. et al. (2013) *Geochim. Cosmochim. Acta* **103**, 63–75.
 [2] Jordan, N. et al. (2013) *J. Colloid Interf. Sci.* **390**, 170–175.
 [3] Foerstendorf et al. (2012) *Report HZDR-013*, p. 50.

Retention of selenate at the water-mineral interface in the context of salt dome repositories

C. Franzen, D. Hering,¹ N. Jordan, S. Weiß, K. Heim

¹Fakultät Mathematik und Naturwissenschaft, Hochschule Zittau/Görlitz, Germany

In the present study, a combination of macroscopic sorption experiments, electrophoretic mobility and *in situ* ATR FT-IR spectroscopy measurements was used to study the interaction of selenate with γ -Al₂O₃ in the presence of NaCl and MgCl₂.

One major process controlling the mobility of selenium, a long-lived fission product found in nuclear waste, is the adsorption onto mineral. In this context, it is important to understand to what extent this sorption is influenced particularly by characteristic parameters as expected in deep underground. These parameters include *inter alia* the presence of different background salts which are important with regard to salt domes as potential repositories.

EXPERIMENTAL. Batch experiments were conducted at a solid-to-solution ratio of 1 g L⁻¹ and an initial Se(VI) concentration of 2×10^{-5} mol L⁻¹. The suspensions were equilibrated for 48 hours. All experiments were conducted in N₂ atmosphere. After centrifugation for two hours at 6,800 g, the remaining selenium concentration in the supernatant was determined by ICP-MS. The selenate sorption reactions onto γ -Al₂O₃ were investigated by *in situ* ATR FT-IR spectroscopy. The impact of salinity on the variable surface charge of γ -Al₂O₃ was evaluated by zeta potential measurements using laser Doppler electrophoresis. There, as well as for the batch experiments, corrections for H⁺ concentrations due to the high ionic strengths were done following Altmaier et al. [1].

RESULTS. From *in situ* ATR FT-IR spectra, a change in the symmetry of the aqueous tetrahedral selenate anion can be derived evidencing the formation of a surface complex on γ -Al₂O₃ (Fig. 1). From batch experiments, we observe a dependence of selenate sorption on the ionic strength and composition of the electrolyte. Additionally, the sorption generally de-

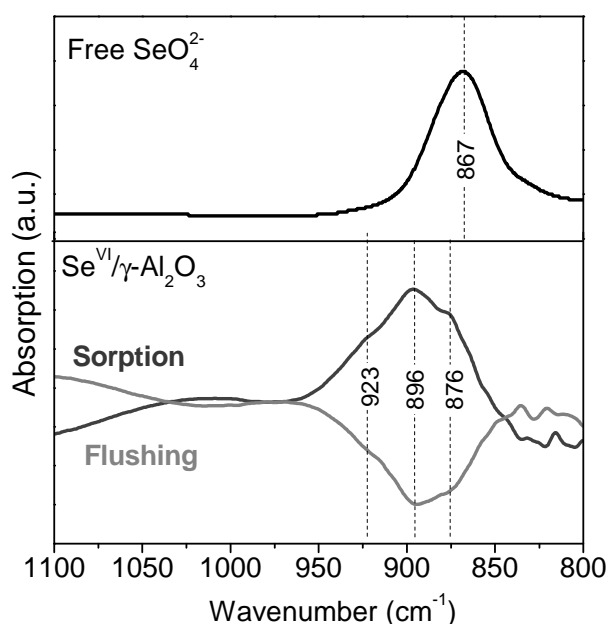


Fig. 1: IR spectra of the Se(VI) sorption onto γ -Al₂O₃, ([Se(VI)]_{ini} = 500 μ M; pD 4.0; I = 0.1 M NaCl).

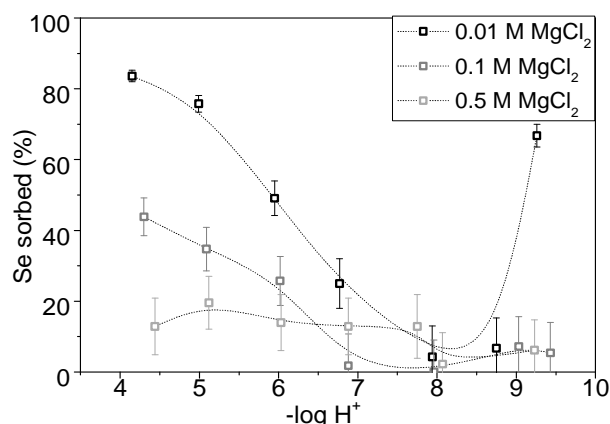


Fig. 2: Sorption edges of Se(VI) onto γ -Al₂O₃, $m/v = 1$ g L⁻¹, [Se(VI)]_{ini} = 2×10^{-5} M, under N₂.

creases with increasing pH. However, in the presence of 0.01 M MgCl₂ and a pH above 9 the percentage of removed Se from solution increased again (Fig 2).

The isoelectric point (pH_{IEP}) of γ -Al₂O₃ is located at pH 9.6 for low NaCl concentration (I = 0.1 M) which is consistent with literature [2]. The increase of ionic strength (up to I = 1 M) results in a decrease of the zeta potential for both the acidic and alkaline pH range. However, in the alkaline range the decrease of the zeta potential is more pronounced. Additionally, in the presence of MgCl₂, we observe that the pH_{IEP} is shifted to more alkaline values and at 0.1 M MgCl₂ no charge reversal is observed. Above pH 10, a sharp potential decrease occurs due to Mg(OH)₂ precipitation (Fig. 3).

The impact of the varied parameters on the retention of selenate in the alkaline pH range will be verified in detail.

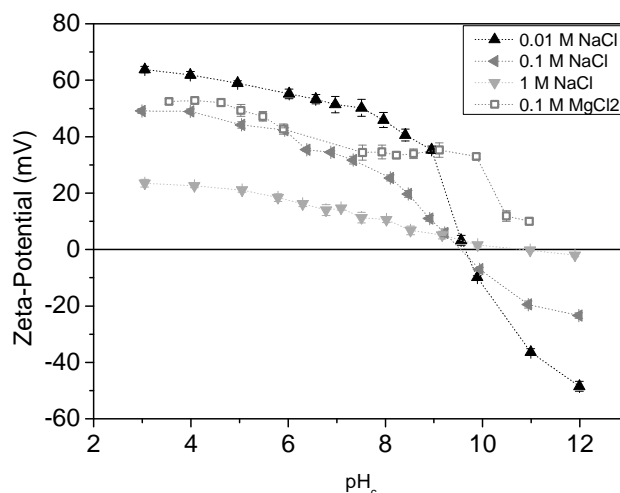


Fig. 3: Zeta potential of the neat surface of Al₂O₃; $m/v = 0.5$ g L⁻¹ at different background electrolytes.

ACKNOWLEDGEMENTS. Authors thank Aline Ritter for ICP-MS measurements.

[1] Altmaier, M. et al. (2003) *Geochim. Cosmochim. Acta.* **67**, 3595–3601.
[2] Kosmulski, M. (2006) *J. Colloid Interf. Sci.* **298**, 730–741.

Interaction of Ca^{2+} and Mg^{2+} with selenium oxyanions studied by ^{77}Se NMR

J. Kretzschmar, N. Jordan, E. Brendler,¹ C. Franzen, V. Brendler

¹Institute of Analytical Chemistry, Technical University Bergakademie Freiberg, Freiberg, Germany

Selenium-79 is a long-lived fission product found in nuclear waste. Due to its half-life of 3.27×10^5 years and mobility, it is expected to be one of the most important isotopes contributing to the potential radiation dose from nuclear waste repositories. The spin $\frac{1}{2}$ nucleus of the inactive isotope ^{77}Se is well suited to be directly observed by Nuclear Magnetic Resonance (NMR) spectroscopy. This method provides a valuable tool for probing the Se nucleus' electronic environment. Due to this structural sensitivity, the Se oxidation or protonation state as well as interactions with metal ions can be monitored. In the presence of Ca^{2+} and Mg^{2+} , the spectra clearly demonstrate changes in the Se chemical shifts, proving the interaction of selenium oxyanions with the divalent metal ions. These results serve as reference data for further investigations addressing the mobility and the sorption behavior in the presence of ubiquitous metal ions.

EXPERIMENTAL. Aqueous solutions containing 10% (v/v) of D_2O were prepared with sodium selenite or sodium selenate concentrations of 0.10 M under inert gas atmosphere. Appropriate amounts of $\text{CaCl}_2 \cdot 2\text{H}_2\text{O}$ or $\text{MgCl}_2 \cdot 6\text{H}_2\text{O}$ were added to yield metal concentrations of 0.05 and 0.10 M. The total ionic strength in all samples was set up to 5.6 m (background electrolyte: NaCl). Considering pH corrections, $-\log[\text{H}^+]$ was adjusted to 5 or 7.5 in the case of Se(IV) or Se(VI), respectively. Solution NMR measurements were carried out on a BRUKER DPX 400 using a 10 mm BBO probe, solid state NMR was performed on a BRUKER AVANCE 400 WB using a CP/MAS probe and a 4 mm ZrO_2 rotor. Both spectrometers operate at magnetic field strengths of 9.4 T, corresponding to a ^{77}Se resonance frequency of 76.4 MHz.

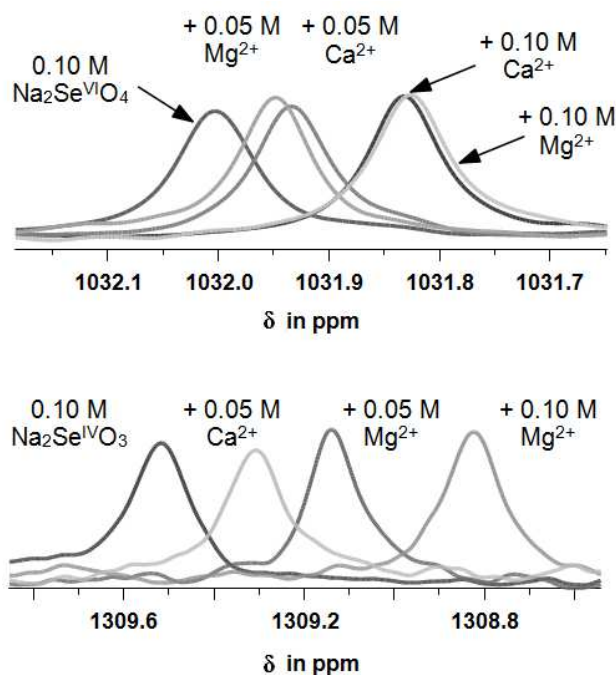


Fig. 1: Superimposed ^{77}Se NMR spectra of 0.1 M sodium selenate (top) and 0.1 M sodium selenite (bottom) solutions containing different amounts of calcium or magnesium ions; spectra referenced relative to 0.5 M Na_2SeO_4 , pH 9.6, using a coaxial insert.

RESULTS. In the presence of calcium or magnesium ions, the selenate and selenite signals are shifted in comparison to the free aqueous oxyanions. This highlights the interaction between selenium and these divalent metal ions (Fig. 1). The magnitude of the shift correlates with the selenium to metal ratio: the higher the ratio, the stronger the shift is. The observed shifts are significant, but weak. This agrees well with the high solubility as well as the low formation constants with $\log \beta \approx 2$ [1] for selenate(VI) complexes of magnesium and calcium ions. In contrast, the selenite(IV) sample containing an equimolar concentration of calcium showed precipitation. This precipitate was characterized by solid-state NMR (Fig. 2 and Tab. 1), IR, XRD and DTA/TG. Though being precipitated from a pH 5 solution, with the selenium(IV) predominating as hydrogen selenite (HSeO_3^-), the white microcrystalline solid consists of calcium selenite hydrate ($\text{CaSeO}_3 \cdot \text{H}_2\text{O}$) with $\delta_{\text{iso}} = 1273.7$ ppm. A second but minor (4%) component, presumably being a hydrogen selenite (HSeO_3^-) species, resonates at $\delta_{\text{iso}} = 1315.3$ ppm.

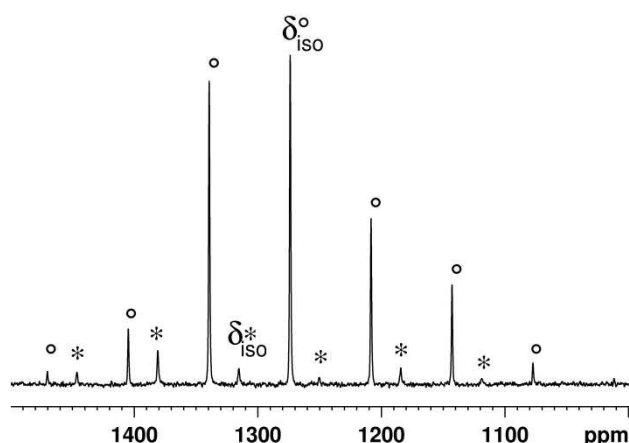


Fig. 2: ^{77}Se solid state CP/MAS NMR spectrum of the Se(IV)-calcium precipitate at a rotational frequency of 5 kHz; δ_{iso} and corresponding spinning sidebands (*, *).

Tab. 1: Analysis of CP/MAS spectra of the Se(IV)-calcium precipitate.

δ_{iso}	δ_{11}	δ_{22}	δ_{33}	Ω	K
1273.7	1396.4	1321.6	1103.1	293.3	0.49
1315.3	1443.7	1434.0	1086.1	375.6	0.95

* isotropic chemical shift $\delta_{\text{iso}} = 1/3(\delta_{11} + \delta_{22} + \delta_{33})$, with δ_{11} , δ_{22} , δ_{33} as principal components of the chemical shift tensor, defined as $\delta_{11} > \delta_{22} > \delta_{33}$ | span $\Omega = \delta_{11} - \delta_{33}$ | skew $\kappa = 3(\delta_{22} - \delta_{\text{iso}})/\Omega$ | δ in ppm.

To conclude, ^{77}Se NMR spectroscopy is a helpful tool in determining the aqueous speciation of selenium and its interactions with metal ions as well as to characterize the formed complexes in both the solution and the solid state. The results reveal the possibility of calcium ions to immobilize selenium in +IV oxidation state. However, neither calcium nor magnesium is able to precipitate and therefore immobilize selenium in its +VI oxidation state as it forms soluble complexes.

[1] Olin, Å. et al. (2005) *Chemical Thermodynamics of Selenium Vol. 7*, Elsevier, Amsterdam.

Hexanuclear Ce(IV)-formate in aqueous solution and its solid state structure

C. Hennig, A. Ikeda-Ohno,¹ W. Kraus,² S. Weiß, P. Pattison,³ H. Emerich,³ P. M. Abdala,³ A. C. Scheinost

¹School of Civil and Environmental Engineering, The University of New South Wales, Sydney, Australia; ²BAM Federal Institute for Materials Research and Testing, Berlin, Germany; ³Swiss–Norwegian Beamlines at ESRF, Grenoble, France

A hexanuclear Ce(IV) formate complex was identified in aqueous solution [1]. The related complex species $[\text{Ce}_6(\mu_3\text{-O})_4(\mu_3\text{-OH})_4(\text{HCOO})_x(\text{NO}_3)_y]^{12-x-y}$ was preserved in a crystal and its structure was determined.

The pH titration (with NH_4^+) of 0.1 M Ce(IV) in 0.5 M HNO_3 and 1.0 M HCOOH results in the formation of hexanuclear Ce(IV) formate complexes. The initial solution (sample INIT), i.e. in absence of HCOO^- , was investigated by Ce-K edge EXAFS and a dimeric complex $[\text{Ce}_2(\mu_3\text{-O})_a(\mu_3\text{-OH})_b(\text{NO}_3)_c]^{8-2a-b-c}$ was identified. In the presence of HCOO^- , pH titration leads to the increasing formation of a hexanuclear solution species with the common formula $[\text{Ce}_6(\mu_3\text{-O})_4(\mu_3\text{-OH})_4(\text{HCOO})_x(\text{NO}_3)_y]^{12-x-y}$. The distribution of the initial dimer and the final hexamer species during pH titration is shown in Fig. 1.

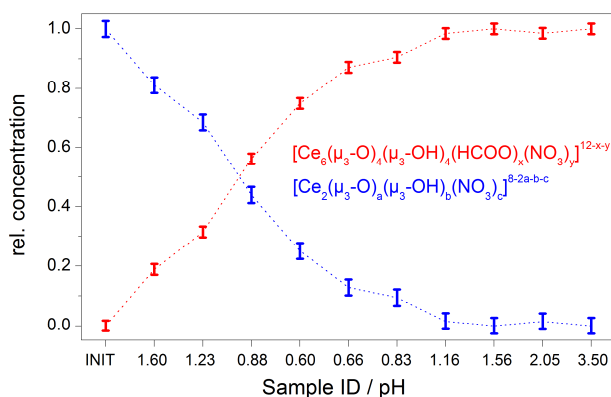


Fig. 1: Concentrations of the two solution species obtained by factor analysis of EXAFS spectra. The blue color represents the initial dimer species, while the red color represents the hexanuclear Ce(IV) formate complex.

Crystals were grown in the stability range of the hexanuclear species. The EXAFS spectrum of such crystals is identical to that of the solution at pH 3.50, suggesting that the structure of the solution species remains preserved in a crystal structure.

The structure of the complex is shown in Fig. 2. The Ce(IV) atoms in the hexanuclear core $[\text{Ce}_6(\mu_3\text{-O})_4(\mu_3\text{-OH})_4]^{12+}$ are arranged at the corners of a nearly regular octahedron. The eight faces of the octahedron are bridged by four $\mu_3\text{-O}$ and four $\mu_3\text{-OH}$ oxygen atoms. 10 out of the 12 edges of the octahedron are bridged by the carboxylic group of the HCOO^- ligands. Together with the 4 NO_3^- ligands in bidentate coordination, the complex should have a formal charge of -2 . However, the complex charge remains uncertain at that point. Because two out of the six Ce(IV) atoms show a coordination number of 8, and four Ce(IV) show a coordination number of 9, a mixed-valence $\text{Ce}^{3+}/\text{Ce}^{4+}$ complex cannot be excluded with certainty from determination of the bond valence alone. Due to strong disorder of the counter ions it was furthermore difficult to distinguish the electron density of the nitrogen atoms in NH_4^+ explicitly from that of the oxygen atoms in H_2O . Furthermore, the hydrogen atoms in this crystal structure could not be located experimentally. To exclude that the crystallization resulted in a mixed-valence struc-

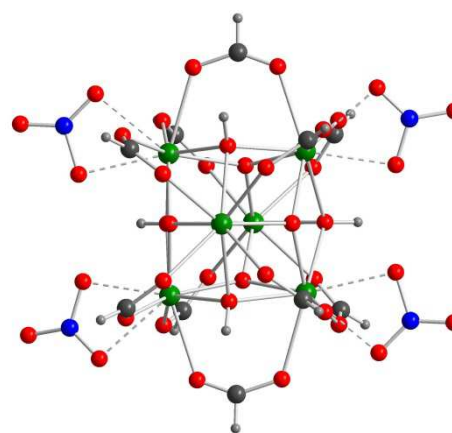


Fig. 2: $[\text{Ce}_6(\mu_3\text{-O})_4(\mu_3\text{-OH})_4(\text{HCOO})_{10}(\text{NO}_3)_4] \cdot (\text{NO}_3)_3(\text{NH}_4)_5(\text{H}_2\text{O})_5$. Color code: Ce green, O red, N blue, C large grey spheres, H small grey spheres.

ture, we verified the oxidation state of cerium by Ce L_3 -edge XANES (Fig. 3).

The Ce L_3 -edge spectrum of Ce(III) consists of a characteristic single peak just above the absorption threshold which is associated with the electron transition $2p^6 4f^1(5d,6s)^3 \rightarrow 2p^5 4f^1(5d,6s)^4$. The Ce L_3 -edge spectrum of Ce(IV) shows two resonances whose origin is interpreted as a result of mixed states between f^0 and f^1 or alternatively as an almost pure f^0 state related to the electron transition $2p^6 4f^0(5d,6s)^4 \rightarrow 2p^5 4f^0(5d,6s)^5$. A comparison of the structure shown in Fig. 2 with appropriate references reveals that the complex consists exclusively of Ce(IV), thereby confirming the stoichiometry of the hexamer complex.

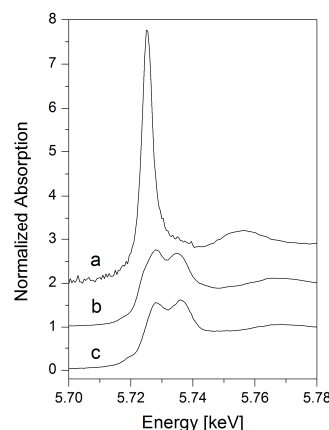


Fig. 3: Ce L_3 -edge XANES spectra: (a) Ce(III) reference of 0.01 M Ce(III) nitrate, (b) Ce(IV) reference of CeO_2 and (c) solid hexamer.

The hexanuclear complex forms by the competing hydrolysis and ligation reactions. The hydrolysis causes polymerization through olation and oxolation, while the ligation through chelating HCOO^- prevents further hydrolytic polymerization and stabilizes the hexanuclear complex in an aqueous solution.

[1] Hennig, C. et al. (2013) *Inorg. Chem.* **52**, 11734–11743.

EXAFS study of K-doped cobalt titanates for ethanol sensing

M. J. Lozano-Rodriguez, C. J. Belle,¹ G. E. Wesch,¹ S. Neumeier,^{1,2} A. C. Scheinost, U. Simon¹

¹Institute of Inorganic Chemistry, RWTH Aachen University, Aachen, Germany, ²Present address: Institute of Energy and Climate Research, Nuclear Waste Management and Reactor Safety (IEK-6), Forschungszentrum Jülich GmbH, Jülich, Germany

The performance of the p-type semiconductor CoTiO₃ as resistive gas sensor in car exhaust systems is significantly improved by volume-doping with K. Using X-ray absorption spectroscopy we could show that the local structure around Co and Ti remains unaffected by the doping despite of a slight increase in static disorder. Hence, the effect of K doping does not originate from alteration in the metal-to-oxygen interaction as expected from previous findings.

EXPERIMENTAL. Polycrystalline materials of undoped and K-doped CoTiO₃ were synthesized as published before [1,2]. EXAFS measurements were carried out at BM20 (ESRF, Grenoble). The spectra were collected at the Ti K (4966 eV) and Co K-edges (7709 eV) in transmission mode, using a He cryostat (15 K). The experimental spectra were Fourier Transformed using a Hanning window over k -space ranging 3.0–13.87 Å⁻¹ for Ti and 2.0–12 Å⁻¹ for Co. The Co and Ti edges were simultaneously refined using the Demeter code [3].

RESULTS. The experimental k^3 -weighted spectra of CoTiO₃ and CoTiO₃:K(A) and their Fourier Transform magnitudes (FT) are shown in Fig. 1. The EXAFS spectra at Ti K-edge are clearly different from those collected at Co K-edge, showing a different local coordination around the Ti and Co metals. In contrast, the differences between the samples of undoped and K-doped CoTiO₃ are very small and can only be seen when they are plotted on top of each other.

At the Ti K-edge, there are two FT peaks labelled as A₁ and A₂. The peaks A₁ and A₂ correspond to the single scattering (SS) contributions of Ti–O distances in the TiO₆ octahedron at 1.85 and 2.05 Å. The peaks B and C arise from the Ti···Co₁, Ti···Ti, Ti···Co₂ and Ti···Co₃ cation-cation interactions until 3.73 Å.

At the Co K-edge, the A' FT peak contains the SS contribution of the CoO₆ octahedra distances at 2.03 and 2.15 Å. The B' and C' FT peaks are the Ti···Co₁, Co···Co, Ti···Co₂, Ti···Co₃ cation-cation interactions until 3.73 Å. These inter-atomic distances are equal to the Ti paths and they were linked during the fit. Additional SS Co···Co and Ti···Co contributions between 5 to 6 Å were considered (D' peak).

The EXAFS results are given in Tab 1. The derived distances for CoTiO₃ are within ± 0.004 Å compared to the values derived by XRD for the same material. Comparison between CoTiO₃ and CoTiO₃:K(A) shows small changes in the CoO₆ and TiO₆ metal-oxygen distances (± 0.01 Å of error). The largest difference occurs for the Ti···Co₂ path which is 0.03 Å longer for CoTiO₃:K(A) while all other distances remain essentially the same. The most important K-induced change seems to be a higher static disorder as expressed by the reduced amplitudes in k and R-space, especially in the mid-range cation-cation interaction, i.e. B and C peaks. The increase of this static disorder is reflected by the increase of the Debye-Waller factors (σ^2) shown in Tab. 1. EXAFS did not detect any change in the atomic arrangement around Ti and Co in agreement with XRD measurements. Therefore the EXAFS-derived local structure did not provide any ex-

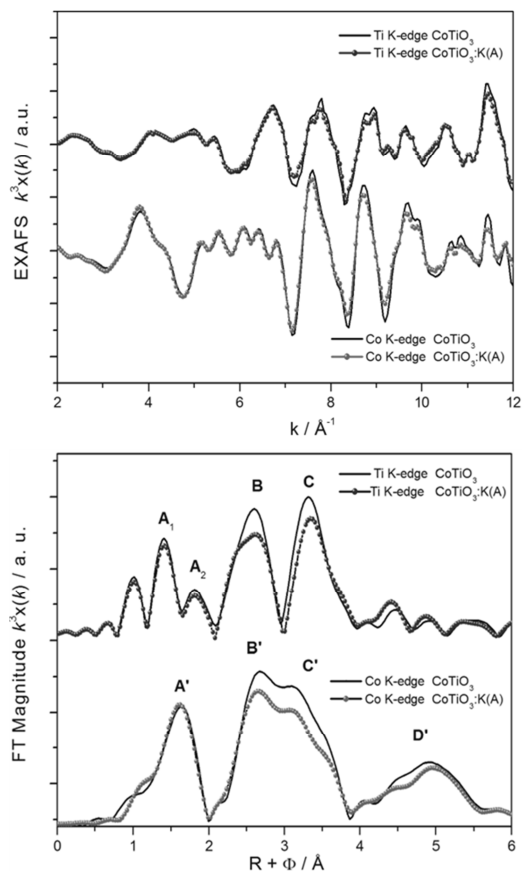


Fig. 1: EXAFS spectra of CoTiO₃ (full lines) and CoTiO₃:K(A) (dotted lines): k^3 -weighted spectra collected at Ti and Co K-edges (top) and corresponding Fourier Transforms (bottom).

Tab. 1: EXAFS data of the best fit obtained for CoTiO₃ and CoTiO₃:K(A).

	XRD		EXAFS		
	R(Å)		CoTiO ₃		CoTiO ₃ :K(A)
		R(Å)	σ^2 (Å ²)	R(Å)	σ^2 (Å ²)
Ti–O _{shorter}	1.87	1.85	0.0012	1.86	0.0017
Ti–O _{longer}	2.09	2.05	0.0012	2.05	0.0017
Co–O _{shorter}	2.05	2.03	0.0022	2.03	0.0011
Co–O _{longer}	2.17	2.15	0.0023	2.15	0.0010
^a Ti···Co ₁	2.92	2.89	0.0010	2.88	0.0003
Co···Co	2.99	2.98	0.0010	2.98	0.0015
Ti···Ti	2.98	3.01	0.0010	3.02	0.0013
^a Ti···Co ₂	3.40	3.42	0.0045	3.45	0.0058
^a Ti···Co ₃	3.73	3.73	0.0033	3.73	0.0042

^a Distances and Debye-Waller factor correlated during the simultaneous fit of Ti and Co data.

planation for the improvement K-doping on the ethanol sensing properties of CoTiO₃.

- [1] Belle, C. J. et al. (2014) *Sens. Actuator B-Chem.* **192**, 60–69.
 [2] Siemons, M. et al. (2007) *Sens. Actuator B-Chem.* **254**, 669–676.
 [3] Ravel, B. et al. (2005) *J. Synchrotron Rad.* **12**, 537–541.

Environmental transport of TiO₂ nanoparticles

S. Schymura, H. Hildebrand, K. Franke¹

¹Institute of Radiopharmaceutical Cancer Research, HZDR, Dresden, Germany

The mobility of TiO₂ nanoparticles (NPs) in water saturated glass bead columns was investigated by means of radiotracer methods. With ideal transport conditions, an almost unhindered transport was found, while the presence of salt lead to their considerable retention. Adsorption of non-aggregated NPs is the dominant removal mechanism shown by reference experiments under ideal adsorption conditions. Under the chosen geochemical transport conditions filtration of agglomerated NPs plays only an insignificant role.

EXPERIMENTAL. We labeled commercial TiO₂ nanoparticles (P25, Degussa) by activation through 13.4 MeV proton irradiation at the Ispra cyclotron, Italy. ⁴⁸V (T_{1/2} = 15.97 d) is formed inside the NPs via a (p,n) reaction from ⁴⁸Ti [1].

NP transport experiments were conducted with 1 × 8 cm glass columns filled with glass beads (450–600 μm) and equilibrated with a 5 mg/L fulvic acid (FA) solution. A 100 μL tracer pulse of a FA-stabilized [⁴⁸V]TiO₂-NP suspension (1 mg/L TiO₂ in 5 mg/L aqueous FA) was injected into the eluent. The retention of the NPs on the column was measured by gamma counting after a throughput of four pore volumes.

RESULTS. TiO₂ NPs could be stabilized in suspension using 5 mg/L fulvic acid (FA, isolated from bog water, Kleiner Kranichsee, Germany, according to [2]). Under these conditions, the NPs as well as the glass matrix equilibrated with a FA show a strongly negative zeta potential (potential at the slipping plane between particle and solution, Tab. 1). Under such repulsive conditions, the TiO₂ NPs behave as a conservative system component with retrieval rates close to 100% (Fig. 1, left).

Tab. 1: Zeta potential [mV] of TiO₂ nanoparticles and matrix (glass beads), under different conditions.*

Conditions	TiO ₂ NPs	Matrix
5 mg/L FA	-41.8	-50.3
5 mg/L FA + 10 mM Ca(NO ₃) ₂	-12.3	-12.6
CTAB	+41.3	
Dist. water	-	-35.0

*pH was set by components; 5 for FA; 6 for CTAB and water.

With the addition of salt (10 mM Ca(NO₃)₂), Ca²⁺ screens the repulsive electrostatic forces considerably and brings up the zeta potential of the NPs and matrix to -12.3 mV and -12.6 mV, respectively. In line with common knowledge on suspensions turning instable if the zeta potential is falling below an absolute value of ± 30 mV [3], we observed a removal of about 47% of the TiO₂ NPs from the eluent after passing through the column.

To distinguish between the two possible removal mechanisms, filtration of aggregated particles and adsorption of non-aggregated particles on the matrix, a third reference experiment was conducted. It aimed at preventing agglomeration while providing ideal adsorption conditions. This was achieved by producing a micelle free suspension of TiO₂ NPs using the surfactant cetyltriethyl ammonium bromide (CTAB) creating a positive surface charge on the

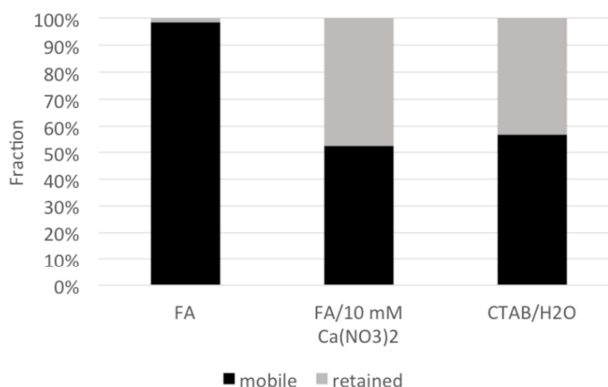


Fig. 1: Fractions of retention and retrieval of NPs after four pore volumes under “ideal transport conditions”, with salt added and “ideal adsorption conditions” (from left).

NPs [4]. This stabilizes the NPs in suspension preventing aggregation and consequently a filtration process on the column. Further, the glass matrix was conditioned only with distilled water resulting in a negative surface potential (Tab. 1), so that adsorption of the NPs is well possible due to the attractive interactions between particles and matrix.

With this third experiment, a similar fraction of NPs was removed as with the addition of 10 mM Ca(NO₃)₂ to a fulvic acid stabilized suspension. This clearly indicates that *adsorption* of NPs onto the geomatrix is the dominant process for the retention in hard water – not *filtration* of aggregates.

ACKNOWLEDGEMENTS. We kindly acknowledge funding from the BMBF (support code 03X007881) and the Qualitynano Transnational Access Program of the European Commission (JRC-TAF-13, JRC-TAF-119, JRC-TAF-168). Thanks to Dr. Neil Gibson and group for the help with the radiolabeling and Dagmar Lösel and Claudia Schöbner for the assistance during the course of this project.

[1] Kamel, A. et al. (2010) *J. Nanopart. Res.* **12**, 2435–2443.

[2] Lin, D.H. et al. (2010) *J. Environ. Qual.* **39**, 1896–1908.

[3] Thurman, E. et al. (1981) *Environ. Sci. Technol.* **15**, 463–466.

[4] Dolle, S. et al. (2012) *Angew. Chem. Int. Ed. Engl.* **51**, 3254–3257.

Solid-state properties and colloidal stability of thorium(IV)-silica nanoparticles

C. Hennig, S. Weiß, D. Banerjee,¹ V. Honkimäki,¹ E. Brendler,² G. Cuello,³ A. Ikeda-Ohno,⁴ A. C. Scheinost, H. Zänker

¹European Synchrotron Radiation Facility, Grenoble, France; ²Technical University Bergakademie Freiberg, Freiberg, Germany; ³Institute Laue-Langevin, Grenoble, France; ⁴School of Civil and Environmental Engineering, The University of New South Wales, Sydney, Australia

In the presence of silica, thorium(IV) forms meta-stable colloids in aqueous solutions at pH ≥ 7. Such colloids might be mobile in the natural aquatic environment. The structure of the amorphous colloids was comprehensively investigated and compared to the crystalline structures α-ThSiO₄ and β-ThSiO₄ [1].

Thorium-silica colloids were prepared by dilution of thorium carbonate in silicic acid solutions. Zeta potential measurements indicate a negative surface charge of the colloids at neutral pH range. The nanoparticles were removed from the solution by neutralizing their surface charge through slow acidification of the suspension. Investigation with TEM did not reveal any ordered domains in the structure of the particles, hence, they can be regarded as amorphous. This is in line with the observation that X-ray powder diffraction does not show Bragg reflections.

Structural disorder may induce destructive interference effects in EXAFS spectra. The effect of disorder can be investigated by comparing α-ThSiO₄ and β-ThSiO₄ (Fig. 1). α-ThSiO₄ has four identical Th–Th distances whereas β-ThSiO₄ has six different Th–Th distances. It is evident that highly symmetric α-ThSiO₄ exhibits a well resolved Th scattering peak in EXAFS, whereas β-ThSiO₄ shows a disturbed signal. This destructive effect becomes even more pronounced in the spectra of colloidal Th(IV)-silica particles. Th–Si distances are 3.25 ± 0.02 Å in the Th(IV)-silica colloid particles.

Real-space analysis of high-energy X-ray scattering (HEXS) is sensitive to the local structure even in the case of structural disorder (Fig. 1). All colloid samples show a

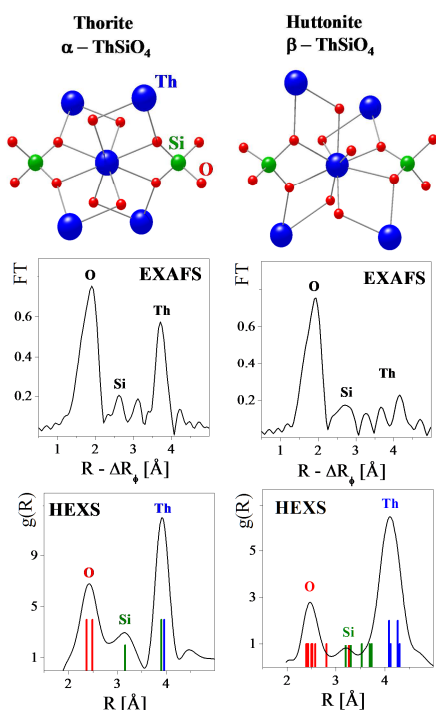


Fig. 1: Comparison of EXAFS and HEXS of crystalline α-ThSiO₄ (left) and β-ThSiO₄ (right). A simplified picture of the coordination is given on top.

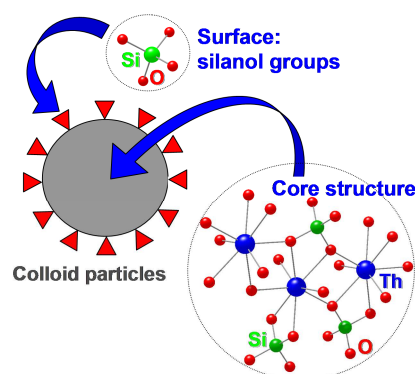


Fig. 2: Structure model of amorphous Th(IV)-silica colloid particles.

relatively strong peak from a Th–Th distance of 3.98 ± 0.01 Å in HEXS measurements. The Th–Th and Th–Si distances are indicators for a structural similarity in the near-order of the amorphous Th-silica colloids and the crystalline ThSiO₄ structures. Neutron scattering was performed on deuterated colloid particles. It reveals a strong peak at an O–D distance of 0.96 ± 0.01 Å. This peak indicates the presence of hydroxo groups in the colloids. The presence of oxo and hydroxo groups in the colloid structure was confirmed by O1s XPS. This observation underlines the structural differences of the oxyhydroxide nature of Th-silica colloids and the oxide nature of ThSiO₄. Solid state ²⁹Si NMR was used to investigate whether the silica ions remain isolated in the colloid structure as in orthosilicates or if polymerization of silica units occurs. Colloids with increasing Si/Th ratio and silica concentrations above the silica solubility limit reveal an increasing number of Si–O–Si bonds, i.e. increasing polymerization. To summarize the experimental results, a structure model of the colloid core is shown in Fig. 2.

A comparison of quantitative XPS data with the chemical analysis of the bulk is well suited to determine whether the surface of a sample is identical to the volume composition or not. XPS is surface sensitive to an excitation depth of 5–10 Å. The size of the Th-silica colloids is in the range of < 7 to 20 nm. The surface and the volume composition of the colloids were compared using quantitative XPS data and chemical analysis of the bulk colloid samples by means of ICP-MS. Three colloid samples with molar Si/Th ratios of 0.46, 0.73 and 1.45 were investigated. The Si/Th ratios of the first two samples were found by XPS to be 0.41 and 0.78 which shows good agreement with the bulk composition. The sample with a Si/Th ratio of 1.45 in the bulk has a Si/Th ratio of 2.77 at the surface, showing silica enrichment at the colloid surface due to the silica excess in the initial solution.

In conclusion, the bulk composition indicates oxyhydroxo-type colloids [(Th,Si)_n(OH)_{4-n} · xH₂O]⁴⁻²ⁿ⁻⁽⁴⁻ⁿ⁾. The presence of structural silica groups at the colloid surface, possibly charged silanol groups, may contribute to the negative surface charge, and thus, to the stability of the colloid suspensions [2].

[1] Hennig, C. et al. (2013) *Geochim. Cosmochim. Acta.* **103**, 197–212.

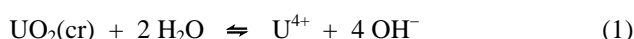
[2] Zänker, H. et al. (2014) *J. Contam. Hydrol.* **157**, 87–105.

The nanocrystallinity of “amorphous” uranium(IV) oxyhydroxide

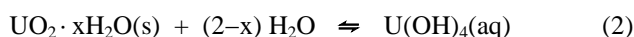
H. Zänker, S. Weiß, I. Ulbricht, R. Husar

“Amorphous” U(IV) oxyhydroxide is not really amorphous but nanocrystalline, even if precipitated from the alkaline side of the pH scale. This questions the current theory of U(IV) oxyhydroxide formation.

The crystalline actinide dioxides are assumed to be the thermodynamically stable oxides of the tetravalent actinides. They possess the Fm3m fluorite lattice structure with the face-centered cubic actinide(IV) sublattice. They are extremely insoluble under environmental conditions [1,2]. Calculated solubilities of these oxides at near neutral to alkaline pH lie in the range of 10^{-16} to 10^{-14} M [1]. In aqueous ambient, the crystalline uranium dioxide, e.g., is in equilibrium with the dissolved U^{4+} ions [1]:



Significant amounts of free U^{4+} ions only exist in strongly acidic solutions; $UO_2(\text{cr})$ should, therefore, only be formed in acidic solutions. In the weakly acidic to near-neutral pH region, on the other hand, the U(IV) solid is in equilibrium with the neutral hydroxo complex $U(\text{OH})_4(\text{aq})$ [1]:



The product of this reaction is called amorphous U(IV) oxyhydroxide, $UO_2 \cdot xH_2O(\text{am})$, in the literature (cf. [1]). Amorphous U(IV) oxyhydroxide has a much higher solubility than the corresponding crystalline solid. A value of about 10^{-9} to 10^{-8} M is observed. It was recommended in the literature that performance assessment calculations concerning the long-term behavior of actinides such as uranium in the environment be based on the solubility values of amorphous actinide(IV) oxyhydroxides and not on the extremely low solubilities resulting from the thermodynamic data of the crystalline actinide dioxides [3].

It has long been more or less taken for granted that the solid generated by reaction (2) is an amorphous oxide. However, how “amorphous” is this product? The classification of $UO_2 \cdot xH_2O(\text{am})$ as amorphous solid results from the finding that no crystallinity is unambiguously detectable by means of X-ray diffraction for oxidic U(IV) precipitates generated at $\text{pH} > 3$ [4]. Thus, the “amorphous” U(IV) oxyhydroxide formed at room temperature is X-ray amorphous. But is it also “nanoamorphous”? A closer look into the structure of the “amorphous” U(IV) oxyhydroxide by high-resolution transmission electron microscopy (HR-TEM) revealed that this solid shows nanocrystallinity of the Fm3m lattice type with crystallites of very few nanometers in size [4].

The nanocrystallinity of U(IV) precipitated at near-neutral pH is not easy to understand since the formation of $UO_2(\text{cr})$ suggests equilibrium according to equation (1) whereas the lack of free U^{4+} ions at near-neutral pH should rule out equilibrium (1) and exclude the formation of $UO_2(\text{cr})$.

Rousseau’s experiment resulting in “amorphous” uranium(IV) oxyhydroxide, which was proven to be nanocrystalline by HR-TEM, was started at the acidic side of the pH scale. In other words, it was done by neutralizing strongly acidic U(IV) solutions. In such experiments, at least at the beginning of the titration, equilibrium (1) is

valid and there is a phase during which free U^{4+} ions are still abundant in the solution. We asked ourselves if this initial period (which is also the period of intensive U(IV) oxide nucleation) might play a special key role for the structure of the final precipitation product. If equilibrium (1) does not play a role (and the existing theoretical explanations are correct), only the formation of $UO_2 \cdot xH_2O(\text{am})$ should be expected over the whole time period of precipitation and the occurrence of crystalline domains in the HR-TEM images should be hindered. In order to test this hypothesis and to improve our understanding of U(IV) precipitate crystallinity evolution, we tried to suppress the influence of equilibrium (1) and the role of free U^{4+} ions by producing the U(IV) precipitate from carbonate-containing alkaline solutions. In such solutions, the uranium(IV) exists as soluble carbonate complexes. Acidification of such solutions results in the destruction of the U(IV) complexes and the formation of oxidic U(IV) colloids or precipitates with minimal influence of free U^{4+} ions.

Figure 1 demonstrates that also the U(IV) oxyhydroxide produced from the alkaline side of the pH scale shows nanocrystallinity. The figure very much resembles the HR-TEM images obtained by Rousseau et al. for “amorphous” U(IV) oxyhydroxide produced by increasing the pH of strongly acidic U(IV) solutions [4]. Obviously, U(IV) oxyhydroxide shows nanocrystallinity no matter if produced from acidic or from alkaline solutions. This indicates that the currently existing theoretical explanations of U(IV) oxyhydroxide formation based on equations (1) and (2) are still incomplete and need reconsideration.

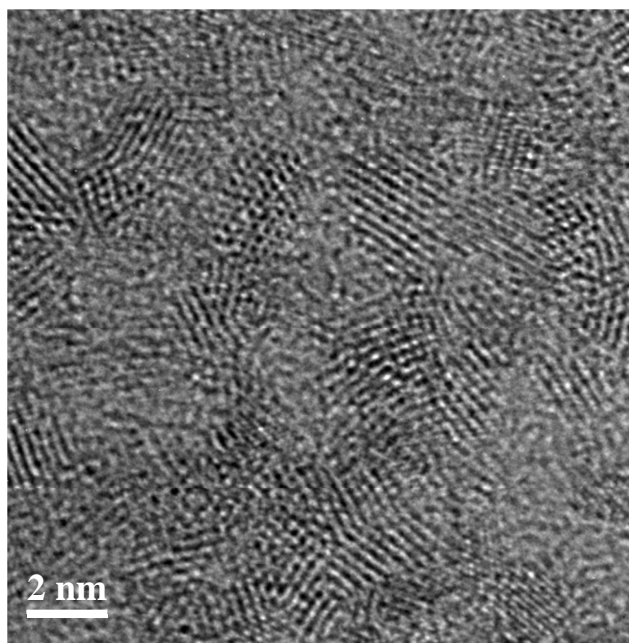


Fig. 1: HR-TEM image of a cluster of UO_2 nanocrystals produced by acidification of a carbonate-containing alkaline U(IV) complex solution.

[1] Neck, V. et al. (2001) *Radiochim. Acta* **89**, 1–16.

[2] Opel, K. et al. (2007) *Radiochim. Acta* **95**, 143–149.

[3] Altmaier, M. et al. (2004) *Radiochim. Acta* **92**, 537–543.

[4] Rousseau, G. et al. (2009) *J. Solid State Chem.* **182**, 2591–2597.

Dependence of morphology and dispersion of neptunium(IV) silica nanoparticles on silica content

R. Husar, S. Weiß, R. Hübner,¹ H. Zänker

¹Institute of Ion Beam Physics and Materials Research, HZDR, Dresden Germany

Neptunium(IV) is stabilized in a colloidal borne form by an excess of silica under insoluble conditions. Exclusively dispersions characterized by particle diameters < 50 nm are long-term stabilized. Variation of the silica content revealed varieties in morphology of the synthesized solids. Herein the silica–Np(IV) ratio is crucial for the formation and stabilization of Np(IV) silica colloids.

In the near and far field of nuclear waste repositories, in principle related with reducing conditions, a prevailing oxidation state of actinides (An) is the tetravalent one. Due to their low solubility at near-neutral pH, An(IV) are assumed to be immobile: exceeding the solubility limit in ultrapure water leads to the formation of An(IV) oxyhydroxide precipitations [1,2]. However, the expected sedimentation behavior is prevented in the presence of ubiquitously occurring silicate and results in the formation of more or less stabilized An(IV) silica colloids [3–5]. Herein, the stability of An(IV) silica dispersions is related to the silica content of the particles: increased silica uptake in Th(IV) and U(IV) systems enhances the effective surface charge (maybe through concentration of silanol groups on the surface) in pH range 6–8 and stabilizes the resulting dispersion due to repulsive forces between the particles. The sensitive colloidal stability at near-neutral pH is limited through the balanced ratio of particle size, surface charge and weight, finally due to the composition and morphology of An(IV) silica particles in dependence of the silica content. We investigate the influence of the silica uptake on the stability of Np(IV) silica particles.

EXPERIMENTAL. Neptunium silicate colloids were prepared from a pure and truly dissolved Np(IV) carbonate precursor by dilution in fresh hydrolyzed silica under anaerobic conditions. In dependence of initial silica concentration the silica uptake into colloids was determined by ICP-MS (content of initial solution related to supernatant after ultrafiltration with 5-kDa devices). Dispersion stability and the corresponding particle size distribution were monitored by scattered light intensity (SLI) and dynamic light scattering (DLS). In all experiments, the concentration of Np(IV) was kept constant at 1×10^{-3} M, whereas the concentration of silica was varied between 0.5 and 9×10^{-3} M in ionic strength of 1×10^{-1} M NaHCO_3 . Precipitates of Np(IV) silica particles were isolated by acidification or addition of NaNO_3 in excess and investigated concerning morphology and composition by transmission electron microscopy (TEM).

RESULTS. The synthesis at various initial silica concentration yielded amorphous silica-enriched Np(IV) particles of different amorphous composition (inset Fig. 1). The SLIs over time in dependence of the silica content are displayed in Fig. 1: only the systems with ninefold excess of silica in the initial solution exhibit a SLI increase indicating particle growth and long-term stable colloidal systems. Results of DLS measurements proved the increase of particles size with diameters of ~ 3 nm in fresh hydrolyzed solution

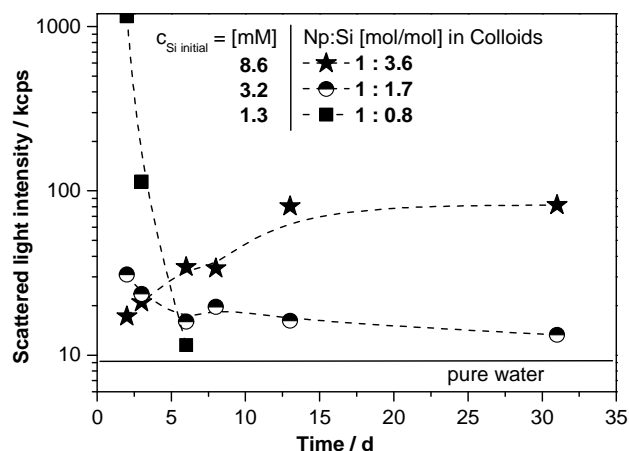


Fig. 1: Scattered light intensity of Np(IV) silica colloids in dependence on silica concentration (initial solution and uptake into solids) and time.

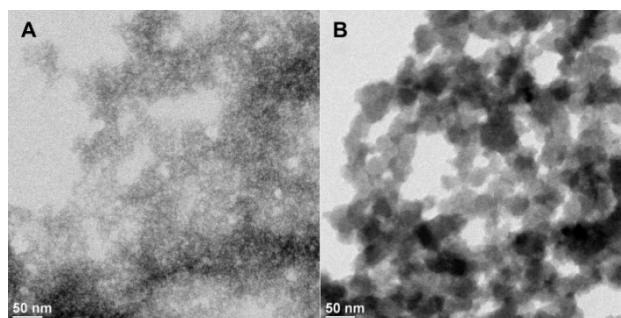


Fig. 2: Bright-field TEM images of Np(IV) silica particles for two different initial silica concentrations and $n_{\text{Np}}/n_{\text{Si}}$ -ratios: (A) $c_{\text{Si}} = 2 \times 10^{-3}$ M with $n_{\text{Np}}/n_{\text{Si}} = 1 : 2$; (B) $c_{\text{Si}} = 9 \times 10^{-3}$ M with $n_{\text{Np}}/n_{\text{Si}} = 1 : 9$.

and < 50 nm after aging for three weeks. The particles poor in silica tend to quantitative sedimentation due to the formation of relatively large particles (~ 1.5 μm). Hence, they are not long-term stabilized. Transition forms exhibit weak SLI, but are also obviously precipitated. TEM confirmed the outcome of DLS investigations: silica-poor systems reveal particles in the micron-range which consist of irregular cross-linked hydrolyzed Np(IV) silica compartments (Fig. 2A). In contrast, long-term stabilized and silica-enriched systems are characterized by isolated particles with an average particle size of 45 nm. Agglomerates of such isolated Np(IV) silica particles are displayed in Fig. 2B. They appear as consolidated amorphous solids with a densely closed surface and exhibit no internal fractures. The latter mentioned morphology of Np(IV) silica particles might facilitate the migration behavior of Np(IV) in a stabilized colloidal form under environmental conditions.

[1] Altmaier, M. et al. (2004) *Radiochim. Acta* **92**, 537–543.
 [2] Neck, V. et al. (2001) *Radiochim. Acta* **89**, 439–446.
 [3] Dreissig, I. et al. (2011) *Geochim. Cosmochim. Acta* **75**, 352–367.
 [4] Hennig, C. et al. (2013) *Geochim. Cosmochim. Acta*, **103**, 197–212.
 [5] Husar, R. et al. (2013) *Report HZDR-030*, p. 52.

Thermodynamic database for lanthanides: procedures and guidelines

V. Brendler, F. Bok, N. Jordan, A. Heller, M. Stockmann, C. Joseph, A. Barkleit, J. Schott, C. Richter

An extensive literature review of thermodynamic data for inorganic aqueous europium complexes has been performed. The critically assessed data have been processed to obtain thermodynamic data for the standard state, along with some ion-ion-interaction parameters applicable for the SIT approach.

Our society is facing a steadily increasing demand for high technology products, many of them incorporating Rare Earth Elements (REE). The growing demand for these elements simultaneously meets a significant shortage on the global market, creating the need for improved REE production and recycling. Accurate and reliable thermodynamic data are mandatory for respective optimizations. Namely for europium, several reviews and systematic studies focusing on the aqueous chemistry are available [1–6]. Complexation constants were determined by very different techniques such as solvent extraction, potentiometry, ion exchange, and spectroscopies (fluorescence, UV-vis). However, the different experimental conditions (ionic strength, temperature, lanthanide concentration, pH range, etc.) and methodologies had negative consequences on both consistency and accuracy. Thus, a thermodynamic database project for Eu was started.

DATA PROCESSING. An extensive data survey of more than 290 publications provided a nominally high number of data records for the above mentioned subset of aqueous Eu complexes, cf. Tab. 1. However, many of them had to be discarded, mainly due to the following reasons:

- inadequate description of experimental conditions,
- use of pH buffers acting as complexants,
- no original data but rather analogue values from other REE or compilations from secondary references,
- missing details for extrapolation to infinite dilution,
- postulation of species not independently evidenced.

Tab. 1: Summary of the aqueous inorganic Eu complexation data records.

System	#total	#selected
Eu-hydroxide	101	53
Eu-fluoride	124	51
Eu-chloride	201	67
Eu-nitrate	154	91

The remaining selected experimental data were processed adapting the OECD-NEA method to determine the $\log K$ value for standard conditions [7]: First, consistency checks had to select those data records that actually could be grouped because they operated on similar species sets. Then the $\log K$ values for the species formation reaction were plotted as a function of ionic strength using equation 1 to obtain $\log K^\circ$ values and SIT interaction parameters.

$$\log K^\circ = \log K - \Delta z_i^2 D + \Delta \epsilon m_x - n \log a_{\text{H}_2\text{O}} \quad (1)$$

As an example, the $\log K^\circ$ fitting for the formation reaction of the 1:1 fluoro complex is given in Fig. 1. Before such fitting exercises, reasonable errors had to be assigned, avoiding both unrealistic low values given in

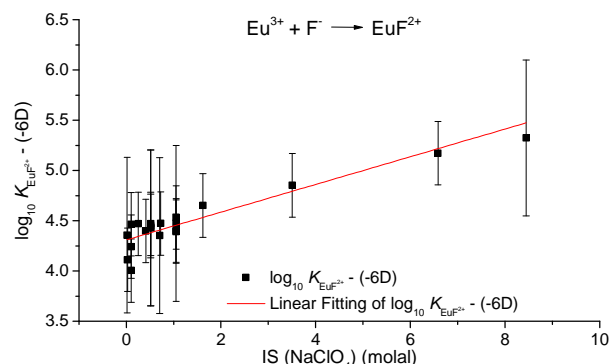


Fig. 1: Linear fitting of the $\log K$ values for the formation reaction of the the EuF^{2+} complex.

some papers as well as errors above a threshold of about 0.6 in $\log K$ which would render respective values obsolete. The weighing factors were set to $1/\sigma$ to avoid a domination of the fit by only a few values with very low uncertainties.

If there are insufficient data for the fitting of the $\log K^\circ$ value for a specific aqueous complex formation equation, the experimental $\log K$ were converted to zero ionic strength using the SIT approach with the interaction parameters given in the literature [7] and a weighted mean value was calculated based on their experimental errors. Here, however, it must be pointed out that many of the SIT interaction parameters published so far for REE are estimates themselves, sometimes based on very weak analogy considerations.

CONCLUSIONS. The data selection and processing methodology described here yielded the so far most comprehensive and reliable thermodynamic database for Eu complexes with hydroxide, fluoride, chloride, and nitrate. Benchmark results underpinning this statement are presented in [8]. Currently, the database is expanded towards aqueous Eu complexes with carbonates and sulfates.

ACKNOWLEDGEMENTS. The authors wish to thank D. Litskevich for his valuable translations of many Russian papers.

[1] Curti, E. (2000) *PSI Report TM-44-00-04*.
 [2] Rard, J.A. (1987) *Update of the europium data base*, LLNL Internal Memo, Livermore, U.S.A.
 [3] Luo, Y.R. et al. (2007) *J. Solut. Chem.* **36**, 673–689.
 [4] Millero, F.J. (1992) *Geochim. Cosmochim. Acta* **56**, 3123–3132.
 [5] Spahiu, K. et al. (1995) *A selected thermodynamic database for REE to be used in HLNW performance assessment exercises*, Swedish Nuclear Fuel and Waste Management Co., Stockholm, Sweden.
 [6] Wood, S.A. (1990) *Chem. Geol.* **82**, 159–186.
 [7] Gamsjäger, H., et al. (2012) in: *Chemical Thermodynamics Volume 12: Chemical Thermodynamics of Tin*, OECD Publications, Paris, France, p. 438–481.
 [8] Bok, F. et al. (2014) this report, p. 47.

Europium-TDB: review of thermodynamic data for Eu(III) complexation with inorganic ligands – First test results

F. Bok, V. Brendler

An extensive literature review of thermodynamic data for europium speciation has been performed and the critically assessed data have been processed to obtain thermodynamic data for the standard state [1]. Computed speciations based on them were successfully compared with experimental results.

TEST CALCULATIONS RESULTS. To test the quality of the obtained Eu data set, the aqueous speciation of europium was calculated for conditions where experimental speciation patterns were published [2,3]. Identical calculations were performed with other Eu containing databases (Nagra/PSI [4], THERMODDEM [5], LLNL and LLNL-V8-R6-“combined” [6]) (Fig. 1 & 2).

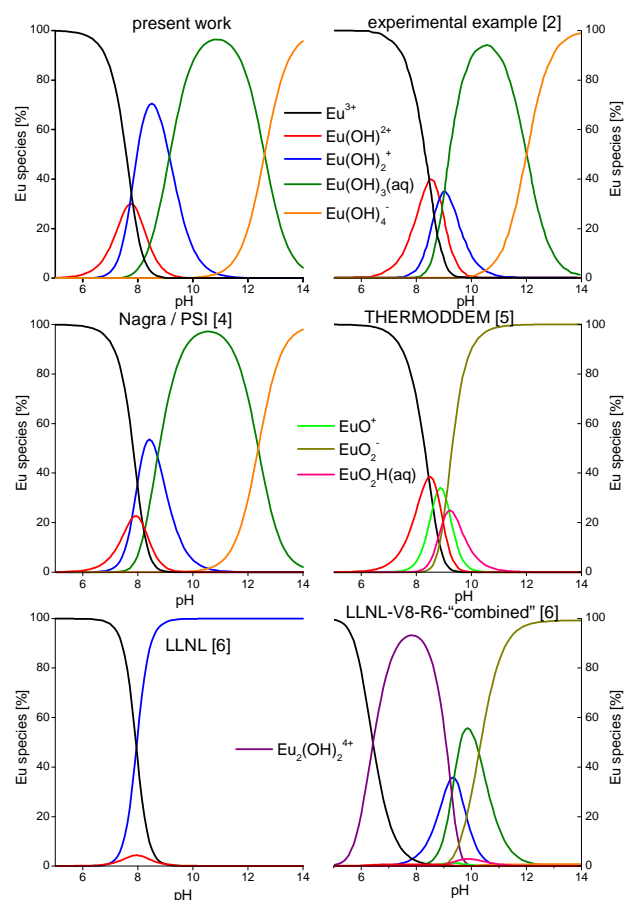


Fig. 1: Eu speciation calculation according to the example from [2] (1 mg/L Eu^{3+} in 0.1 M NaClO_4) and comparing calculations using other databases [4–6].

For most of these databases, the calculation results differ strongly from the experimentally determined chemical speciation of Eu, as they either contain data for too few (LLNL) or too many chemical species (LLNL-V8-R6-“combined”). Species like EuO^+ , EuO_2^- or $\text{EuO}_2\text{H}(\text{aq})$ (as in [5,6]) are not to be found in aqueous solutions where Eu as well as trivalent lanthanides and actinides form hydroxo complexes ($\text{Eu}(\text{OH})_x^{3-x}$). Also the existence of the dimer $\text{Eu}_2(\text{OH})_2^{4+}$ is questionable because of the still missing spectroscopic evidence [7–9]. Even if a dimer is formed, it might not become the dominant species. The speciation calculations with Nagra/PSI data (Fig. 1) fit best to the experimental findings, as our new reviewed

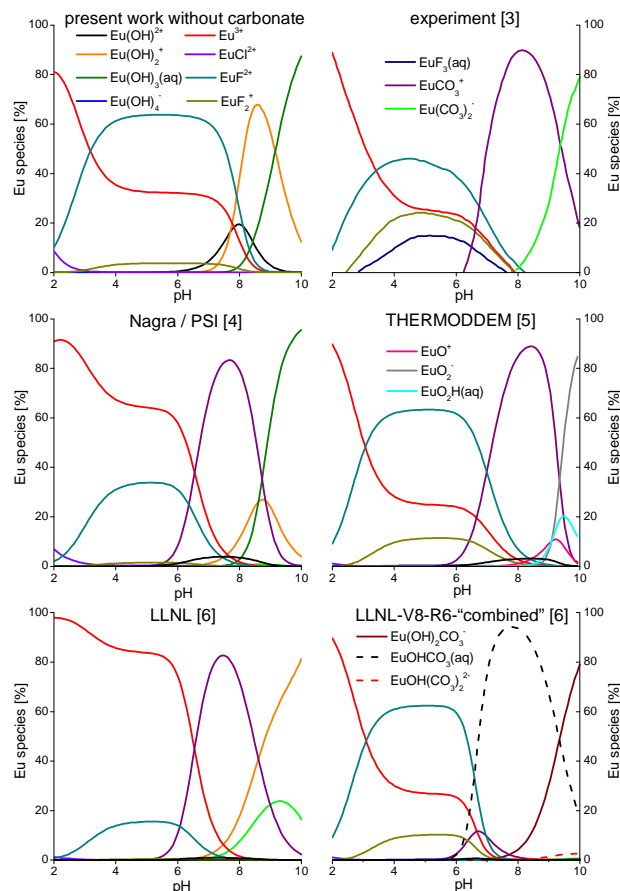


Fig. 2: Eu speciation calculation according to the example from [3] (10^{-7} M Eu^{3+} with 2×10^{-4} M NaCl , 10^{-4} M NaF and 10^{-4} M Na_2CO_3) and comparing calculations using other databases [4–6].

data do. Also the results of the calculations including carbonate differ a lot due to different sets of carbonate complexes (Fig. 2). Therefore, the evaluation of the carbonate data is now mandatory.

CONCLUSIONS. The different results for the europium speciation calculations when using different thermodynamic databases illustrate the need of a critical review of the existent data in literature. This would improve chemical process control of the extraction and processing of important resources like rare earth elements.

ACKNOWLEDGEMENTS. The authors wish to thank A. Barkleit, A. Heller, N. Jordan, C. Joseph, J. Kretzschmar, C. Richter, J. Schott and M. Stockmann for their contributions to the project.

- [1] Brendler, V., Bok, F. (2014) this report, p. 46.
- [2] Planque, G. et al. (2003) *Anal. Chim. Acta*, **478**, 11–22.
- [3] Wood, S. A. (1990) *Chem. Geol.* **82**, 159–186.
- [4] Nagra / PSI (<http://les.web.psi.ch/TDBbook>, as of 2013-12-05).
- [5] THERMODDEM (<http://thermoddem.brgm.fr>, as of 2013-12-05).
- [6] Geochemist’s Workbench® (<http://www.gwb.com/thermo.php>, as of 2013-12-05).
- [7] Bernkopf, M.F. (1984), Ph. D. thesis, TU München.
- [8] Luo, Q. H. et al. (1985) *Chem. J. Chin. Univ.-Chin.*, **6**, 201–205.
- [9] Rard, J. A. (1987) Update of the europium data base, October, 1987: LLNL Internal Memo.

Thermodynamic reference database THEREDA: 5. Test calculation cases of uranium(IV/VI) in the oceanic salt system including carbonates/CO₂

A. Richter, F. Bok

The cooperative project THEREDA establishes a consistent and quality assured database for all safety relevant elements, temperature and pressure ranges, with its focus on saline systems. Data access is possible via commonly available internet browsers under the address <http://www.thereda.de>. Beginning with first data releases in 2011 [1], soon the first ready-to-use Pitzer data set including tetra- and hexavalent uranium data for the system of oceanic salts will be available. Four common geochemical codes (ChemApp, EQ3/6, Geochemist's Workbench, PHREEQC) are addressed.

The NEA Thermodynamic Database (TDB) [2,3] is the major source for thermodynamic data of the aqueous and solid uranium species. Additionally, recently published paper and partially unpublished works from the research group of Neck, Altmaier and co-workers (KIT-INE) are considered. Primarily their work (i.a. [4]) is also the source of the Pitzer ion interaction parameters for the system of oceanic salts containing the elements Na, K, Mg, Ca, Cl, S, C. The THEREDA data release included additional thermodynamic data of solid secondary phases formed in the waste material which were excluded by [2,3] as a result of very stringent quality demands.

URANIUM(IV). According to the experimental study of Rai et al. [5], the solubility of amorphous U(OH)₄ was modeled depending on the bicarbonate concentration using the THEREDA and the Yucca Mountain Pitzer File (YPF) [6] databases (see Fig. 1). While the results of the calculation with the database THEREDA reproduce the experimental values acceptably, it is not possible to model the measured values using the YPF database. However, this is not surprising because oxidizing conditions were presumed at the compilation of this YPF database for modeling in the context of Yucca Mountain. Nevertheless, this serves as an example how misleading results can be by using easily accessible but inappropriate databases. Due to scarcity of data combined with complex systems to be modeled this phenomenon can be observed rather often.

URANIUM(VI). For the hexavalent uranium data, the experimental work of Sandino et al. [7] were chosen as a reference for measured values of the solubility of becquerelite (Ca(UO₂)₆O₄(OH)₆·8H₂O) in high saline (1 m CaCl₂) solution as a function of pH. Again, the scenario was modeled using THEREDA and the Yucca Mountain Pitzer File (YPF) [6] (see Fig. 2). The results of the calculations show that with both databases the measured values can be reproduced comparably well. The differences between the two versions of the YPF database are a result of the changes within the thermodynamic data and the interaction parameters of the matrix elements. The uranium data are identical within those two release versions.

OUTLOOK. The date for the official release is planned to be within the first quarter of 2014. Future THEREDA release of phosphate data will trigger an upgrade of the uranium data release which then will include the uranium(IV/VI)-phosphate interactions, including phases such

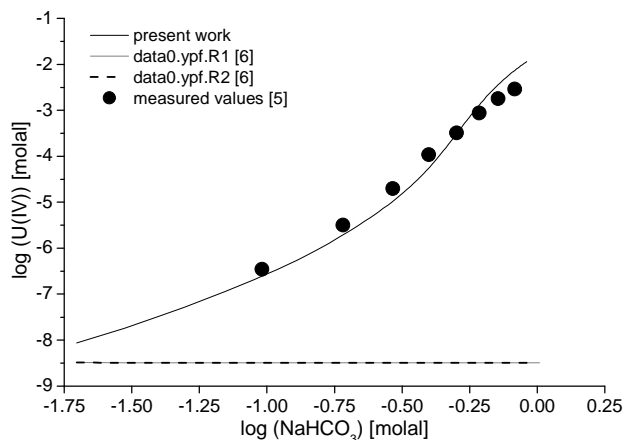


Fig. 1: Solubility of U(OH)₄(am) in up to 1.0 m NaHCO₃ solution, lines: calculated solubility using different Pitzer databases [6], dots: measured values from literature [5].

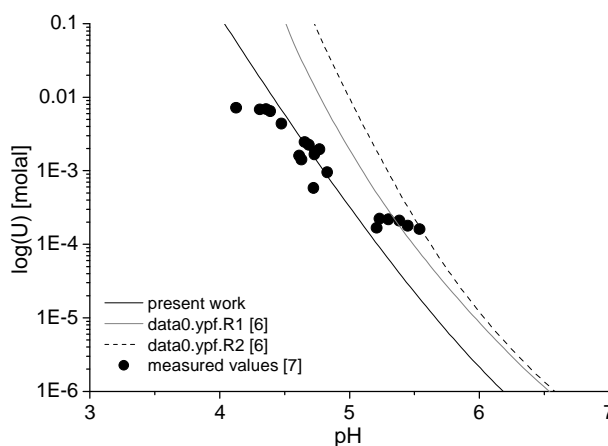


Fig. 2: Solubility of becquerelite in 1 m CaCl₂ solution, lines: calculated solubility using different Pitzer databases [6], dots: measured values from literature [7].

as Ningoyite CaU(PO₄)₂·2H₂O(cr), Chernikovite UO₂(HPO₄)·4H₂O(cr), and Saleeite Mg(UO₂)₂(PO₄)₂(cr).

ACKNOWLEDGEMENTS. Financial support of project stage 2 by the Federal Office for Radiation Protection (BfS) is gratefully acknowledged. The authors thank all partners from the THEREDA joint project.

- [1] Richter, A. et al. (2012) *Report HZDR-013*, p. 55.
- [2] Grenthe, I. et al. (1993) *Chemical Thermodynamics Vol. 1*, Elsevier, Amsterdam.
- [3] Guillaumont, R. et al. (2003) *Chemical Thermodynamics Vol. 5*, Elsevier, Amsterdam.
- [4] Neck, V. et al. (2001) *Report FZK-INE 001/01*.
- [5] Rai, D. et al. (1995) *Mat. Res. Soc. Symp. Proc.*, **35**, 1143–1150.
- [6] Yucca Mountain Pitzer File Version 1/2 delivered with the EQ3/6 software package (<https://missions.llnl.gov/energy/technologies/geochemistry>)
- [7] Sandino, M. et al. (1994) *Radiochim. Acta*, **66/67**, 37–43.

Two new radioactivity-scanners for 1D transport studies (LHS and 1DDAS)

T. Leipold, J. Hauser, K. Franke, J. Lippmann-Pipke

The investigation of transport processes in environmental or technical systems requires suitable detection apparatuses for analyte tracking and process monitoring. The Reactive Transport Division applies radio-tracers that enable excellent accessibility to in situ investigations of isolated processes in complex environments. For many years, we have focused on time resolved process observations in batch systems [1] and 3D-spatio-temporal transport visualizations by means of the GeoPET-method [2]. Here, we report about two new, own designed, built and implemented column scanners – a linear hub scanner (LHS) and a 1D detector array scanner (1DDAS) (Fig. 1) – that close a long-lasting analytical gap.

The LHS (Fig. 1, left) is a sequential detection system for radioactivity distributions within vertical columns (Tab. 1). During a scan, a movable, lead shielded 2x2" NaI(Tl) detector (Gabi, Raytest, Germany) can operate in continuous, discrete or transient mode. The sensitivity of the scanner is adjustable by scan-speed (minimal movement of 0.01 mm/s, precision of 0.01 mm), dwell time and collimator size. Figure 2 shows scan results of a model system with an 8 mm field of view (FOV). The static model system consists of three Cs-137 and two Co-60 point sources of different radioactive activity. The setup allows the differentiation of e.g. these two radionuclides. The activity to signal ratio behaves linearly in the activity range of the used sources.

The 1DDAS (Fig. 1, right) allows simultaneous measurement of the radionuclide distribution within vertical columns (Tab. 1). This scanner is equipped with up to 32 CsI(Tl) detectors (First-Sensor, Germany). Each detector has a size of 100 mm × 8 mm and a dose rate sensitivity for Cs-137 of 900 cpm/(μ Sv/h). The 1DDAS has a modular design. Each detector module contains four detectors and can be arranged according to the experimental needs. The standard setup consists of two opposing scan arrays composed of four vertically stacked modules. This setup offers the best spatial resolution (10 mm). For adjustment to different column diameters (up to 60 mm), the scan arrays are movable at the x-axis. The detectors are shielded and collimated by 50 mm lead. The maximal height of the scanner of 64 cm can be achieved by stacking all detector modules in one array.

Both scanners are equipped with an automatic control and data collecting system. The control software and the hardware interfaces were realized with National Instruments components.

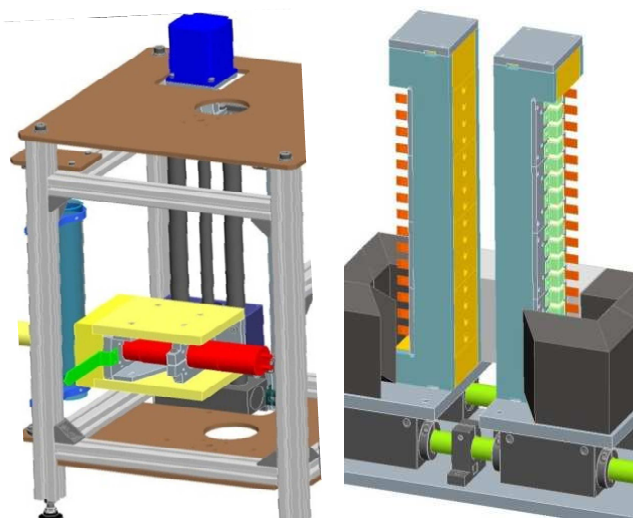


Fig. 1: LHS (left) and 1DDAS (right).

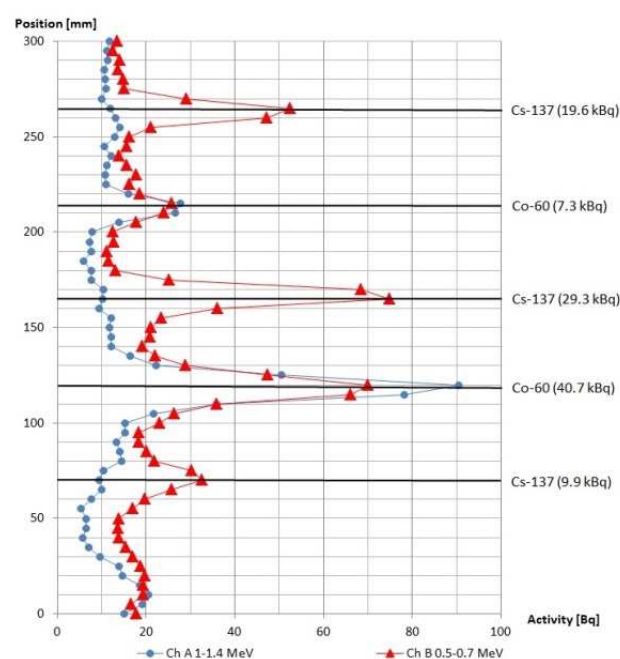


Fig. 2: LHS measurement of 5 radioactive point sources.

Tab. 1: Possible column dimensions.

Column	1DDAS	LHS
height (mm)	10–640	10–350
diameter (mm)	0–60	0–80

[1] Lippold, H. et al. (2012) *Appl. Geochem.* **27**, 250–256.

[2] Kulenkampff, J. et al. (2011) ABC-Salt II Workshop, November 07–08, Karlsruhe, Germany.

SCIENTIFIC CONTRIBUTIONS (PART III)

**NUCLEAR REACTOR
SAFETY & TRANSMUTATION**

The trigonal-geometry diffusion model of the reactor dynamics code DYN3D

S. Duerigen

DYN3D is a three-dimensional nodal reactor dynamics code for steady-state and transient analyses of light-water reactors with square and hexagonal fuel assembly geometries as well as of innovative reactor concepts, which is undergoing continuous development. In this article, the trigonal-geometry DYN3D diffusion model is verified by means of the VVER-1000 benchmark AER-FCM-101.

Recently, the DYN3D code has been extended by multi-group diffusion and SP₃ nodal solvers for reactor cores with hexagonal fuel assembly geometry on trigonal basis [1,2]. The obvious advantage in developing nodal methods in trigonal geometries is the capability of mesh refinement, as a hexagon cannot be subdivided into hexagons of smaller size. A further field of application is the modeling of asymmetric hexagonal fuel assemblies.

BENCHMARK. The three-dimensional diffusion AER-FCM-101 benchmark provided by Schulz [3] models a VVER-1000 in steady state. There are seven material compositions comprising four enrichments, burnable absorber, control rods, and reflector. Figures 1 and 2 show the axial and radial benchmark core configuration. Using zero-current outer boundary conditions, the effective multiplication factor k_{eff} and the two- and three-dimensional power distributions normalized to a core power density of unity are calculated in a 30° symmetry sector over a grid of 18 fuel assemblies with 10 axial layers plus radial and axial reflectors. A CRONOS [4] extrapolated finite-element solution of second order is used as reference [5].

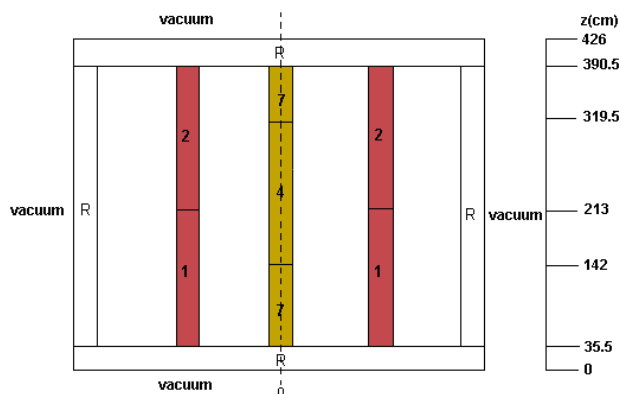


Fig. 1: Axial benchmark core configuration.

RESULTS. In Tab. 1, the multiplication factors k_{eff} , the difference Δk_{eff} and the arithmetic mean absolute difference between the DYN3D three-dimensional power distributions and the CRONOS reference values are listed. Trigonal refinements from 6 to 1536 radial nodes per fuel assembly are used. In Fig. 2, the absolute differences in the axially averaged power distributions are compared. Both multiplication factors and power distributions converge well to the finite-element reference solution with increasing trigonal mesh refinement attaining a precision of only 3 pcm in k_{eff} and 0.4% in the average power distribution.

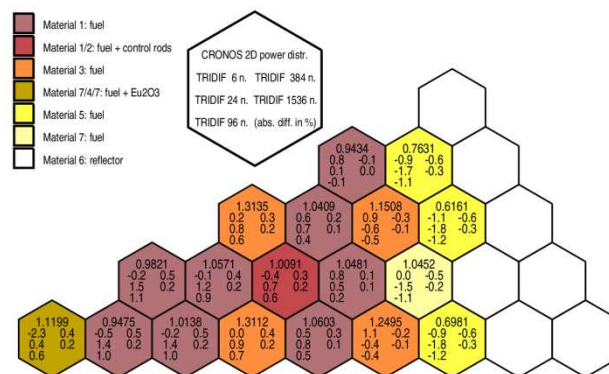


Fig. 2: Radial benchmark core configuration. Axially averaged CRONOS reference power distribution and absolute differences in % determined by DYN3D-TRIDIF using triangular subdivisions from 6 to 1536 nodes.

Tab. 1: Multiplication factors and average absolute 3D power differences of DYN3D-TRIDIF in comparison to CRONOS reference solution.

Method	No. of trig. per fuel ass.	k_{eff}^*	Δk_{eff} (pcm)	Avg. 3D power diff (%)
DYN3D-TRIDIF	6	1.049882	36	0.9
	24	1.049291	-23	1.0
	96	1.049330	-20	0.8
	384	1.049433	-9	0.5
	1536	1.049494	-3	0.4
CRONOS (ref.)		1.049526		

*: $\Delta k_{eff} = (k_{eff_DYN3D} - k_{eff_CRONOS}) \times 10^5$

CONCLUSIONS. In this article, the diffusion model DYN3D-TRIDIF based on trigonal geometries are tested by means of the AER-FCM-101 benchmark. The DYN3D results agree well with the CRONOS finite-element reference solution and spatially converge towards the reference with increasing mesh refinement. Besides the gain in accuracy, however, also the computational effort has to be taken into consideration. It appears that three-dimensional core calculations in very fine nodal resolution are unpractical already in steady state. However, in case of high accuracy required, it is an available option. In practice, a fine resolution might be of interest for a certain core region only, e.g., the central assembly or an assembly with inserted control rods. For such cases, a local refinement option would be beneficial. This is subject to future development.

ACKNOWLEDGMENTS. This work was funded by the German Federal Ministry of Economics and Technology (project no. 1501358).

[1] Duerigen, S. et al. (2013) *Kerntechnik*, **78/4**, 310–318.
 [2] Duerigen, S. (2013), *Report HZDR-035*. (PhD thesis: <http://digbib.ubka.uni-karlsruhe.de/volltexte/1000034870>).
 [3] Schulz, G. (1996) in: *Proceedings of the sixth Symposium of AER on VVER Reactor Physics and Reactor Safety*.
 [4] Lautard, J. J. et al. (1990), *Report IAEA-TECDOC-678*.
 [5] Kolev, N. P. et al. (1999), *AER Benchmark Book* (<http://aerbench.kfki.hu/aerbench/FCM101.doc>).

New coupling approach DYN3D-TRANSURANUS shows limitations of simplified fuel behavior modeling already at low burn-up

L. Holt,¹ U. Rohde

¹Long term visiting scientist at the European Commission, JRC-ITU, Karlsruhe, Germany.

To achieve a more efficient use of uranium resources, the discharge burn-up of nuclear fuels has been gradually increased over the last few decades. This can have an important potential effect on the fuel behavior during design basis accidents (DBA) [1,2]. Hence, it is necessary to model the fuel behavior more detailed, i.e. fission gas release or development of high burn-up structure (HBS) [3]. However, almost all reactor dynamics codes, thermal hydraulics system codes and sub-channel codes include fuel behavior models which treat these complex phenomena in a simplified and often conservative manner. Thus, for the reactor dynamics code DYN3D, a coupling to the European fuel performance code TRANSURANUS [4] was developed. The first results of DYN3D-TRANSURANUS confirm the need of extension of multi-physics couplings to fuel performance codes, at reasonable computational costs.

DEVELOPMENT OF THE CODE SYSTEM DYN3D-TRANSURANUS. In the coupled code system, the simpler fuel behavior model implemented in DYN3D is replaced by the well validated fuel performance code TRANSURANUS [4] maintained by JRC-ITU Karlsruhe. DYN3D provides the time-dependent rod power and thermal hydraulics conditions to TRANSURANUS, which in turn transfers parameters like fuel temperature and cladding temperature back to DYN3D (Fig. 1). In the frame of this development, it was decided to develop a so-called general TRANSURANUS coupling interface and to implement modifications in TRANSURANUS that can be generally used for future code couplings, i.e. DYN3D should be easily replaceable by any other code in the coupled system. Thence, this development can be used for several fuel compositions, for reactor conditions from normal operation to design basis accidents and for time scales from milliseconds to years [5,6].

DESCRIPTION OF THE SIMULATED SCENARIO. The reactivity initiated accident (RIA) is chosen as design basis accident (DBA) for the presentation of the benefit of the new best estimate coupling approach. This kind of transient can occur due to a control rod ejection in a pressurized water reactor (PWR). Within a short time period, a high amount of energy is injected in the fuel rod. The

resulting sharp increase of the fuel temperature can cause transient fission gas release and mechanical loading on the cladding due to pellet cladding mechanical interaction or cladding ballooning [2]. Finally, these phenomena can lead to a burst of the fuel rod. The reactor must be constructed to handle the consequences of the accident without environmental impact.

HIGHLIGHTS OF THE RESULTS. A single failure was assumed for a fully inserted control rod with an ejection time of 0.1 s. DYN3D-TRANSURANUS systematically calculates higher maximum values for the node centerline fuel temperature (max. diff. of 181 K) and node fuel enthalpy (max. diff. of 46 J/g) compared to DYN3D standalone [5,6]. Large differences can be already seen for low burn-up fuel. The differences can be explained by a greater degree of detail in fuel behavior modeling in TRANSURANUS [6]. In summary, the DYN3D standard fuel behavior model has to be used with care keeping in mind that the results might be not conservative.

OUTLOOK FOR DYN3D-TRANSURANUS. The new coupled code system DYN3D-TRANSURANUS opens several options for the future:

- Application of DYN3D-TRANSURANUS to other safety relevant transients, i.e. boron dilution transients.
- Extension of DYN3D-TRANSURANUS to burn-up cycle calculations as well as to a code system for simulating a whole nuclear power (including a thermal hydraulics system code).
- Introduction of the new code system to interested DYN3D users (more accurate safety analysis for nuclear power plants in Europe).
- Providing the general TRANSURANUS coupling interface for other planned couplings with the fuel performance code TRANSURANUS.

ACKNOWLEDGEMENTS. The authors would like to thank Dr. A. Schubert, Dr. P. van Uffelen and J. van de Laar from JRC-ITU Karlsruhe, Dr. M. Seidl from E.ON Kernkraft GmbH as well as Dr. S. Baier, A. Gommlich and Dr. S. Kliem from Helmholtz-Zentrum Dresden-Rossendorf for the technical support, fruitful discussions and comments. The supervision of the PhD thesis by Prof. Dr. R. Macián-Juan at the Technical University Munich is acknowledged. The project is funded by E.ON Kernkraft GmbH within the knowledge preservation program in the German nuclear safety research.

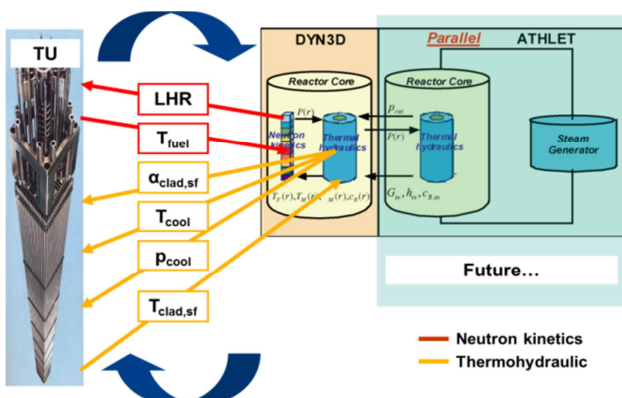


Fig. 1: Data transfer between DYN3D and TRANSURANUS (TU).

[1] RIA Fuel Codes Benchmark (2013), OECD/NEA (including calculations performed by Holt, L.).
 [2] Nuclear Fuel Behaviour Under Reactivity-initiated Accident (RIA) Conditions (2010), OECD/NEA.
 [3] Holt, L. et al. (2014) *J. Nucl. Mat.*, submitted.
 [4] Lassmann, K. (1992) *J. Nucl. Mat.* **188**, 295–302.
 [5] Holt, L. et al. (2013) in: *Conference Proceedings, 10th International Conference on WWR Fuel, Sandanski, Bulgaria.*
 [6] Holt, L. et al. (2014) *Ann. Nucl. Energy*, special volume on LWR Multi-Physics, in preparation.

Development of a transport solver for DYN3D

D. Litskevich, B. Merk

The main objective of this study is to develop and verify new transport solver for DYN3D on the base of current coupling collision probability method with orthonormal flux expansion. Developed solver has been tested for the fixed source problem as well as for eigenvalue problem. Results of calculations performed with developed solver demonstrate good agreement with results of Monte-Carlo and HELIOS calculations.

The last version of the DYN3D code [1] can be used for investigations of transients in light water reactors cores with hexagonal or quadratic fuel assemblies. The DYN3D code is based on the nodal expansion method. It applies for the calculations fuel assembly wise homogenized cross-sections and determines fluxes homogenized for each node in the core. But in many cases, a good knowledge of power and temperature distributions on nodal level is not enough for safety calculations. In most cases, the ability to predict accurately the local pin powers in nuclear reactors is necessary. In the work [2], a new methodology for pin-power calculations in chosen nodes has been proposed. The main idea is to determine the pin wise power distribution inside fuel assemblies applying a transport solver using unstructured mesh with boundary conditions extracted from the 3D full core nodal diffusion solution. In the work, advanced method for solution of transport equation based on the current coupling collision probability method with orthonormal flux expansion was proposed and tested for the single cell [2]. In the present work, the proposed transport methodology is extended from the level of single cell to full assembly level. The results of the calculations demonstrate a good agreement with the results of Monte-Carlo calculations as well as with the results of HELIOS 1.11 [3] calculations.

ONE GROUP CALCULATIONS. The flat flux approximation is used for the traditional CCCP method. Therefore, subdivisions of each zone are needed [4] for an accurate result. This leads to an increasing in calculation time. In order to bypass this problem, an advanced approach based on non-flat flux approximation has been suggested. According to this approach, the nonuniformity of the flux distribution inside zones can be described with the help of orthonormal functions. The method helps to reduce the otherwise required subdivision of zones and thus decreases the time of calculations. In order to verify the developed solver, calculations of a test assembly consisting of hexagonal cells in one energy group have been performed.

The results of the calculations are compared with the results obtained by the Monte Carlo code MCU. A cartogram

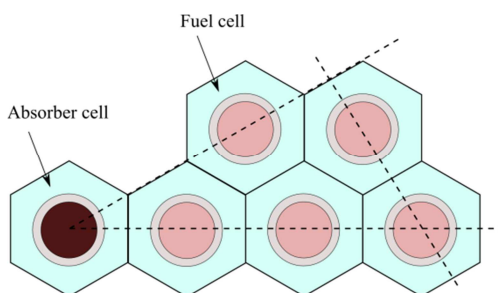


Fig. 1: Cartogram of the test mini assembly.

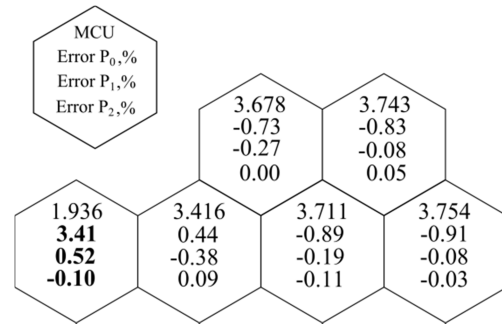


Fig. 2: Results of the calculations for the test mini assembly and comparison with MCU (flux averaged on cell level).

gram of the test mini assembly is presented in Fig. 1. As it can be seen from the Fig. 2, the maximal difference for flat flux approximation (P₀) is 3.41% for average flux in the absorber cell. The error decreases with increasing order of polynomials used for the flux expansion in the calculation regions of the cells. For the P₂-approximation, the maximal absolute error decreases to 0.11% for the average flux in the cells.

MULTIGROUP CALCULATIONS. In order to verify the developed transport solver for the case of several energy groups, the test mini assembly consisting of the strong absorber and the fuel cells has been proposed. The geometry of assembly is the identical to the geometry used for the one group calculations (see Fig. 1). In this study, we used for the calculations HELIOS. The results of the calculation of the normalized fission reaction rates and the comparison of them with the HELIOS reference solution are presented in Fig. 3.

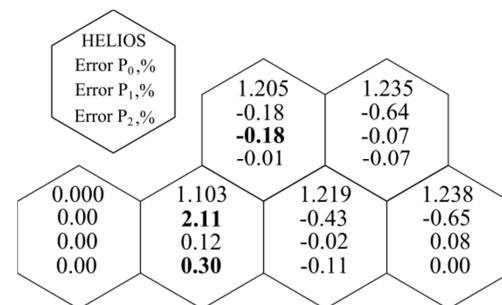


Fig. 3: Results of the multigroup calculations.

As it can be seen from the Fig. 3, the results obtained by the HELIOS code agree quite well with the results obtained by the calculations with the developed transport solver.

[1] Grundmann, U., et al. (2000) *Proc. PHYSOR 2000*, Pittsburgh, U.S.A.
 [2] Litskevich, D., et al. (2013) *Proc. of the 44th Annual Meeting on Nuclear Technology*, Berlin, Germany.
 [3] "HELIOS methods" (2008) *Manual, Program HELIOS-1.10*, Studsvik-Scandpower.
 [4] Merk, B., et al. (2008) *Ann. Nuc. Ener.* **35**, 1492–1501.

Uncertainty and sensitivity analysis for a large break accident simulation for a PWR

U. Rohde, Y. Kozmenkov

A statistical uncertainty analysis (UA) approach was applied to Large Break Loss Of Coolant Accident (LB LOCA) analysis for a Pressurized Water Reactor (PWR). The UA approach allows quantifying target parameter uncertainties caused by input and model parameter uncertainties [1]. A method developed by the Gesellschaft für Anlagen- und Reaktorsicherheit (GRS) [2] based on the Wilk's statistical theory [3] was applied. The ATHLET thermo-hydraulic system code was used for the calculations. It was shown, that the peak cladding temperature upper limit during the accident stays well below the safety limit of 1200 °C. The completeness of the list of uncertainty parameters considered in the UA was shown based on sensitivity analysis.

OBJECTIVES AND METHODOLOGY OF UNCERTAINTY ANALYSIS. Generally, reactor safety analyses are based on the traditional conservative deterministic approach. However, the conservative approach does not allow evaluating the accuracy of results and their deviations from the real values. An alternative approach to reactor safety analyses uses best estimate computer codes in combination with quantification of uncertainties in model and plant parameters. Uncertainties in the results of safety analysis calculations are related to the uncertainties in the employed code models as well as to the lack of knowledge on the reactor initial conditions.

In HZDR, an uncertainty analysis for a LB LOCA scenario for a generic German PWR of the KONVOI design was performed [4] using the thermo-hydraulic system code ATHLET and the EXCEL integrated software SUSANA developed by GRS. SUSANA accomplishes the generation of uncertainty parameter vectors, their incorporation into ATHLET input files and the statistical evaluation of the results. The methodology is based on the Wilks' theory on statistical analysis. According to this theory, the number of calculations required to perform a probabilistic estimation of an output parameter with a given coverage/confidence level (e.g., 95%/95%) does not depend on the number of input uncertainty parameters. 93 calculations, corresponding to the second order of the Wilks' formula, have to be done to reach this level of coverage/confidence for one-sided (e.g., upper) statistical tolerance limit. All uncertainty parameters must be statistically independent and are varied simultaneously in the calculations.

RESULTS OF UNCERTAINTY ANALYSIS. The target parameter in the LOCA analysis is the maximum fuel cladding temperature which is reached during the course of the transient. Usually, the maximum occurs during the blow-down phase of the accident, when a huge part of the coolant is lost through the leak. According to safety criteria, this peak cladding temperature (PCT) should not exceed 1200 °C. Figure 1 shows the PCT results for the 93 calculations with statistical variation of the uncertain input parameters. The PCT upper limit value for this peak is 846 °C what is well below the safety limit.

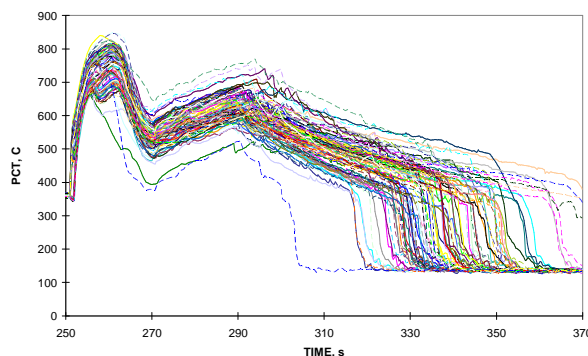


Fig. 1: Behavior of the PCT in the ATHLET calculations.

SELECTION OF UNCERTAINTY PARAMETERS AND SENSITIVITY ANALYSIS.

An important step of the analysis is the selection of uncertainty parameters to be varied. In the first step, 47 uncertainty parameters were selected based on expert's judgment. They are belonging to the following 3 groups:

- parameters of ATHLET thermal-hydraulic models (32 parameters),
- reactor core parameters (8 parameters),
- reactor plant and safety systems parameters (7 parameters).

However, the number of uncertainty parameters should be reduced to limit the tremendous efforts required for the quantification of the model parameters uncertainties based on the analysis of measurement data. On the other hand, it must be ensured that all uncertainty parameters, which have a significant impact on the result of the calculations, are included. This task was solved by means of sensitivity analysis. As a measure for the sensitivity of the result against statistical uncertainty of an input parameter, statistical correlation coefficients, like e.g. the Pearson's rank correlation coefficient, are calculated. The Student's criterion was used to check whether the correlation is statistically relevant, what means, that it shows a confidence level required. Applying this procedure, finally a list of 16 relevant uncertainty parameters was identified. It was found, that the main contributions to the uncertainty of the PCT are given by the core parameters (maximum local heat generation rate, fuel conductivity, width of the gas gap between fuel and cladding) which affect the fuel's stored energy at the beginning of the accident.

ACKNOWLEDGEMENTS. The project was funded by Vereinigung der Großkraftwerksbetreiber (VGB PowerTech) under contract number SA AT 25/11.

-
- [1] Seeberger, G-J. et al. (2011) *From phenomena to acceptance criteria. A statistical LBLOCA analysis*, Jahrestagung Kerntechnik, Berlin.
 - [2] Glaeser, H. (2008) *GRS Method for Uncertainty and Sensitivity Evaluation of Code Results and Applications*, Science and Technology of Nuclear Installations, Article ID 798901.
 - [3] Wilks, S.S. (1941) *Ann. Math. Stat.* **12**, 91–96.
 - [4] Kozmenkov, Y.; Rohde, U. (2013) *Kerntechnik* **78**, 354–361.

Application of the system code ATHLET from nuclear engineering onto solar thermal power plants

A. Hoffmann

The ATHLET (Analysis of THERmal-hydraulics of LEaks and Transients) code originates from nuclear engineering for the investigation of light water reactors [2]. But ATHLET is also capable of treating topics which are not connected to nuclear engineering. The objective is to use the capabilities of ATHLET in the field of solar power plants.

The parabolic trough solar thermal power plants are one promising technology to cover the energy demand in the future. Next level solar thermal power plants are working with the direct steam generation (DSG) process. The working principle of the recirculation-mode (see Fig. 1) is to concentrate the sunlight with parabolic trough collectors onto a straight horizontal receiver tube and to evaporate a part of the feed water directly. Afterwards, water and steam is separated in the water/steam separator and the steam is superheated in two further collectors. This steam can be used to drive a steam turbine and generator for electricity production. The DSG process improves the efficiency and reduces the investment and operating costs compared to a process with heat transfer fluid [1,4]. To predict the behavior of the water/steam flow inside of the absorber pipes, numerical simulation tools are applied. ATHLET is used in the present study to perform post-test calculations.

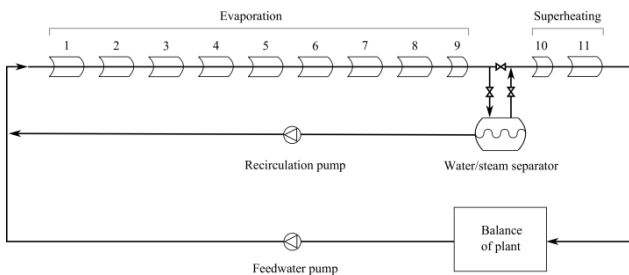


Fig. 1: Simplified scheme of the DISS test facility at Plataforma Solar de Almería, Spain.

MODEL. ATHLET is used to assemble a model of the DISS test facility at Plataforma Solar de Almería [4] (Fig. 1). The receiver tubes have a combined length of 500 m. In between, each receiver tube connection pipes are modelled and the water/steam separator is represented by a vertical pipe. One hour of operation under real conditions at DISS test facility is chosen as test case. This test case provides the boundary conditions for the simulation. The mass flow and the enthalpy are given as boundary conditions at the inlet of the receiver tube 1. After the superheating section, the pressure is given as boundary condition and a mass flow is given at the water/steam separator to represent the recirculation pump. Further necessary boundary conditions are the heat flux into the receiver tube and the ambient temperature.

RESULTS. To assess the results of the ATHLET post-test calculations the mass flow and steam temperature at the outlet of receiver tube 11 are compared to the measurements (Fig. 2,3). The overall mass and energy balance is properly calculated by the ATHLET code for this demonstration test case. Therefore, the ATHLET code

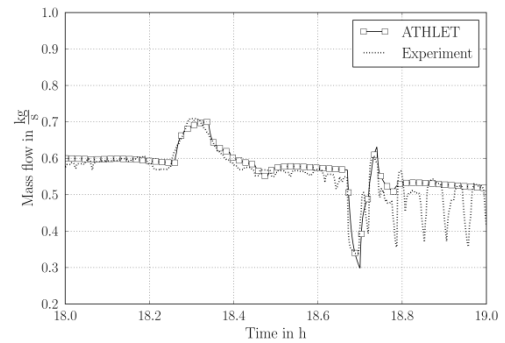


Fig. 2: Mass flow of steam at the outlet of receiver tube 11.

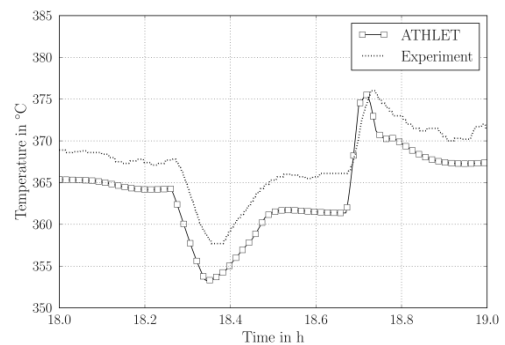


Fig. 3: Steam temperature at the outlet of receiver tube 11.

seems to be able to reliably predict the thermal fluid dynamics of such facilities.

Figure 4 shows the velocities of each phase in the receiver tubes which have not been measured during the experiment and cannot be calculated with the usually applied simulation tools. But ATHLET provides a 6-equation model for the description of the fluid flow and enables their calculation. It has been found that the steam phase precedes the liquid phase with maximal twice the velocity. A more detailed analysis of the slip should investigate the influence of the slip on the heat transfer and the pressure drop.

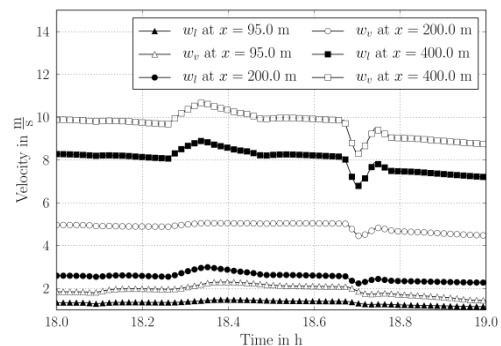


Fig. 4: Steam and liquid velocity at different positions along the two-phase region.

[1] Feldhoff, J. F. et al. (2010) *J. Sol. Energy Eng.* **132**, 041001.
 [2] Lerchl, G. et al. (2012) *ATHLET Mode 3.0 Cycle A - User's Manual*, Gesellschaft für Anlagen- und Reaktorsicherheit (GRS) mbH.
 [3] Zarza, E. et al. (2004) *Energy* **29**, 635–644.
 [4] Zarza, E. et al. (2001) *Proc. Solar Forum 2001*, Washington D.C., U.S.A.

Neutron fluence calculations in the cavity of a VVER-440/213 reactor and of surveillance specimens positions

J. Konheiser, A. Grahn

The reactor pressure vessel (RPV) represents one of the most important safety components in a nuclear power plant. Therefore, a special program exists for monitoring the material conditions of RPVs. Surveillance specimen (SS) programs for RPV materials supply a reliable assessment of RPV residual life-time. They involve accompanying calculations of neutron fluence. This work was performed as part of a Russian-German scientific and technical cooperation.

For the assessment of RPV embrittlement, it is necessary to know the radiation exposure parameters. Those are mainly the neutron- and gamma fluences and spectra in the RPV. Another aspect is the heating of the sample during irradiation. Excessive heating could lead to annealing of defects and to misleading results. The results of fluence and temperature calculations were checked against experiments. Activation measurements were carried out at ex-vessel positions of a VVER-440 reactor for the neutron fluences. They provide the basis for validation of calculated neutron fluences of the surveillance specimen.

CALCULATION. The neutron and gamma fluences were calculated by the Monte Carlo program TRAMO [1] and a three-dimensional synthesis method, based on the 2D discrete ordinates code DORT [2].

Full geometrical and material information were provided by the Russian colleagues. A 60° sector model of the reactor was used for the calculation. The necessary source data were calculated based on the power data of the cycle of unit. The source distribution was given pin-wise in the outer fuel assembly rows.

The stationary temperature distribution in the SS was calculated based on simplified geometries in order to make the problem amenable to analytic treatment. Two cases were defined which correspond to the upper and lower limits of the expected temperature range. The lower limit is established by a hollow cylinder with a concentrically embedded SS capsule which is cooled around its entire circumference, the upper limit by approximating the SS as an additional heated shell around the core barrel with one dimensional heat conduction in the radial direction. The heat source due to irradiation was estimated to be 0.06 W/g with help of the fluence calculations and is mainly caused by gamma radiation. The heat conduction equation was solved analytically, based on estimated heat transfer coefficients at the channel surface against the coolant flow in the downcomer.

MEASUREMENT. The measurements were carried out by Russian colleagues of SEC-NRS at Unit 3 of Kola NPP over the time span of a whole fuel cycle. Detectors were installed in the heights of the core mid-plane and of the critical weld. Likewise, monitors were at the azimuthal position of 30°, distributed over the height of the cores. As neutron activation dosimeters the isotopes ^{54}Fe and ^{58}Ni were mainly used.

SS capsules are placed in two vertical channels which are welded at different azimuthal positions onto the outer core barrel surface and are distributed over the height of the active zone. The capsules contain melting monitors (277,

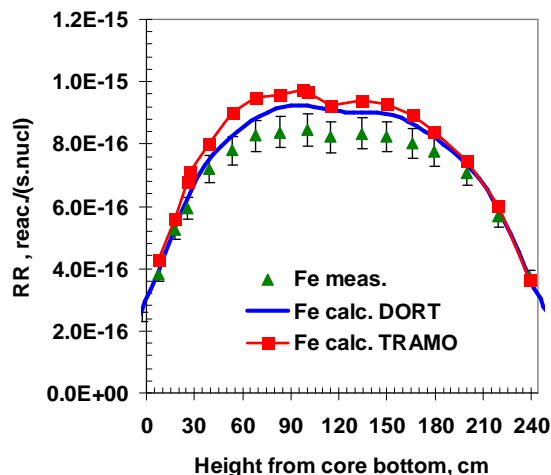


Fig. 1: Reaction rates for the Fe-monitors on the vertical positions.

280, 284, 286, 288 °C) for temperature determination. Additionally, temperature was measured by thermocouples mounted into the two uppermost capsules. The coolant inlet temperature was measured as well.

RESULTS. Figure 1 shows exemplarily reaction rates for the Fe-monitors on the vertical positions. The reaction rates were determined on the basis of calculated neutron spectra and the cross section of $^{54}\text{Fe}(n,p)^{54}\text{Mn}$ reaction. Tendency to large values was calculated for the monitors. The maximum deviation is 15%. The reason is suspected in the source data, since the results are too large in both calculations. A surprising result was that the shielding effect of a baffle rib was seen in the measurement and the Monte Carlo calculation results.

The comparisons between the results of TRAMO and DORT calculations showed very good agreement. The differences between the calculated results were 5% at maximum.

The thermocouple readings were in the range of 263–273 °C, depending on the reactor power. The temperature measurements by melting monitors fell in the same range, although these results were less precise. The inlet coolant temperature was 265 °C, leading to an average overheating of the specimen of about 4 to 5 degrees. The calculated temperatures for the two limiting cases were found to be 270.5 and 286 °C, leading to a calculated overheating of 5.5 degrees for the lower limiting case. Although rather conservative, the calculated upper limit is far below temperatures which would allow for annealing effects of the RPV material.

ACKNOWLEDGEMENTS. This work was supported in part by the bilateral scientific-technical cooperation agreement between Germany and Russia through the project of the Ministry of Economics and Technology of Germany.

[1] Barz, H.-U. et al. (1998) Report FZR-245.

[2] Rhoades, W., and Childs, R., (1991) TORT/DORT: Two-and Three Dimensional Discrete Ordinates Transport, CCC-543.

Neutronic and thermal-hydraulic analysis of High Conversion Th-U233 PWR core

D. Baldova, E. Fridman

This study presents the development of a high conversion Th-U233 fuel cycle that is considered for current generation of Pressurized Water Reactors. The proposed high conversion core model consists of 193 typical 17x17 PWR fuel assemblies. Each fuel assembly is subdivided into two regions designated as seed and blanket (Fig. 1). The central seed region, which has high U233 content, serves as a neutron supplier for the peripheral blanket region. The blanket region, which consists mostly of Th232, acts as a U233 breeder.

This paper presents the results of the neutronic and thermal-hydraulic (T-H) analysis of the high-conversion (HC) Th-U233PWR core. The main goal is to evaluate the operational feasibility of the high conversion Th-U233 core through performing the 3D fully coupled neutronic and thermal-hydraulic analysis. The 3D full core calculations were performed with the DYN3D core [1], employing the two-group cross sections (XS) generated by the code HELIOS [2]. The XS were generated as functions of burn-up, fuel and moderator temperatures, and soluble boron level. The full core analysis was done for different HC PWR core cases varying in the initial seed enrichment, in the average power density level, and in the inlet coolant temperature. All the HC PWR core cases were analyzed by using of the 3-bath fuel management. As an alternative to the conversion ratio, the instant to initial fissile inventory ratio (FIR) was considered. The T-H behavior was analyzed through an evaluation of the limiting T-H parameters including Minimum Departure from Nucleate Boiling Ratio (MDNBR), Fuel Central Line Temperature (T_{CL}), and void fraction. It is required that the maximum T_{CL} should be 200 °C below the melting point of the Th-U oxide, which is 3100 °C. The local heat flux should be lower than critical heat flux by 1.3 which is the MDNBR value typically used in the PWR thermal analysis. The maximum void fraction representing nucleate boiling should not exceed the sub-cooled boiling level.

RESULTS. As shown in Fig. 2, the maximum boron concentration of any of HC Th-U233 PWR cores does not exceed 250 ppm. The fuel cycle length ranged from 300 to 345 Effective Full-Power Days (EFPD), depending on the HC Th-U233 PWR case. The results presented in Tab. 1 suggest that HC Th-U233 core at higher power density levels of 70 W/cc (Case 1) and 65 W/cc (Case 2)

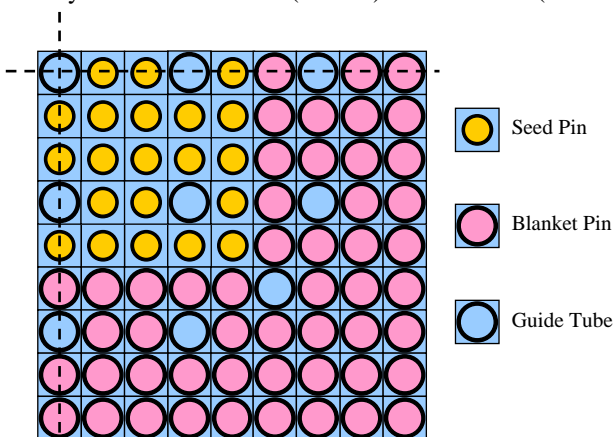


Fig. 1: 1/4th of the 17x17 SB fuel assembly.

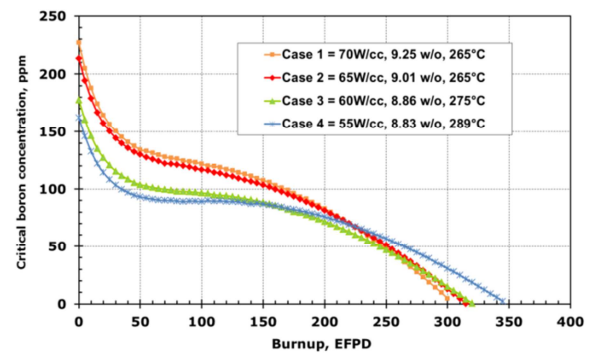


Fig. 2: Critical boron concentration (where Case No. = power density, initial seed enrichment, inlet coolant temperature).

Tab. 1: Results of 3D full core analysis.

Case No.	FIR at discharged	Min DNBR	Max void fraction (%)	Max T_{CL} (°C)
<i>Beginning of Cycle</i>				
1		1.46	0.6	2110
2		1.54	0.3	1957
3		1.52	0.7	1870
4		1.51	8.0	1774
<i>End of Cycle</i>				
1	0.98	1.66	0.1	1512
2	0.99	1.82	0.0	1432
3	1.00	1.89	0.0	1361
4	1.01	1.89	0.3	1284

comply with the safety limits – both could be potentially operated; however, the FIR in both cases is lower than unity. The HC Th-U233 core operated at power density of 60 W/cc and with the higher inlet coolant temperature of 275 °C meets both the safety requirements and the self-sustainability (FIR equal to unity) requirements. The last Case 4 having the lowest power density could be potentially operated, too; however, it can be seen that the reduction in the power density from 104 to 60 W/cc is sufficient to ensure the safety operation and to achieve sustainable fuel cycle.

[1] Grundmann, U. et al. (2000) *Proc. PHYSOR 2000*, Pittsburgh, U.S.A..

[2] Scandpower, S. (2008) “*HELIOS Methods*” (version 1.10).

Coolant mixing experiments at the ROCOM test facility for a main steam line break scenario

S. Kliem, R. Franz¹

¹Institute of Fluid Dynamics, HZDR, Dresden, Germany

Coolant mixing experiments based on a main steam line break scenario have been conducted at the Rosendorf Coolant Mixing Model (ROCOM). The main purpose of these experiments was the clarification of the underlying mixing processes inside the vessel of the facility. From the results, it can be concluded that the ratio of the flow rates between perturbed and non-perturbed loops is the main factor for determining the position of the boundary layer between mixed and non-mixed regions.

ROCOM is a four-loop test facility for the investigation of coolant mixing operated with water at room temperature (Fig. 1).

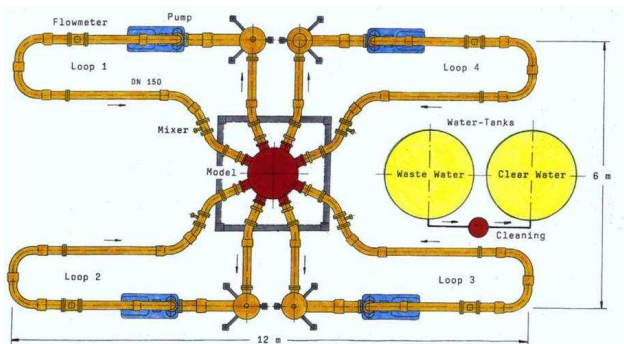


Fig. 1: Sketch of the ROCOM test facility.

The facility models the primary circuit of a German KONVOI-type reactor with all details important for the coolant mixing along the flow path, from the cold-leg nozzles up to the core inlet, at a linear scale of 1:5. Special attention was given to components which significantly influence the velocity field, such as the core barrel with lower core support plate and core simulator, perforated drum in the lower plenum, and inlet and outlet nozzles [1]. The facility is operated with de-mineralized water at room temperature. Salt water is used to alter the local electrical conductivity of the fluid in order to label a specific volume of water and thus simulate an overcooled slug of coolant. The distribution of this tracer in the test facility is measured by special own developed wire-mesh electrical conductivity sensors which allow measurements of the transient tracer concentration with a high spatial and time resolution.

A series of five different experiments on coolant mixing at this test facility have been conducted within an OECD sponsored research project [2].

OBJECTIVE AND BOUNDARY CONDITIONS. In contrast to quasi-stationary tests performed earlier [3], the ROCOM test described here was performed under transient conditions. The main objective of this test was the assessment of the influence of changing mass flow rate in the non-affected loops on the position of the transition region between the sectors and a more or less homogeneous temperature distribution. The corresponding data contributes to the understanding of the mixing processes inside the reactor pressure vessel and to the safety assessment of the reactor behavior in related hypothetical accidents.

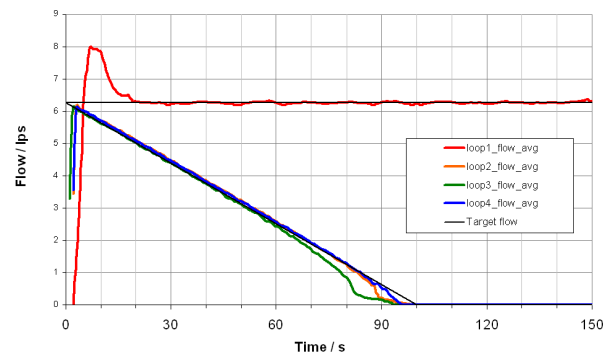


Fig. 2: Flow rates in the different loops over time.

Figure 2 shows the flow rates in the four loops of the test facility (loop 1 is the overcooled loop).

RESULTS. Figures 3 and 4 show the temperature distribution in the early phase and at the end of the experiment. A shifting of the position can be observed only after a considerable reduction of the flow rate in the unperturbed loops. It can be concluded that the ratio of the flow rates (perturbed flow and sum of the unperturbed flows from the three other loops) is the determining factor for the position of this transition region.

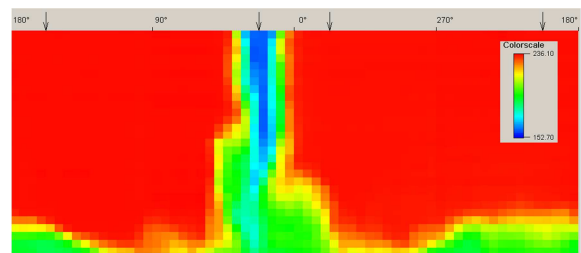


Fig. 3: Measured tracer distribution in the downcomer at the begin of the experiment (temperature scale in °C).

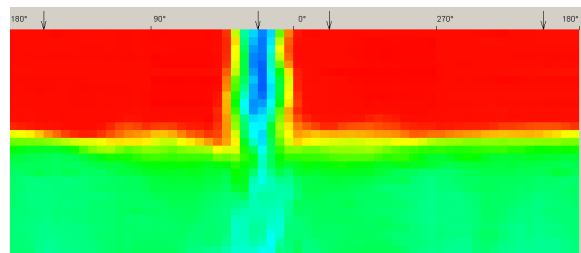


Fig. 4: Measured tracer distribution in the downcomer at the end of the experiment.

The determination of the influence of the flow rates on the transition region contributes to the reduction of the uncertainty in assessing the re-criticality risk during hypothetical overcooling transients in pressurized water reactors.

ACKNOWLEDGEMENTS. The ROCOM experiment was conducted within the OECD sponsored PKL2 project. The boundary conditions were derived from a PKL-experiment conducted by AREVA Germany in Erlangen.

[1] Kliem, S. et al. (2008) *Nucl. Eng. Design* **238**, 566–576.
 [2] Agnoux, C. et al. (2013) *OECD PKL2 Final Report*.
 [3] Kliem, S. et al. (2013) *HZDR Report-030*, p. 69.

Conceptual design of a pressure tube light water reactor with variable moderator control (PTVM LWR)

R. Rachamin, E. Fridman, A. Galperin¹

¹Department of Nuclear Engineering, Ben-Gurion University of the Negev, Beer Sheva, Israel

An innovative light water reactor constructed as a multitude of modular, horizontal fuel channels has been proposed. The basic novelty of the proposed design is an implementation of the “breed & burn” mode of operation by a dynamic variation of the moderator content in the core. The feasibility of such a design was evaluated by analysing a full core model using the BGCORE Monte-Carlo based depletion code. It has been shown that the proposed design has a potential to increase the fuel utilization, to attain negative reactivity coefficients and to reduce the excess core reactivity during the power operation.

INTRODUCTION AND REACTOR DESIGN DESCRIPTION

This study presents the development of an innovative nuclear reactor based on an idea of “breed & burn” mode of operation [1]. The “breed & burn” mode holds a great promise of improving the fuel utilization. The principles and concepts of fast “breed & burn” reactors were extensively investigated and reported through the years [2,3]. Unlike these reactors, the proposed novel design is a thermal light water reactor in which the “breed & burn” mode of operation is implemented by a dynamic variation of the moderator content in the core. In order to achieve a practical reactor design build on proven technology, the novel design is based on the ACR-1000 core layout [4]. There are, however, several major features which differ from the ACR-1000 design. First, the inter-fuel channels spacing, surrounded by the calandria tank, contains a low pressure gas instead of heavy water moderator. Second, the fuel channel design features an additional/external tube (designated as moderator tube) connected to a separate moderator management system. The modified fuel channel assembly is shown schematically in Fig. 1. The moderator management system is designed to vary the moderator tube content from “dry” (gas) to “flooded” (light water filled). The moderator variation results in a neutron spectral shift, which allows the implementation of the “breed & burn” mode of operation. The “breed & burn” mode is implemented by keeping the moderator tube empty (“dry” filled with gas) during the breed part of the fuel depletion and subsequently introducing the moderator by “flooding” the moderator tube for the “burn” part. The fuel channel assembly is designed to contain 12 fuel bundles and produce average power of 6.129 MWt. The core design consists of 528 novel fuel channel assemblies (3236 MWt) arranged in hexagonal lattice (14 rings). It is assumed that the moderator management system is capable of changing the moderator content of a collection of fuel channel assemblies, e.g. all channels positioned in a single ring of channels. The proposed design is basically Pressure Tube light water reactor with Variable Moderator control (PTVM LWR) [1].

NEUTRONIC ANALYSIS OF THE REACTOR DESIGN

The feasibility of the PTVM LWR design was evaluated primarily from a neutronics point of view by analyzing an all-U based fuel cycle model with 4-batches in-core fuel management scheme and on-power stepwise moderator addition [4]. The core performance was analyzed using

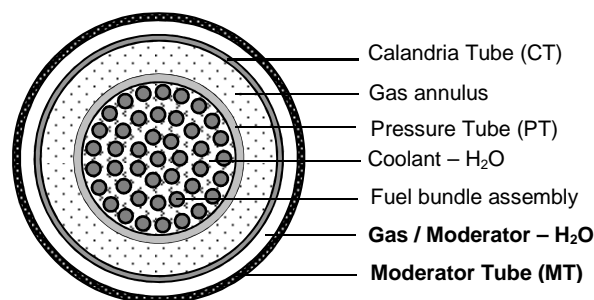


Fig. 1: Schematic view of the PTVM fuel channel assembly design.

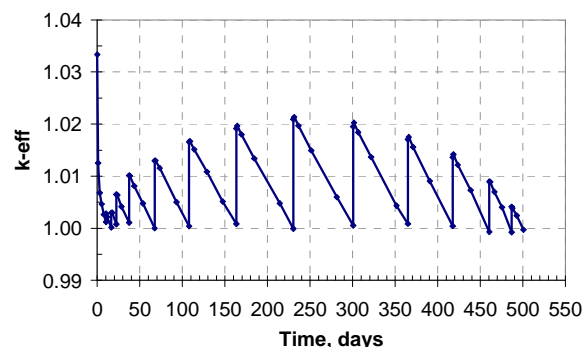


Fig. 2: Core k-eff (equilibrium cycle) as a function of time.

the BGCORE Monte-Carlo based depletion code [5] for a total of 5 reload cycles, in order to achieve a representative equilibrium cycle. The core k-eff of the equilibrium cycle is presented as a function of time in Fig. 2. The k-eff curve reflects the core power production with the on-power stepwise moderator addition. The core power production starts with a dry core (all fuel channel assemblies are in a dry status). At the point where k-eff is about 1.00, the core reactivity is augmented by a series of successive additions of moderator, carried out by flooding a single ring of fuel channel assemblies during the power production. The successive channels flooding are continued “out-in”, i.e. starting with outer ring and inwards, until the whole core is flooded. It should be noted that the maximum excess reactivity of the core is about 2%, excluding the initial burnup at the BOC. The fuel utilization was estimated and found to be 6.08 GWd/T NU. This result clearly indicates that the proposed design has a potential to increase the fuel utilization in comparison with LWR’s of current technology by about 15% and to reduce excess core reactivity during the power operation.

- [1] Rachamin, R. et al. (2013) *Ann. Nucl. Energy* **60**, 248–255.
- [2] Fischer, G.J. et al. (1980) *Report BNL-51391*, BNL, U.S.A.
- [3] Greenspan, E. (2012) *Sustainability* **4**, 2745–2764.
- [4] AECL (2007) *ACR-1000 Technical Summary*, AECL, Canada.
- [5] Fridman, E. et al. (2008) *Proc. PHYSOR 2008*, Switzerland.

- ▣ ARTICLES (PEER-REVIEWED)
- ▣ EXTENDED ABSTRACTS, REPORTS,
CONTRIBUTIONS
- ▣ LECTURES, ORAL PRESENTATIONS
- ▣ POSTERS
- ▣ AWARD
- ▣ DOCTORAL THESES
- ▣ MASTER, DIPLOMA, BACHELOR

ARTICLES (PEER-REVIEWED)

- Barkleit, A.; Acker, M.; Bernhard, G.
Europium(III) complexation with salicylic acid at elevated temperatures
Inorganica Chimica Acta 394, 535–541 (2013).
- Belin, R.C.; Martin, P.M.; Lechelle, J.; Reynaud, M.; Scheinost, A.C.
On the role of cation interactions in the reduction process in plutonium-amercurium mixed oxides
Inorganic Chemistry 52, 2966–2972 (2013).
- Carvajal-Nunez, U.; Prieur, D.; Janssen, A.; Wiss, T.; Cambriani, A.; Vermorel, E.; Scheinost, A.C.; Somers, J.
Characterization of self-damaged (U,Pu)N fuel used in the NIMPHE program
Journal of Nuclear Materials 443, 491–496 (2013).
- Chorro, M.; Kane, G.; Alvarez, L.; Cambedouzou, J.; Paineau, E.; Rossberg, A.; Kociak, M.; Aznar, R.; Pascarelli, S.; Launois, P.; Bantignies, J.L.
1D-confinement of polyiodides inside single-wall carbon nanotubes
Carbon 52, 100–108 (2013).
- Dahou, S.; Hennig, C.; Moisy, P.; Petit, S.; Scheinost, A.C.; Subra, G.; Vidaud, C.; Den Auwer, C.
Short note on the hydrolysis and complexation of neptunium(IV) in HEPES solution
Radiochimica Acta 101, 367–372 (2013).
- Duerigen, S.; Rohde, U.; Bilodid, Y.; Mittag, S.
The reactor dynamics code DYN3D and its trigonal-geometry nodal diffusion model
Kerntechnik 78, 310–318 (2013).
- Dulnee, S.; Banerjee, D.; Merkel, B.; Scheinost, A.C.
Surface complexation and oxidation of Sn^{II} by nano-magnetite
Environmental Science & Technology 47, 12852–12859 (2013).
- Dumas, T.; Charbonnel, M.C.; Charushnikova, I.A.; Conradson, S.D.; Fillaux, C.; Hennig, C.; Moisy, P.; Petit, S.; Scheinost, A.C.; Shuh, D.K.; Tyliszczak, T.; Den Auwer, C.
Multi edge X-ray absorption spectroscopy of thorium, neptunium and plutonium hexacyanoferrate compounds
New Journal of Chemistry 37, 3003–3016 (2013).
- Fridman, E.
Serpent Monte-Carlo code: an advanced tool for Few-group cross section generation
atw - International Journal for Nuclear Power 58, 156–157 (2013).
- Fridman, E.; Duerigen, S.; Bilodid, Y.; Kotlyar, D.; Shwageraus, E.
Axial discontinuity factors for the nodal diffusion analysis of high conversion BWR cores
Annals of Nuclear Energy 62, 129–136 (2013).
- Fridman, E.; Shwageraus, E.
Modeling of SFR cores with Serpent-DYN3D codes sequence
Annals of Nuclear Energy 53, 354–363 (2013).
- Gaona, X.; Wieland, E.; Tits, J.; Scheinost, A.C.; Dähn, R.
Np(V/VI) redox chemistry in cementitious systems: XAFS investigations on the speciation under anoxic and oxidizing conditions
Applied Geochemistry 28, 109–118 (2013).
- Güchel, K.; Rossberg, A.; Müller, K.; Brendler, V.; Bernhard, G.; Foerstendorf, H.
Spectroscopic identification of binary and ternary surface complexes of Np(V) on gibbsite
Environmental Science & Technology 47, 14418–14425 (2013).
- Güchel, K.; Tsushima, S.; Foerstendorf, H.
Structural characterization of the aqueous dimeric uranium(VI) species: (UO₂)₂CO₃(OH)₃⁻
Dalton Transactions 42, 10172–10178 (2013).
- Hennig, C.; Ikeda-Ohno, A.; Kraus, W.; Weiss, S.; Pattison, P.; Emerich, H.; Abdala, P.; Scheinost, A.C.
Crystal structure and solution species of Ce(III) and Ce(IV) formates – From mononuclear to hexanuclear complexes
Inorganic Chemistry 52, 11734–11743 (2013).
- Hennig, C.; Takao, S.; Takao, K.; Weiss, S.; Kraus, W.; Emmerling, F.; Meyer, M.; Scheinost, A.C.
Identification of hexanuclear actinide(IV) carboxylates with thorium, uranium and neptunium by EXAFS spectroscopy
Journal of Physics: Conference Series 430, 012116 (2013).

- Hennig, C.; Weiss, S.; Banerjee, D.; Brendler, E.; Honkimäki, V.; Cuello, G.; Ikeda-Ohno, A.; Scheinost, A.C.; Zänker, H.
Solid-state properties and colloidal stability of thorium(IV)-silica nanoparticles
Geochimica et Cosmochimica Acta 103, 197–212 (2013).
- Höhne, T.; Grahn, A.; Kliem, S.; Rohde, U.; Weiss, F.-P.
Numerical simulation of the insulation material transport in a PWR core under loss of coolant conditions
Nuclear Engineering and Design 258, 241–248 (2013).
- Ikeda-Ohno, A.; Hennig, C.; Weiss, S.; Yaita, T.; Bernhard, G.
Hydrolysis of tetravalent cerium for a simple route to nanocrystalline cerium dioxide: an in situ spectroscopic study of nanocrystal evolution
Chemistry – A European Journal 19, 7348–7360 (2013).
- Insulander-Björk, K.; Mittag, S.; Nabbi, R.; Rineiski, A.; Schitthelm, O.; Vezzoni, B.
Irradiation of a thorium-plutonium rodlet: experiment and benchmark calculations
Progress in Nuclear Energy 66, 73–79 (2013).
- Jordan, N.; Müller, K.; Franzen, C.; Brendler, V.
Temperature impact on the sorption of selenium(VI) onto anatase
Journal of Colloid and Interface Science 390, 170–175 (2013).
- Jordan, N.; Ritter, A.; Foerstendorf, H.; Scheinost, A.C.; Weiß, S.; Heim, K.; Grenzer, J.; Mücklich, A.; Reuther, H.
Adsorption mechanism of selenium(VI) onto maghemite
Geochimica et Cosmochimica Acta 103, 63–75 (2013).
- Joseph, C.; Stockmann, M.; Schmeide, K.; Sachs, S.; Brendler, V.; Bernhard, G.
Sorption of U(VI) onto Opalinus Clay: effects of pH and humic acid
Applied Geochemistry 36, 104–117 (2013).
- Joseph, C.; van Loon, L.R.; Jakob, A.; Steudtner, R.; Schmeide, K.; Sachs, S.; Bernhard, G.
Diffusion of U(VI) in Opalinus Clay: influence of temperature and humic acid
Geochimica et Cosmochimica Acta 109, 74–89 (2013).
- Kobayashi, T.; Scheinost, A.C.; Fellhauer, D.; Gaona, X.; Altmaier, M.
Redox behavior of Tc(VII)/Tc(IV) under various reducing conditions in 0.1 M NaCl solutions
Radiochimica Acta 101, 323–332 (2013).
- Koehler, M.; Degering, D.; Zessin, J.; Fuechtner, F.; Konheiser, J.
Radionuclide impurities in [¹⁸F]F⁻ and [¹⁸F]FDG for positron emission tomography
Applied Radiation and Isotopes 81, 268–271 (2013).
- Kozmenkov, Y.; Rohde, U.
Application of statistical uncertainty and sensitivity evaluations to a PWR LBLOCA analysis calculated with the code ATHLET. Part 1: uncertainty analysis
Kerntechnik 78, 354–361 (2013).
- Lederer, F.; Weinert, U.; Günther, T.; Raff, J.; Weiß, S.; Pollmann, K.
Identification of multiple putative S-layer genes partly expressed by *Lysinibacillus sphaericus* JG-B53
Microbiology 159, 1097–1108 (2013).
- Lucks, C.; Roßberg, A.; Tsushima, S.; Foerstendorf, H.; Fahmy, K.; Bernhard, G.
Formic acid interaction with uranyl(VI) ion: structural and photochemical characterization
Dalton Transactions 42, 13584–13589 (2013).
- Lütke, L.; Moll, H.; Bachvarova, V.; Selenska-Pobell, S.; Bernhard, G.
The U(VI) speciation influenced by a novel *Paenibacillus* isolate from Mont Terri Opalinus Clay
Dalton Transactions 42, 6979–6988 (2013).
- Macé, N.; Wieland, E.; Dähn, R.; Tits, J.; Scheinost, A.C.
EXAFS investigation on U(VI) immobilization in hardened cement paste: influence of experimental conditions on speciation
Radiochimica Acta 101, 379–389 (2013).
- Martínez-Torrents, A.; Meca, S.; Baumann, N.; Martí, V.; Giménez, J.; de Pablo, J.; Casas, I.
Uranium speciation studies at alkaline pH and in the presence of hydrogen peroxide using time-resolved laser-induced fluorescence spectroscopy
Polyhedron 55, 92–101 (2013).

- Mendes, M.; Leguay, S.; Le Naour, C.; Hamadi, S.; Roques, J.; Moisy, P.; Guillaumont, D.; Topin, S.; Aupiais, J.; Den Auwer, C.; Hennig, C.
Thermodynamic study of the complexation of protactinium(V) with diethylenetriaminepentaacetic acid
Inorganic Chemistry 52, 7497–7507 (2013).
- Merchel, S.; Bremser, W.; Bourlès, D.L.; Czeslik, U.; Erzinger, J.; Kummer, N.A.; Leanni, L.; Merkel, B.; Recknagel, S.; Schaefer, U.
Accuracy of ^9Be -data and its influence on ^{10}Be cosmogenic nuclide data
Journal of Radioanalytical and Nuclear Chemistry 298, 1871–1878 (2013).
- Merk, B.
Fine distributed moderating material with improved thermal stability applied to enhance the feedback effects in SFR cores
Science and Technology of Nuclear Installations, 217548 (2013).
- Merk, B.
Moderating material to compensate the drawback of high minor actinide containing transmutation fuel on the feedback effects in SFR cores
Science and Technology of Nuclear Installations, 172518 (2013).
- Merk, B.; Glivici-Cotruță, V.; Duerigen, S.; Rohde, U.; Kliem, S.
Overview of major HZDR developments for fast reactor analysis
Nuclear Engineering and Design 265, 1194–1204 (2013).
- Moll, H.; Lütke, L.; Barkleit, A.; Bernhard, G.
Curium(III) speciation studies with cells of a groundwater strain of *Pseudomonas fluorescens*
Geomicrobiology Journal 30, 337–346 (2013).
- Müller, K.; Foerstendorf, H.; Brendler, V.; Rossberg, A.; Stolze, K.; Gröschel, A.
The surface reactions of U(VI) on $\gamma\text{-Al}_2\text{O}_3$ – In situ spectroscopic evaluation of the transition from sorption complexation to surface precipitation
Chemical Geology 357, 75–84 (2013).
- Müller, K.; Sasaki, T.
Complex formation of Np(V) with fulvic acid at tracer metal concentration
Radiochimica Acta 101, 1–6 (2013).
- Osman, A.A.A.; Geipel, G.; Bernhard, G.
Interaction of uranium(VI) with bioligands present in human biological fluids: the case study of urea and uric acid
Radiochimica Acta 101, 139–147 (2013).
- Osman, A. A.A.; Geipel, G.; Bernhard, G.; Worch, E.
Investigation of uranium binding forms in selected german mineral waters
Environmental Science and Pollution Research 20, 8629–8635 (2013).
- Payne, T.E.; Brendler, V.; Ochs, M.; Baeyens, B.; Brown, P.L.; Davis, J.A.; Ekberg, C.; Kulik, D.A.; Lützenkirchen, J.; Missana, T.; Tachi, Y.; van Loon, L.R.; Altmann, S.
Guidelines for thermodynamic sorption modelling in the context of radioactive waste disposal
Environmental Modelling & Software 42, 143–156 (2013).
- Perea-Buceta, J.E.; Wirtanen, T.; Laukkanen, O.V.; Mäkelä, M.K.; Nieger, M.; Melchionna, M.; Huittinen, N.; Lopez-Sanchez, J.A.; Helaja, J.
Cycloisomerization of 2-alkynylanilines to indoles catalyzed by carbon-supported gold nanoparticles and subsequent homocoupling to 3,3'-biindoles
Angewandte Chemie – International Edition 52, 11835–11839 (2013).
- Pietrzyk, U.; Zakhnini, A.; Axer, M.; Sauerzapf, S.; Benoit, D.; Gaens, M.
EduGATE – Basic examples for educative purpose using the GATE simulation platform
Zeitschrift für Medizinische Physik 23, 65–70 (2013).
- Prieur, D.; Martin, P.; Lebreton, F.; Delahaye, T.; Banerjee, D.; Scheinost, A.C.; Jankowiak, A.
Accommodation of multivalent cations in fluorite-type solid solutions: case of Am-bearing UO_2
Journal of Nuclear Materials 434, 7–16 (2013).
- Prinz, J.; Schreiber, B.; Olejko, L.; Oertel, J.; Rackwitz, J.; Keller, A.; Bald, I.
DNA origami substrates for highly sensitive surface-enhanced Raman scattering
Journal of Physical Chemistry Letters 4, 4140–4145 (2013).
- Pürschel, M.; Sachs, S.; Bernhard, G.; Ender, V.
Uptake of multi-disperse starch by anion exchangers
Journal of Physical Science and Application 3, 147–155 (2013).

- Radeva, G.; Kenarova, A.; Bachvarova, V.; Flemming, K.; Popov, I.; Vassilev, D.; Selenska-Pobell, S.
Bacterial diversity at abandoned uranium mining and milling sites in Bulgaria as revealed by 16S rRNA genetic diversity study
Water, Air & Soil Pollution 224, Art. No. 1748 (2013).
- Rachamin, R.; Fridman, E.; Galperin, A.
Design and analysis of an innovative pressure tubes light water reactor with variable moderator control
Annals of Nuclear Energy 60, 248–255 (2013).
- Rachamin, R.; Wemple, C.; Fridman, E.
Neutronic analysis of SFR core with HELIOS-2, SERPENT, and DYN3D codes
Annals of Nuclear Energy 55, 194–204 (2013).
- Raditzky, B.; Sachs, S.; Schmeide, K.; Barkleit, A.; Geipel, G.; Bernhard, G.
Spectroscopic study of americium(III) complexes with nitrogen containing organic model ligands
Polyhedron 65, 244–251 (2013).
- Schleuter, D.; Günther, A.; Paasch, S.; Ehrlich, H.; Kljajic, Z.; Hanke, T.; Bernhard, G.; Brunner, E.
Chitin-based renewable materials from marine sponges for uranium adsorption
Carbohydrate Polymers 92, 712–718 (2013).
- Schmidt, M.; Lee, S. S.; Wilson, R. E.; Knope, K. E.; Bellucci, F.; Eng, P. J.; Stubbs, J.; Soderholm, L.; Fenter, P.
Surface-mediated formation of Pu(IV) nanoparticles at the muscovite-electrolyte interface
Environmental Science & Technology 47, 14178–14184 (2013).
- Schymura, S.; Scalia, G.
On the effect of carbon nanotubes on properties of liquid crystals
Philosophical Transactions of the Royal Society A 371, 20120261 (2013).
- Takao, K.; Takao, S.; Ikeda, Y.; Bernhard, G.; Hennig, C.
Uranyl-halide complexation in N,N-dimethylformamide: halide coordination trend manifests hardness of $[\text{UO}_2]^{2+}$
Dalton Transactions 42, 13101–13111 (2013).
- Tondera, C.; Laube, M.; Wimmer, C.; Kniess, T.; Mosch, B.; Großmann, K.; Pietzsch, J.
Visualization of cyclooxygenase-2 using a 2,3-diarylsubstituted indole-based inhibitor and confocal laser induced cryofluorescence microscopy at 20 K in melanoma cells in vitro
Biochemical and Biophysical Research Communications 430, 301–306 (2013).
- Veeramani, H.; Scheinost, A.C.; Monsegue, N.; Qafoku, N.P.; Kukkadapu, R.; Newville, M.; Lanzirotti, A.; Pruden, A.; Murayama, M.; Hochella, M.F.
Abiotic reductive immobilization of U^{6+} by biogenic mackinawite
Environmental Science & Technology 47, 2361–2369 (2013).
- Wang, Y.; Frutschi, M.; Suvorova, E.; Phrommavanh, V.; Descostes, M.; Osman, Alfatih A.A.; Geipel, G.; Bernier-Latmani, R.
Mobile uranium(IV)-bearing colloids in a mining-impacted wetland
Nature Communications 4, 2942 (2013).
- Weinert, U.; Pollmann, K.; Raff, J.
Fluorescence resonance energy transfer by S-layer coupled fluorescence dyes
Sensors and Actuators B 185, 553–559 (2013).
- Zakhnini, A.; Kulenkampff, J.; Sauerzapf, S.; Pietrzyk, U.; Lippmann-Pipke, J.
Monte Carlo simulations of GeOPET experiments: 3D images of tracer distributions (^{18}F , ^{124}I and ^{58}Co) in Opalinus Clay, anhydrite and quartz
Computers & Geosciences 57, 183–196 (2013).

EXTENDED ABSTRACTS, REPORTS, CONTRIBUTIONS

- Barth, T.; Kulenkampff, J.; Ludwig, M.; Bras, S.; Gründig, M.; Franke, K.; Lippmann-Pipke, J.; Hampel, U.
Study of particle deposition and resuspension in pebble beds using positron emission tomography
Proceedings of the 15th International Topical Meeting on Nuclear Reactor Thermalhydraulics NURETH-15, May 12–15, 2013, Pisa, Italy, NURETH15-280, 10 p. (2013).
- Brockmann, S.; Arnold, T.; Bernhard, G.
Wechselwirkung von Uran(VI) mit Biofilmen
Wissenschaftlich-Technische Berichte / Helmholtz-Zentrum Dresden-Rossendorf; HZDR-043 (2013).
- Fahmy, K.
Fourier transform infrared spectroscopy for biophysical applications: technical aspects
Encyclopedia of Biophysics (Roberts, G. C. K., ed.), Springer, Berlin, 844–852 (2013).
- Flügge, J.; Stockmann, M.; Schneider, A.; Noseck, U.
The impact of climate transitions on the radionuclide transport through a sedimentary aquifer
Assessing and Managing Groundwater in Different Environments” (Cobbing, J.; Adams, S.; Dennis, I.; Riemann, K., eds.), 147–164, CRC Press, Leiden, The Netherlands (2013).
- Franzen, C.; Siedler, G.; Franzen, C.; Vetter, S.
Orthogonal IRT Imaging
Proceedings of the 2013 Digital Heritage Congress (DigitalHeritage) Vol. 1 (Addison, A.C.; Guidi, G.; De Luca, L.; Pescarin, S., eds.) Vol. 1, 633–636 (2013).
- Fridman, E.; Leppänen, J.; Wemple, C.
Comparison of Serpent and HELIOS-2 as applied for the PWR few-group cross section generation
International Conference on Mathematics and computational Methods Applied to Nuclear Science and Engineering (M&C 2013), May 05–09, 2013, Sun Valley, U.S.A. American Nuclear Society, LaGrange Park, U.S.A., Vol. 1, 693–703 (2013).
- Fridman, E.; Rachamin, R.; Shwageraus, E.
Generation of SFR few-group constants using the Monte Carlo code Serpent
International Conference on Mathematics and computational Methods Applied to Nuclear Science and Engineering (M&C 2013), May 05–09, 2013, Sun Valley, U.S.A. American Nuclear Society, LaGrange Park, U.S.A., Vol. 1, 2978–2985 (2013).
- Moll, H.; Lütke, L.; Bachvarova, V.; Steudtner, R.; Geißler, A.; Krawczyk-Bärsch, E.; Selenska-Pobell, S.; Bernhard, G.
Microbial Diversity in Opalinus Clay and Interaction of Dominant Microbial Strains with Actinides (Final Report BMWi Project No.: 02 E 10618)
Wissenschaftlich-Technische Berichte / Helmholtz-Zentrum Dresden-Rossendorf; HZDR-036 (2013).
- Rohde, U.; Kozmenkov, Y.
Sensitivity analysis o the ranking of input uncertainties withe respect to peak cladding temperature uncertainty in a PWR LBLOCA analysis
Proceeedings of the 23rd Symposium of AER on VVER Reactor Physics and Reactor Safety, October 30–04, 2013, Štrbské pleso, Slovakia, Kiadja az MTA Eneriatudományi Kutatóközpont, Budapest, 501–512 (2013).

LECTURES, ORAL PRESENTATIONS

- Arnold, T.
Rossendorf Research Update - Microbiological research in underground salt formations
Salt Club Meeting, September 16, 2013, Berlin, Germany (2013).
- Arnold, T.
Untersuchungen zu den Wechselwirkungen zwischen unter Tage lebenden Mikroorganismen mit Uran und deren Einfluss auf das Migrationsverhalten von Uran in gefluteten Urangruben
Kick-Off Meeting Verbund TransAqua, June 21, 2013, Munich, Germany (2013).
- Barth, T.; Kulenkampff, J.; Ludwig, M.; Bras, S.; Gründig, M.; Franke, K.; Lippmann-Pipke, J.; Hampel, U.
Study of particle deposition and resuspension in pebble beds using positron emission tomography
NURETH-15 – The 15th International Topical Meeting on Nuclear Reactor Thermalhydraulics, May 12–15, 2013, Pisa, Italy (2013).
- Barth, T.; Kulenkampff, J.; Ludwig, M.; Bras, S.; Gründig, M.; Franke, K.; Lippmann-Pipke, J.; Hampel, U.
Study of particle deposition and resuspension in pebble beds using positron emission tomography
WCIPT7 – 7th World Congress on Industrial Process Tomography, September 02–05, 2013, Wroclaw, Poland (2013).
- Bauer, J.D.; Labs, S.; Weiss, S.; Bayarjargal, L.; Curtis, H.; Morgenroth, W.; Bosbach, D.; Hennig, C.; Winkler, B.
Raman spectroscopy and powder diffraction study of synthetic coffinite (USiO₄) at high pressures
Goldschmidt 2013, August 25–30, 2013, Florence, Italy (2013).
- Baumann, N.; Arnold, T.
Messsystem zur Untersuchung von Metall-Fluoreszenzen in biologischer Matrix mikroskopischer Dimension
Projekt Strahlung und Umwelt II: Influence of Biofilms on Migration of Uranium, Americium and Europium in the Environment, June 20, 2013, Munich, Germany (2013).
- Bok, F.; Voigt, W.; Bube, C.; Wilhelm, S.; Moog, H.
A brief comparison of Pitzer databases for nuclear waste disposal modeling
Actinide and Brine Chemistry in a Salt Repository Workshop (III), April 15–17, 2013, Santa Fe, U.S.A. (2013).
- Borodkin, P.G.; Borodkin, G.I.; Adeev, V.A.; Konheiser, J.
Results of testing of calculation procedure for neutron fluence and spectrum on the VVER-440 RPV during operation with new fuel compositions
The 8th International Scientific and Technical Conference “Safety Assurance of NPP with WWER”, May 28–31, 2013, Podolsk, Russia (2013).
- Brendler, V.; Bok, F.; Müller, K.
Uranium sorption onto single mineral phases – approaching consistency and robustness
Actinides 2013 – 9th International Conference on the Chemistry and Physics of the Actinide Elements, July 21–26, 2013, Karlsruhe, Germany (2013).
- Duerigen, S.; Kliem, S.
The DYN3D trigonal-geometry diffusion model – verification using the AER-FCM-101 benchmark
23rd Symposium of AER on VVER Reactor Physics and Reactor Safety, October 30–04, 2013, Štrbské pleso, Slovakia (2013).
- Dumas, T.; Fellhauer, D.; Gaona, X.; Altmaier, M.; Scheinost, A.C.
Is plutonium being incorporated by magnetite under anoxic conditions?
Goldschmidt 2013, August 25–30, 2013, Florence, Italy (2013).
- Foerstendorf, H.
Spectroscopic investigations of actinides for ecological risk assessment in the context of nuclear waste disposal
Seminar of Department of Nuclear Engineering, Kyoto University, October 02, 2013, Kyoto, Japan (2013).
- Foerstendorf, H.
Spectroscopic investigations of actinides for ecological risk assessment in the context of nuclear waste disposal
Seminar of Quantum Beam Science Directorate, JAEA, September 30, 2013, Tokai, Ibaraki, Japan (2013).

- Foerstendorf, H.; Gückel, K.; Jordan, N.; Rossberg, A.; Brendler, V.
Surface speciation of dissolved radionuclides on mineral phases – A vibrational and X-ray absorption spectroscopic study
APSORC 13 – 5th Asia-Pacific Symposium on Radiochemistry, September 22–27, 2013, Kanazawa, Japan (2013).
- Foerstendorf, H.; Heim, K.; Jordan, N.
Sorption and desorption processes of U(VI) on iron (hydr)oxide phases
Goldschmidt 2013, August 25–30, 2013, Florence, Italy (2013).
- Franzen, C.
Geowissenschaftliche Berufsfelder – Als Mineralogin in der Endlagerforschung
Berufsfelder in den Geowissenschaften, July 15, 2013, Heidelberg, Germany (2013).
- Fridman, E.; Rachamin, R.; Shwageraus, E.
Generation of SFR few-group constants using the Monte Carlo code Serpent
M&C 2013 – International Conference on Mathematics and computational Methods Applied to Nuclear Science and Engineering, May 05–09, 2013, Sun Valley, U.S.A. (2013).
- Fritsch, K.; Schmeide, K.
Uranium(VI) sorption on montmorillonite in high ionic strength media
ABC-Salt Workshop III, April 15–17, 2013, Santa Fe, U.S.A. (2013).
- Hennig, C.
EXAFS and X-ray scattering as complementary techniques to determine metal coordination in solutions
School and Conference on Analysis of Diffraction Data in Real Space, March 18–22, 2013, Grenoble, France (2013).
- Hennig, C.
Formation and structure of polynuclear actinide(IV) carboxylates in aqueous solution
Laboratoire des Interactions Ligand-Actinide, CEA Marcoule, December 19, 2013, Marcoule, France (2013).
- Hennig, C.
Spectroscopic investigation of heavy metals
Universidad de Granada, Facultad de Ciencias, Departamento de Micobiología, May 21, 2013, Granada, Spain (2013).
- Holt, L.; Rohde, U.; Seidl, M.; Schubert, A.; van Uffelen, P.
Development of a General Coupling Interface for the Fuel Performance Code TRANSURANUS Tested with the Reactor Dynamic Code DYN3D
10th International Conference on WWER Fuel Performance, Modelling and Experimental Support, September 07–14, 2013, Sandanski, Bulgaria (2013).
- Husar, R.; Weiss, S.; Hennig, C.; Hübner, R.; Zänker, H.; Bernhard, G.
Investigation into the formation of Np(IV) silica colloids
Migration 2013 – 14th International Conference on the Chemistry and Migration Behaviour of Actinides and Fission Products in the Geosphere, September 08–13, 2013, Brighton, United Kingdom (2013).
- Konheiser, J.; Borodkin, P.; Borodkin, G.
Fluence calculation and reaction rates determination at the reactor pressure vessel Kola 3
13th AAA Usergroup Meeting, December 02, 2013, Garching, Germany (2013).
- Krawczyk-Bärsch, E.
Microbial experiments at URL sites: Influence on radionuclide
Final Workshop of the CROCK Project "Crystalline rock retention processes", May 14–16, 2013, Karlsruhe, Germany (2013).
- Krawczyk-Bärsch, E.
Microbial influence on the immobilization of radionuclides in crystalline rock environments
IGD-TP 4th Exchange Forum, October 29–30, 2013, Prague, Czech Republic (2013).
- Krawczyk-Bärsch, E.
Microbial influence on the migration behaviour of radionuclides
Coordination Meeting at Äspö, April 26, 2013, Äspö, Sweden (2013).
- Krawczyk-Bärsch, E.
Microbially mediated immobilization of radionuclide in subsurface crystalline rock environments
12th Symposium on remediation, September 26–27, 2013, Jena, Germany (2013).

- Kulenkampff, J.; Gründig, M.; Zakhnini, A.; Lippmann-Pipke, J.
PET-Prozessstomographie von Transportvorgängen in Bohrkernen zur Verbesserung des Prozessverständnisses und zur Verifikation von Modellcodes
73. Jahrestagung der Deutschen Geophysikalischen Gesellschaft, March 04–07, 2013, Leipzig, Germany (2013).
- Lebreton, F.; Martin, P.M.; Belin, R.C.; Horlait, D.; Dardenne, K.; Rothe, J.; Rossberg, A.; Scheinost, A.C.; Delahaye, T.; Blanchart, P.
U1-xAmxO₂±δ solid solution study
E-MRS 2013 Spring Meeting, May 27–31, 2013, Strasbourg, France (2013).
- Lederer, F.; Weinert, U.; Günther, T.; Raff, J.; Pollmann, K.
Identification of multiple S-layer genes that are expressed by *Lysinibacillus sphaericus* JG-B53 – A bacterial survival strategy in metalliferous environments?
FEMS 2013 – 5th Congress of European Microbiologists, July 21–25, 2013, Leipzig, Germany (2013).
- Lippold, H.
Isotopenaustausch-Studien zur Reversibilität der Metall-Huminstoff-Komplexbildung
4. Workshop zum Verbundprojekt "Rückhaltung endlagerrelevanter Radionuklide im natürlichen Tongestein und in salinaren Systemen", April 11–12, 2013, Karlsruhe, Germany (2013).
- Lucas, D.; Montoya, G.
Multiphase CFD @ HZDR – Strategy and research topics of the CFD department
ICONE21 – 21st International Conference on Nuclear Engineering, July 29–August 02, 2013, Chengdu, China (2013).
- Mansel, A.; Franke, K.; Fischer, S.; Steinbach, J.
Herstellung und Reinigung von ⁶⁴Cu am Leipziger Zyklotron Cyclone® 18/9
Wissenschaftsforum Chemie 2013 – Fachgruppe Nuklearchemie, September 01–04, 2013, Darmstadt, Germany (2013).
- Massarczyk, R.; Schwengner, R.; Dönauf, F.; Anders, M.; Bemmerer, D.; Beyer, R.; Bhatia, C.; Birgersson, E.; Butterling, M.; Elekes, Z.; Ferrari, A.; Hannaske, R.; Junghans, A.R.; Kempe, M.; Kelley, J.H.; Kögler, T.; Matic, A.; Menzel, M.L.; Müller, S.; Reinhardt, T.; Röder, M.; Rusev, G.; Schilling, K.D.; Schmidt, K.; Schramm, G.; Tonchev, A.P.; Tornow, W.; Wagner, A.
Dipole strength in Xe-Isotopes
4th Workshop on Nuclear Level Density and Gamma Strength, May 27–31, 2013, Oslo, Norway (2013).
- Massarczyk, R.; Schwengner, R.; Dönauf, F.; Anders, M.; Bemmerer, D.; Beyer, R.; Bhatia, C.; Birgersson, E.; Butterling, M.; Elekes, Z.; Ferrari, A.; Hannaske, R.; Junghans, A.R.; Kempe, M.; Kelley, J.H.; Kögler, T.; Matic, A.; Menzel, M.L.; Müller, S.; Reinhardt, T.; Röder, M.; Rusev, G.; Schilling, K.D.; Schmidt, K.; Schramm, G.; Tonchev, A.P.; Tornow, W.; Wagner, A.
Dipole strength in Xe-Isotopes
International Conference on Nuclear Data for Science and Technology 2013, March 04–08, 2013, New York, U.S.A. (2013).
- Merk, B.
Thermal stability of moderating material used to enhance the feedback coefficients in SFR cores
International Conference on Fast Reactors and Related Fuel Cycles: Safe Technologies and Sustainable Scenarios (FR13), March 04–07, 2013, Paris, France (2013).
- Merk, B.; Rohde, U.; Scholl, S.
The Molten Salt Fast Reactor as transmutation system
International Conference on Fast Reactors and Related Fuel Cycles: Safe Technologies and Sustainable Scenarios (FR13), March 04–07, 2013, Paris, France (2013).
- Moll, H.; Lütke, L.; Bachvarova, V.; Cherkouk, A.; Selenska-Pobell, S.; Bernhard, G.
Interactions of plutonium with a typical isolate from Mont Terri Opalinus Clay
5. Workshop zum Verbundprojekt „Rückhaltung endlagerrelevanter Radionuklide im natürlichen Tongestein und in salinaren Systemen“, September 30–October 01, 2013, Potsdam, Germany (2013).

- Moll, H.; Lütke, L.; Cherkouk, A.; Selenska-Pobell, S.; Bernhard, G.; Brendler, V.
Microbial influences on radionuclide behaviour – An example of less-understood problems and how to solve them
IGD-TP 4th Exchange Forum (EF4), October 29–30, 2013, Prague, Czech Republic (2013).
- Moog, H.C.; Bok, F.
THEREDA – Thermodynamic Reference Database
Goldschmidt 2013, August 25–30, 2013, Florence, Italy (2013).
- Müller, K.; Berger, J.; Cordiez, M.; Gröschel, A.; Foerstendorf, H.
Vibrational spectroscopic study of Np(V) sorption on mineral oxides
Goldschmidt 2013, August 25–30, 2013, Florence, Italy (2013).
- Müller, K.; Gröschel, A.
Identification of Np(V) sorption complexes at the hematite-water interface studied by in-situ ATR FT-IR spectroscopy
Actinides 2013 – 9th International Conference on the Chemistry and Physics of the Actinide Elements, July 21–26, 2013, Karlsruhe, Germany (2013).
- Poetsch, M.; Mansel, A.; Schnorr, R.; Haupt, S.; Kersting, B.
Extraktionsuntersuchungen von umweltrelevanten Radionukliden mit modifizierten Calix[4]arenen
Anakon 2013, March 04–07, 2013, Essen, Germany (2013).
- Rachamin, R.
Conceptual design of Pressure Tube Light Water Reactor with variable moderator control
R&D Seminar, Candu Energy Inc., October 24, 2013, Mississauga, Ontario, Canada (2013).
- Rachamin, R.
Conceptual design of Pressure Tube Light Water Reactor with variable moderator control
R&D Seminar, University of Ontario Institute of Technology, October 25, 2013, Oshawa, Ontario, Canada (2013).
- Rachamin, R.
Conceptual design of Pressure Tube Light Water Reactor with variable moderator control
R&D Seminar, AECL Chalk River Laboratories, October 22, 2013, Chalk River, Ontario, Canada (2013).
- Rachamin, R.; Fridman, E.
Steady state analysis of SFR cores using DYN3D-Serpent codes sequence
Annual Meeting on Nuclear Technology (Jahrestagung Kerntechnik), May 14–16, 2013, Berlin, Germany (2013).
- Raff, J.
Intelligente Biomoleküle zur Funktionalisierung von Kunststoffoberflächen beim Endanwender
Mitteldeutscher Kunststofftag 2013, June 26–27, 2013, Erfurt, Germany (2013).
- Raff, J.; Vogel, M.; Matys, S.; Bobeth, C.
Biomolekül-unterstützte Photokatalysatoren zur Wasserreinigung
Photokatalyse-Kolloquium, October 09, 2013, Frankfurt am Main, Germany (2013).
- Rohde, U.; Kliem, S.; Duerigen, S.; Bilodid, Y.
Status of development of the reactor dynamics code DYN3D
The 8th International Scientific and Technical Conference “Safety Assurance of NPP with WWER”, May 28–31, 2013, Podolsk, Russia (2013).
- Rohde, U.; Kozmenkov, Y.
Sensitivity analysis of the ranking of input uncertainties with respect to peak cladding temperature uncertainty in a PWR LBLOCA analysis
23rd Symposium of AER on VVER Reactor Physics and Reactor Safety, October 30–04, 2013, Štrbské pleso, Slovakia (2013).
- Sabău, A.; Jordan, N.; Lomenech, C.; Marmier, N.; Brendler, V.; Barkleit, A.; Surblé, S.; Toulhoat, N.; Pison, Y.; Moncoffre, N.; Giffaut, E.
Interaction of Eu(III) with calcium carbonate: spectroscopic characterization.
Goldschmidt 2013, August 25–30, 2013, Florence, Italy (2013).
- Sachs, S.; Heller, A.; Bernhard, G.
Interaction of Eu(III) with mammalian cells as a function of Eu(III) concentration and nutrient composition
APSORC 13 – 5th Asia-Pacific Symposium on Radiochemistry, September 22–27, 2013, Kanazawa, Japan (2013).
- Scheinost, A.C.
Electron transfer processes at the mineral/water interface in the context of anoxic radioactive waste disposal
Goldschmidt 2013, August 25–30, 2013, Florence, Italy (2013).

- Scheinost, A.C.
Reduction and immobilization processes of contaminants (Se, Tc, Pu) by Fe(II)-bearing minerals
Institutseminar am Institut für Radioökologie und Strahlenschutz der Universität Hannover, May 16, 2013, Hannover, Germany (2013).
- Scheinost, A.C.
Reduction and immobilization processes of contaminants (Se, Tc, Pu) by Fe(II)-bearing minerals
Chemical and Radiochemical Processes in the Environment, May 17, 2013, Nice, France (2013).
- Scheinost, A.C.
The Rossendorf Beamline at ESRF: A Pooled Facility of ACTINET-I3
2nd ACTINET-I3 Plenary Meeting, January 23–24, 2013, Avignon, France (2013).
- Scheinost, A.C.; Schmeisser, N.; Banerjee, D.; Rossberg, A.; Denecke, M.; Dardenne, K.; Rothe, J.; Daehn, R.
AcXAS: Actinide Reference X-ray Absorption Spectroscopy Database
2nd ACTINET-I3 Plenary Meeting, January 23–24, 2013, Avignon, France (2013).
- Schmeide, K.; Gürtler, S.; Bok, F.; Brendler, V.
Interaction of uranium(VI) and neptunium(V) with Äspö diorite under anoxic conditions
Final Workshop of the CROCK Project "Crystalline rock retention processes", May 14–16, 2013, Karlsruhe, Germany (2013).
- Schmeide, K.; Gürtler, S.; Müller, K.; Steudtner, R.; Joseph, C.; Bok, F.; Brendler, V.
Sorption of uranium and neptunium onto diorite from Äspö HRL
Goldschmidt 2013, August 25–30, 2013, Florence, Italy (2013).
- Schmoock, C.; Malkova, M.; Börnick, H.; Gravenhorst, O.; Hartmann, J.; Vogel, M.; Lehmann, F.; Kutschke, S.; Raff, J.; Worch, E.
Indirekte Bestimmung der photokatalytisch generierten Hydroxylradikale – Anwendungen zur Charakterisierung von erweiterten Oxidationsverfahren
Wasser 2013, May 06–08, 2013, Goslar, Germany (2013).
- Schott, J.; Acker, M.; Barkleit, A.; Taut, S.; Brendler, V.; Bernhard, G.
Latest results in the Eu(III)-B(OH)₃-organic System
4. Workshop zum Verbundprojekt "Rückhaltung endlagerrelevanter Radionuklide im natürlichen Tongestein und in salinaren Systemen", April 11–12, 2013, Karlsruhe, Germany (2013).
- Schott, J.; Acker, M.; Kretzschmar, J.; Barkleit, A.; Taut, S.; Brendler, V.; Bernhard, G.
Investigations to the Eu(III)-B(OH)₃-organic System at increased salt concentrations
Actinide and Brine Chemistry in a Salt Repository Workshop (III), April 15–17, 2013, Santa Fe, U.S.A. (2013).
- Schott, J.; Acker, M.; Kretzschmar, J.; Barkleit, A.; Taut, S.; Brendler, V.; Bernhard, G.
Investigations to the system Ln(III)/An(III)-B(OH)₃-organics
Migration 2013 – 14th International Conference on the Chemistry and Migration Behaviour of Actinides and Fission Products in the Geosphere, September 08–13, 2013, Brighton, United Kingdom (2013).
- Schymura, S.; Hildebrand, H.; Cydzik, I.; Bulgheroni, A.; Simonelli, F.; Holzwarth, U.; Kozempel, J.; Bilz, E.; Freyer, A.; Franke, K.; Gibson, N.
Radiolabelling of engineered nanoparticles – Different strategies for Ag⁰-NP, TiO₂-NP and MWCNTs
2nd QNano Integrating Conference, February 27– March 01, 2013, Prague, Czech Republic (2013).
- Steudtner, R.; Berger, M.; Müller, K.; Brendler, V.
Uranium(VI) sorption on mineral phases studied by in situ laser fluorescence spectroscopy
GDCh-Wissenschaftsforum Chemie 2013, September 01–04, 2013, Darmstadt, Germany
- Suhr, M.; Matys, S.; Raff, J.; Pollmann, K.
Metal interaction processes with cell wall components of Gram-positive bacteria studied by QCM-D
VAAM – Annual Conference of the Association for General and Applied Microbiology, March 10–13, 2013, Bremen, Germany (2013).

- Tsushima, S.; Rossberg, A.; Moll, H.
Exchange of oxygen in uranyl(VI) and water: two binuclear scenarios in acid and in base
Migration 2013 – 14th International Conference on the Chemistry and Migration Behaviour of Actinides and Fission Products in the Geosphere, September 08–13, 2013, Brighton, United Kingdom (2013).
- van Uffelen, P.; van de Laar, J.; Schubert, A.; Di Marcello, V.; Vlahovic, L.; Holt, L.
Modelling of Nuclear Fuel under Accident Conditions by means of TRANSURANUS
Technical meeting on modelling of water-cooled fuel including design basis and severe accidents, October 28–November 01, 2013, Chengdu, China (2013).
- Wolf, M.; Enzmann, F.; Kulenkampff, J.; Lippmann-Pipke, J.
3D Analysis of fluid flow in fissured salt rock
Migration 2013 – 14th International Conference on the Chemistry and Migration Behaviour of Actinides and Fission Products in the Geosphere, September 08–13, 2013, Brighton, United Kingdom (2013).
- Zänker, H.
Kolloide in der aquatischen Umwelt – Ein Überblick über die Kolloidarbeiten am Institut für Ressourcenökologie
Lecture given at Helmholtz-Institut Freiberg, April, 15, 2013, Freiberg, Germany (2013).
- Zirnstein, I.
Radioaktiv belastete Umwelt – Lebensräume für Bakterien?
11. Lange Nacht der Wissenschaften 2013, Juüy 05, 2013, Dresden, Germany (2013).
- Zirnstein, I.; Arnold, T.
Insights into the biodiversity of salt sumps in the ASSE II salt mine, Germany
ABC-Salt Workshop III Actinide and Brine Chemistry in a Salt Repository, April 15–17, 2013, Santa Fe, U.S.A. (2013).
- Zirnstein, I.; Baumann, N.; Arnold, T.
Microbial diversity of the water from uranium mine Königstein
Projekt Strahlung und Umwelt II: Influence of Biofilms on Migration of Uranium, Americium and Europium in the Environment, June 20, 2013, Munich, Germany (2013).

▣ POSTERS

- Attia, E.; Fahmy, K.
Spectroscopic characterization of transition metal complexes with quercetin in aqueous solutions
Jahrestagung der Deutschen Gesellschaft für Biophysik, September 23–26, 2013, Göttingen, Germany (2013).
- Bok, F.; Richter, A.; Brendler, V.
A comparison of Pitzer databases for nuclear waste disposal modelling
Goldschmidt 2013, August 25–30, 2013, Florence, Italy (2013).
- Brendler, V.; Bok, F.; Marquardt, C.; Altmaier, M.
THEREDA revisited – project status in 2013
Migration 2013 – 14th International Conference on the Chemistry and Migration Behaviour of Actinides and Fission Products in the Geosphere, September 08–13, 2013, Brighton, United Kingdom (2013).
- Brockmann, S.; Arnold, T.; Großmann, K.
Ortsaufgelöste Analyse von Uranspezies mittels einem gekoppelten System aus konfokaler Laser-Scanning Mikroskopie (CLSM) und Laser induzierter Fluoreszenzspektroskopie (LIFS)
7. Workshop RCA, June 10–11, 2013, Dresden, Germany (2013).
- Comarmond, M. J.; Foerstendorf, H.; Steudtner, R.; Chong, E.; Heim, K.; Müller, K.; Gückel, K.; Brendler, V.; Payne, T. E.
Investigations of the sorption of U(VI) onto SiO₂ in the presence of phosphate: In search of a ternary surface complex
Migration 2013 – 14th International Conference on the Chemistry and Migration Behaviour of Actinides and Fission Products in the Geosphere, September 08–13, 2013, Brighton, United Kingdom (2013).

- Ferrari, A.
Aspects of the core shielding assessment for the design of FASTEF-MYRRHA
525. WE-Heräus-Seminar "Nuclear Physics Data for the Transmutation of Nuclear Waste", February 25–27, 2013, Bad Honnef, Germany (2013).
- Ferrari, A.; Di Maria, S.; Fernandez, R.; Konheiser, J.; Ottolini, M.; Sarotto, M.; Stankovskiy, A.
Aspects of the core shielding assessment for the FASTEF-MYRRHA design
International Conference on Fast Reactors and Related Fuel Cycles: Safe Technologies and Sustainable Scenarios (FR13), March 04–07, 2013, Paris, France (2013).
- Fischer, S.; Steudtner, R.; Maffert, A.; Vogel, M.; Franzen, C.; Barkleit, A.; Raff, J.
Formation of Se(0) nanoparticles by bacteria
8th HZDR PhD Seminar, October 07–09, 2013, Bautzen, Germany (2013).
- Fischermeier, E.; Sayed, A.; Oertel, J.; Fahmy, K.
Membrane nanodiscs: a platform for the structural and functional characterization of a bacterial PIB-type ATPase
Jahrestagung der Deutschen Gesellschaft für Biophysik, September 23–26, 2013, Göttingen, Germany (2013).
- Franzen, C.; Hering, D.; Jordan, N.
Retention of selenate at the water-mineral interface in the context of salt dome repositories
Goldschmidt 2013, August 25–30, 2013, Florence, Italy (2013).
- Fridman, E.; Rachamin, R.
On applicability of the 3D nodal code DYN3D for the analysis of SFR cores
International Conference on Fast Reactors and Related Fuel Cycles: Safe Technologies and Sustainable Scenarios (FR13), March 04–07, 2013, Paris, France (2013).
- Fritsch, K.; Schmeide, K.
Uranium(VI) retention in clay rocks with saline pore waters
Kompetenzzentrum Ost für Kerntechnik, December 12, 2013, Dresden, Germany (2013).
- Fritsch, K.; Schmeide, K.
Uranium(VI) sorption on montmorillonite at high ionic strengths
4. Workshop des Verbundprojekts „Rückhaltung endlagerrelevanter Radionuklide im natürlichen Tongestein und in salinaren Systemen“, April 12, 2013, Karlsruhe, Germany (2013).
- Fritsch, K.; Schmeide, K.; Bernhard, G.
Investigation of the mobility of uranium(VI) in argillaceous rock at higher salinity
Migration 2013 – 14th International Conference on the Chemistry and Migration Behaviour of Actinides and Fission Products in the Geosphere, September 08–13, 2013, Brighton, United Kingdom (2013).
- Gagell, C.; Röske, K.; Arnold, T.
Microbial communities in flooded underground uranium mines of East Germany
2nd International Conference on microbial diversity, October 23–25, 2013, Torino, Italy (2013).
- Gückel, K.; Foerstendorf, H.; Kruse, C.; Müller, K.
Analyse von aquatischen und sorbierten Actinidspezies mittels Abgeschwächte Totalreflexion (ATR) FT-IR Spektroskopie
7. Workshop RCA, June 10–11, 2013, Dresden, Germany (2013).
- Hassan Obeid, M.; Geissler, A.; Solioz, M.; Fahmy, K.; Oertel, J.
Influence of low (radio)metal concentrations on bacterial growth using calorimetric metabolic monitoring
Jahrestagung der Deutschen Gesellschaft für Biophysik, September 23–26, 2013, Göttingen, Germany (2013).
- Hennig, C.; Takao, K.; Takao, S.; Weiss, S.; Kraus, W.; Emerling, F.; Scheinost, A.C
Formation of actinide(IV) carboxylate complexes in aqueous solution – The unexpeted predominance of hexanuclear species
Actinides 2013 – 9th International Conference on the Chemistry and Physics of the Actinide Elements, July 21–26, 2013, Karlsruhe, Germany (2013).
- Hildebrand, H.; Franke, K.; Gibson, N.; Cydzik, I.; Simonelli, F.; Bulgheroni, A.; Holzwarth, U.; Bilz, E.; Freyer, A.
Radiolabelling of silver and titania nanoparticles as a tool for sensitive detection of nanoparticle release from surface coatings
3. Clustertreffen NanoCare / NanoNature, January 14–15, 2013, Frankfurt am Main, Germany (2013).

- Jordan, N.; Domaschke, S.; Foerstendorf, H.; Scheinost, A.C.; Weiß, S.; Heim, K.
Sorption of selenium oxyanions onto hematite.
Migration 2013 – 14th International Conference on the Chemistry and Migration Behaviour of Actinides and Fission Products in the Geosphere, September 08–13, 2013, Brighton, United Kingdom (2013).
- Krawczyk-Bärsch, E.; Pedersen, K.; Arnold, T.; Bok, F.; Lehtinen, A.
Microbial mediated immobilization of radionuclide in a future crystalline nuclear-waste repository
EURADWASTE '13, 8th EC Conference on the Management of Radioactive Waste, October 14–16, 2013, Vilnius, Lithuania (2013).
- Kretzschmar, J.; Barkleit, A.; Brendler, V.; Brunner, E.
NMR Spectroscopy in Nuclear Safety Research
15th JCF Frühjahrssymposium, March 06–09, 2013, Berlin, Germany (2013).
- Kretzschmar, J.; Jordan, N.; Brendler, E.
⁷⁷Se-NMR spectroscopic investigations on aqueous selenium speciation at higher temperatures and in the presence of divalent metal ions
EURACT-NMR Workshop 2013, July 17–19, 2013, Karlsruhe, Germany (2013).
- Labs, S.; Weiss, S.; Hennig, C.; Hübner, R.; Curtis, H.; Bosbach, D.
Synthesis and structure investigation of USiO₄ – Comparison between local structure and bulk
E-MRS 2013 Spring Meeting, May 27–31, 2013, Strasbourg, France (2013).
- Lippold, H.; Lippmann-Pipke, J.
Radiotracer exchange studies on the reversibility of interaction processes related to humic-bound metal transport
Migration 2013 – 14th International Conference on the Chemistry and Migration Behaviour of Actinides and Fission Products in the Geosphere, September 08–13, 2013, Brighton, United Kingdom (2013).
- Mansel, A.; Poetsch, M.; Franke, K.
Herstellung und Reinigung von ⁵⁶Co, ⁶⁴Cu und ⁸⁵Sr am Leipziger Zyklotron Cyclone 18/9
Anakon 2013, March 04–07, 2013, Essen, Germany (2013).
- Marquardt, C.M.; Altmaier, M.; Bube, C.; Bok, F.; Brendler, V.; Gaona, X.; Moog, H.; Schrage, T.; Munoz, A.; Richter, A.; Sukhanov, D.; Voigt, W.; Wilhem, S.
ThEREDA Database Project
GDCh Wissenschaftsforum Chemie 2013, September 01–04, Darmstadt, Germany (2013).
- Mickein, K.; Kutschke, S.; Pollmann, K.; Kulenkampff, J.; Lippmann-Pipke, J.
Feasibility studies with GeoPET: microbial processes tomography in geological environments
VAAM – Annual Conference of the Association for General and Applied Microbiology, March 10–13, 2013, Bremen, Germany (2013).
- Moll, H.; Lütke, L.; Bachvarova, V.; Geissler, A.; Selenska-Pobell, S.; Bernhard, G.
Bacterial diversity in Mont Terri Opalinus Clay and the influence of the bacterial *Sporomusa* sp. isolate on plutonium speciation
Migration 2013 – 14th International Conference on the Chemistry and Migration Behaviour of Actinides and Fission Products in the Geosphere, September 08–13, 2013, Brighton, United Kingdom (2013).
- Pollmann, K.; Günther, T.; Suhr, M.; Weinert, U.; Kutschke, S.; Lehmann, F.; Raff, J.
Surface functionalization for technical applications using bacterial S-layers
EURO BioMAT 2013 – European Symposium on Biomaterials and Related Areas, April 23–24, 2013, Weimar, Germany (2013).
- Richter, C.; Stockmann, M.; Brendler, V.; Großmann, K.
Clarification of the sorption behavior of uranium onto mica and feldspar
15th JCF Frühjahrssymposium, March 06–09, 2013, Berlin, Germany (2013).
- Schmeide, K.; Gürtler, S.; Bok, F.; Brendler, V.
Interaction of uranium(VI) and neptunium(V) with Äspö diorite under anoxic conditions
Final Workshop of the CROCK Project "Crystalline rock retention processes", May 14–16, 2013, Karlsruhe, Germany (2013).

- Sabău, A.; Jordan, N.; Lomenech, C.; Marmier, N.; Brendler, V.; Barkleit, A.; Surblé, S.; Toulhoat, N.; Pipon, Y.; Moncoffre, N.; Giffaut, E.
Study of europium and nickel interaction with calcite - batch experiments and spectroscopic characterization.
Migration 2013 – 14th International Conference on the Chemistry and Migration Behaviour of Actinides and Fission Products in the Geosphere, September 08–13, 2013, Brighton, United Kingdom (2013).
- Schmoock, C.; Börnick, H.; Worch, E.; Vogel, M.; Lehmann, F.; Bobeth, C.; Matys, S.; Kutschke, S.; Raff, J.
Neue photokatalytisch aktive Verbundmaterialien zur Eliminierung von pharmazeutischen Reststoffen – Interaktion zwischen S-Layer-Proteinen und photokatalytischem System
3. Clustertreffen NanoCare / NanoNature, January 14–15, 2013, Frankfurt am Main, Germany (2013).
- Schymura, S.; Hildebrand, H.; Franke, K.
Radiolabelling of engineered nanoparticles – alternative strategies for Ag⁰-NP, TiO₂-NPs and CNTs
2nd QNano Integrating Conference, February 27– March 01, 2013, Prague, Czech Republic (2013).
- Schymura, S.; Weiß, S.; Zänker, H.; Franke, K.
Colloidal Stability of Carbon Nanotubes - A Matter of Modification
3. Clustertreffen NanoCare / NanoNature, January 14–15, 2013, Frankfurt am Main, Germany (2013).
- Steutner, R.; Drobot, B.; Raff, J.; Scheinost, A.C.; Brendler, V.
Uranium(VI) complexation with carbonate studied by cryo-TRLFS and PARAFAC
Anakon 2013, March 04–07, 2013, Essen, Germany (2013).
- Steutner, R.; Maffert, A.; Vogel, M.; Franzen, C.; Scheinost, A.C.
Formation of Se(0) nanoparticles by *Azospirillum brasilense*
Goldschmidt 2013, August 25–30, 2013, Florence, Italy (2013).
- Steutner, R.; Müller, K.; Meusel, T.; Brendler, V.
Preliminary multi-method spectroscopic approach for the uranium(VI) hydrolysis at temperatures up to 60 °C
DMG-DGK-BMBF-ImmoRad Workshop "From atomistic calculations to thermodynamic modelling", February 18–22, 2013, Frankfurt, Germany (2013).
- Stockmann, M.; Brendler, V.; Richter, C.; Flüge, J.; Britz, S.; Noseck, U.
Environmental parameters that determine distribution coefficients of radionuclides for repositories
Goldschmidt 2013, August 25–30, 2013, Florence, Italy (2013).
- Suhr, M.; Matys, S.; Viacava Romo, K.E.; Raff, J.; Pollmann, K.
Adsorption behavior and heavy metal interaction processes of cellular components of Gram-positive bacteria investigated by QCM-D
International Soft Matter Conference 2013, September 15–19, 2013, Rome, Italy (2013).
- Suhr, M.; Matys, S.; Viacava Romo, K.E.; Raff, J.; Pollmann, K.
Biosorption of heavy metals and nanoparticles by Gram-positive bacteria and cellular components
8th HZDR PhD Seminar, October 07–09, 2013, Bautzen, Germany (2013).
- Suhr, M.; Vogel, M.; Matys, S.; Raff, J.; Pollmann, K.
Industrial applicability of microbial interaction with metals and metalloids
Engineering Life 2013: Bio-molecular principles for novel methods and materials, September 17–18, 2013, Dresden, Germany (2013).
- Tondera, C.; Laube, M.; Wimmer, C.; Kniess, T.; Mosch, B.; Großmann, K.; Pietzsch, J.
Visualization of cyclooxygenase-2 by confocal laser induced cryofluorescence microscopy at 20 K using a novel autofluorescent inhibitor in amelanotic and melanotic melanoma cells
8th World Congress of Melanoma, 9th Congress of the European Association of Dermatology (EADO), 7th Interdisciplinary Melanoma/Skin Cancer Meeting, and the 3rd European Post-Chicago Melanoma Meeting, July 17–20, 2013, Hamburg, Germany (2013).

Toulhoat, N.; Pipon, Y.; Moncoffre, N.; Sabău, A.; Lomenech, C.; Jordan, N.; Barkleit, A.; Marmier, N.; Brendler, V.; Surblé, S.; Giffaut, E.
Incorporation of Europium and Nickel in calcite studied by Rutherford Backscattering Spectrometry
21st International Conference on Ion Beam Analysis, June 23–28, 2013, Seattle, U.S.A. (2013).

Zirnstein, I.; Arnold, T.; Röske, K.; Röske, I.
Bacterial and archaeal community in a flooding uranium mine, Königstein (Germany)
2nd International Conference on microbial diversity, October 23–25, 2013, Torino, Italy (2013).

AWARD

Hofinger, J.; Günther, T.; Wengrzik, S.; Matys, S.; Raff, J.
Team BioBASE
Winner of “futureSAX Ideenwettbewerb”
Sächsische Staatsministerium für Wirtschaft, Arbeit und Verkehr
June 25, 2013.

DOCTORAL THESES

Brockmann, S.
Zur chemischen Identifizierung und Visualisierung von Uranspezies in Biofilm und Euklena Mutabilis Zellen
Technische Universität Dresden, Dresden, Germany (2013).

Lederer, F.
Genetische Modifizierung bakterieller S-layer-Proteine zur Erzeugung maßgeschneiderter Proteinvarianten für technische Anwendungen
Universität Rostock, Rostock, Germany (2013).

Duerigen, S.
Neutron transport in hexagonal reactor cores modeled by trigonal-geometry diffusion and simplified P3 nodal methods
Karlsruhe Institute of Technology, Karlsruhe, Germany (2013).

Lucks, C.
Untersuchungen zur Struktur von wassergelösten und an Hämatit sorbierten Uran(VI)-Komplexen mit aliphatischen (Hydroxy-)Carbonsäuren: Kombination verschiedener spektroskopischer Methoden mit Faktorenanalyse und quantenchemischen Berechnungen
Technische Universität Dresden, Dresden, Germany (2013).

Gückel, K.
Structural analysis of ternary actinyl(V/VI) sorption complexes on gibbsite – A combined quantum chemical and spectroscopic approach
Technische Universität Dresden, Dresden, Germany (2013).

Lütke, L.
Interaction of Selected Actinides (U, Cm) with Bacteria Relevant to Nuclear Waste Disposal
Technische Universität Dresden, Dresden, Germany (2013).

Joseph, C.
The ternary system U(VI) / humic acid / Opalinus Clay
Technische Universität Dresden, Dresden, Germany (2013).

Weinert, U.

**Erzeugung S-Layer basierter
fluoreszierender Schichten für technische
Anwendungen**

*Technische Universität Dresden, Dresden,
Germany (2013).*

MASTER, DIPLOMA, BACHELOR

Domaschke, K.

**Multidimensionale Spektrenanalyse mittels
neuronaler Netze**

*Hochschule Zittau/Görlitz, Zittau, Germany
(2013).*

Domaschke, S.

**Untersuchung des Sorptionsverhaltens von
Selen-Spezies an Hämatit**

*Hochschule Zittau/Görlitz, Zittau, Germany
(2013).*

Gröschel, A.

**Schwingungsspektroskopische
Untersuchungen der Sorption von Np(V) an
Mineraloxiden (Al₂O₃, SiO₂, TiO₂) in
wässriger Lösung**

*Dresden University of Applied Sciences,
Dresden, Germany (2013).*

Hering, D.

Sorption von Se(VI) an γ -Al₂O₃

*University of Applied Sciences Zittau/Görlitz,
Zittau, Germany (2013).*

Jäckel, E.

**Spektroskopische Untersuchungen von
Uran(VI) und Uran(IV) - Redoxprozesse und
Komplexierungsverhalten in Gegenwart
organischer Säuren**

*Hochschule Zittau/Görlitz, Zittau, Germany
(2013).*

Maffert, A.

**Charakterisierung der Wechselwirkung von
Selen mit dem Bakterium *Azospirillum
brasiliense***

*International Institute (IHI) Zittau, Zittau,
Germany (2013).*

Viacava Romo, K. E.

**Investigation of heavy metals sorption
behavior of isolated bacterial cell wall
components of Gram-positive bacteria using
ICP-MS and TRIFS**

*Technische Universität Bergakademie Freiberg,
Germany (2013).*

Zabelt, D.

**Untersuchungen zur Abtrennung von
Uranverbindungen aus Grubenwässern**

*Technische Universität Bergakademie Freiberg,
Freiberg, Germany (2013).*

Zehlike, L.

**Durchführung von Sorptions- und
Desorptionsversuchen von Uran(VI) an
Montmorillonit**

*Technische Universität Dresden, Dresden,
Germany (2013).*

SCIENTIFIC ACTIVITIES

- ▣ SEMINARS (TALKS OF VISITORS)
- ▣ WORKSHOPS
- ▣ TEACHING ACTIVITIES

Ansoborlo, E.

CEA/DEN/DRCP/CETAMA, Marcoule, France

**Researches developed at CEA in the field of
speciation applied to environment and
toxicology**

February 28, 2013

Müller, J.

University of Münster, Germany

**Metals inside of DNA: site-specific
functionalization of nucleic acids with metal
ions**

September 04, 2013

Schierz, A.

Center for Research in Water Resources,

University of Texas at Austin, U.S.A.

**Fate of mercury and methylmercury in
contaminated sediments – From the lab to the
field**

July 16, 2013

Simoni, E.

IPNO, Paris-Sud University, Orsay, France

**Structural studies of the actinides/
biomolecules interactions**

July 19, 2013

Skerencak-Frech, A.

Institute for Nuclear Waste Disposal, Karlsruhe

Institute of Technology (KIT); Physikalisch-

Chemisches Institut, Universität Heidelberg,

Germany

**The complexation of trivalent actinides with
inorganic and organic ligands at T = 25 to
200 °C: application of TRLFS and EXAFS at
high temperatures**

November 28, 2013

Swanson, J.

Los Alamos National Laboratory, Carlsbad,

U.S.A.

**Influence of indigenous microorganisms on
salt-based nuclear waste repositories**

September 19, 2013

WORKSHOPS; (CO)-ORGANIZED BY THE IRE

Helmholtz Meeting

“Research on Waste Repositories“,

Institute for Waste Disposal (INE), KIT, Karlsruhe,

Institute of Energy and Climate Research (IEK), FZJ, Jülich, and

Institute of Resource Ecology (IRE), HZDR, Dresden

HZDR, Dresden, Germany, February 20–21, 2013.

Alekseev, E. V.

**Progress in actinide solid state chemistry
research at IEK-6, Jülich**

Altmaier, M.

Aquatische Chemie und Thermodynamik

Kienzler, B.

Endlagersicherheit

Kliem, S.

**The Reactor Safety Research within the
Institute of Resource Ecology**

Krawczyk-Bärsch, E.

**Speciation of uranium in biofilms and
groundwater seeps from the granitic rock
walls in the future nuclear HLW repository
in Finland**

Labs, S.

**Coffinite, thorite and their solid solutions –
Comparison of bulk and local structure**

Neumeier, S.

**Stand der Arbeiten zu keramischen
Materialien für die nukleare Entsorgung**

Schäfer, T.

Geochemie

Schmeide, K.

**U(VI) sorption and diffusion on/in Opalinus
Clay and clay minerals – Influence of clay
organics, temperature and ionic strength**

International DYN3D Users and Developers Meeting

HZDR, Dresden, Germany, April 18–19, 2013.

Baier, S.

Heat conduction model for prismatic HTRs

Bilodid, Y.

**Cross section preparation and historical
effects in burn-up**

Däubler, M.

**DYNSUB: A parallelized high-fidelity
coupled code system for reactor core safety
assessments**

**Parallel MPI based coupling of DYN3D and
Neptune CFD/SYRTHES**

Duerigen, S.

**Neutron transport in hexagonal reactor cores
modeled by trigonal-geometry diffusion and
simplified P3 Nodal methods**

Fridman, E.

Cross section preparation by SERPENT

Galchenko, V.

**The influence of water temperature profile on
fuel assembly and fuel temperature profiling
on a fuel pellet on macro cross section
preparation**

- Gommlich, A.
DYN3D code management and maintenance
- Grahn, A.
Thermal hydraulic calculations based on coupling the neutron kinetic core model of DYN3D with the 3D CFD code ANSYS-CFX

Using Bugzilla for improved communication between DYN3D users and developers
- Grundmann, U.
Generation and application of SPH-factors in pin-wise calculations with DYN3D
- Hádek, J.
The DYN3D code as a tool for research and development and safety analysis in ÚJV Řež, a.s.
- Holt, L.
PWR control rod ejection simulations including high burn-up phenomena – DYN3D coupled via an at HZDR developed general coupling interface for TRANSURANUS
- Kliem, S.
Further directions of the development of the reactor dynamics code DYN3D
- Ovdiienko, I.
Using DYN3D code by SSTC N&RS for independent verifying calculations
- Palahina, J.
Sample calculations of the safety analysis by DYN3D to overcooling
- Rohde, U.
Overview on the status of development of the code DYN3D
- Sasinovich, V.
Control rod ejection as example of calculations of NPP safety assessment by DYN3D
- Seidl, M.
How to choose appropriate boundary conditions for PWR rod ejection transients from the point of view of a utility
- Strmensky, C.
Experiences with DYN3D for safety analysis of VVER440 reactors

Workshop of the Nuclear Energy and Safety Research Department, Laboratory for Waste Management (LES), Paul Scherrer Institute (PSI), Villigen, Switzerland, and the Institute of Resource Ecology (IRE) HZDR, Dresden, Germany, June 17–19, 2013.

- Arnold, T.
Immobilization of uranium in *Euglena* cells
- Bradbury, M.
Overview of radioactive waste management in Switzerland and in PSI/LES
- Churakov, S.
Multi-scale modelling of ion transport and sorption in clays.
- Fritsch, K.
Uranium(VI) sorption on montmorillonite in highly concentrated electrolyte solutions
- Husar, R.
Investigations into the formation of Np(IV)-silica colloids
- Kliem, S.
The Reactor Safety Research within the Institute of Resource Ecology
- Kosakowski, G.
Benchmarks and applications for reactive transport codes.

Raff, J.

Technology platform on basis of intelligent biomolecules from microbial isolates of a uranium waste pile with potential for many industrial applications

Soltermann, D.

Fe(II) uptake mechanisms and competitive sorption on 2:1 dioctahedral clay minerals.

Wieland, E.

Organics in a L/ILW repository: Impact on the engineered barrier and C-14 release from the near field.

Status-Seminar 2013:

„Nuclear Safety Research – From Reactors to Disposal“

HZDR, Dresden, Germany, December 11–13, 2013.

Bok, F.

Thermodynamic database development: from nuclear waste to technology resources

Cherkouk, A; Moll, H.

Microorganisms in host rocks of potential nuclear waste repositories and their interactions with actinides

Fischermeier, E.

In vitro reconstitution of a copper ATPase for structural and functional studies

Franzen, C.

Se chemistry in Rossendorf – From final repositories for a radioactive pollutant to biotechnological processing of a valuable resource

Fridman, E.

Overview of the research activities within the junior reactor physics group

Fritsch, K.

Actinide sorption at high ionic strengths

Gagell, C.; Zirnstein, I.

Microbiological characterization from mine water of flooded uranium mines in Germany

Hennig, C.

Polynuclear hydrolysis species and formate complexes of cerium(IV)

Hildebrand, H.; Schymura, S.; Franke, K.

Environmental fate of TiO₂ nanoparticles

Jordan, N.

Se(VI) sorption by haematite

Kliem, S.

Overview on DYN3D development and application to Light Water Reactors

Krawczyk-Bärsch, E.

Microbially mediated retention of radionuclides in biofilms grown in crystalline rock environments

Kulenkampff, J.

The GeoPET facility for radiotracer process tomography - Temporary relocation from Leipzig to Rossendorf

Lippmann-Pipke, J.

From tracer studies to reactive transport modelling

Lozano Rodriguez, J.

BMBF-CONDITIONING: First XAFS results

Merk, B.

Research at FWO in the Subtopic Nuclear Waste Management

Oertel, J.; Obeid, M.

Influence of low uranium concentrations on different bacterial strains using calorimetric metabolic monitoring

Poetsch, M.; Lippold, H.

The influence of salinity and organic matter on the mobility of Tb(III) in clay

- Prieur, D. (ITU)
Application of XAS to nuclear material science
- Richter, C.
U-sorption onto mica and feldspars
- Rossberg, A.
Data mining with artificial neural networks: U(VI) sorption complexes and aqueous U(VI) complexes with aliphatic (hydroxy-) carboxylic acids
- Sachs, S.
Interaction of Eu(III) with mammalian cells: Influence of Eu(III) concentration, nutrient composition and the presence of ^{152}Eu
- Schäfer, F.
System codes for nuclear and non-nuclear applications - Accident analysis, severe accident research and solar power plants
- Scheinost, A.C.; Steudtner, R.
BMBF-IMMORAD: Activities and results
- Schott, J.
Combining different spectroscopic techniques to characterize Eu-B interactions
- Schmeide, K.
Actinide migration through clay rocks
- Schulz, K.
EXAFS study of U(VI) with N,O donor ligands in methanolic solution
- Tsushima, S.
Photochemical reaction of uranyl complexes: structure is the key
- Vogel, M.
Advanced technologies for bacterial cell encapsulation for water treatment

TEACHING ACTIVITIES

Lectures

Bernhard, G.

Radiochemistry

*Technische Universität Dresden
Summer term 2013*

Environmental chemistry

*Technische Universität Dresden
Summer term 2013*

Brendler, V.

Radiochemie 2

*University of Applied Sciences, Dresden
Summer term 2013*

Fahmy, K.

Biophysics

*Dresden-International-PhD-Programme
(DIPP), Technische Universität Dresden
Winter term 2012/2013*

Biophysikalische Methoden

*Modul in "Soft Condensed Matter and
Biophysics"
Winter term 2012/2013*

UV-vis and infrared spectroscopy

*BIOTEC-Master-Course, Technische Universität
Dresden
Winter term 2012/2013*

Kretzschmar, J.

Seminar: "Strukturbestimmung"

*Technische Universität Dresden
Summer term 2013*

Lippold, H.

Radiochemische Analysenmethoden

*University of Leipzig
Summer term 2013*

Entstehung und Eigenschaften ionisierender Strahlung

*University of Leipzig
Summer term 2013*

Raff, J.

Mikrobiologie

*University of Applied Sciences, Dresden
Winter terms 2012/2013 & 2013/2014*

Technische Biochemie

*University of Applied Sciences, Dresden
Summer term 2013*

Courses

☞ The laboratory course "Radiochemistry" was provided from August 19th to 23rd and from 26th to 30th, 2013, as a part of a module of the chemistry master degree program at the Technische Universität Dresden.

Advisers:

Drobot, B.	Kostudis, S.	Schulz, K.
Fischer, S.	Kretzschmar, J.	Suhr, M.
Fritsch, K.	Dr. Müller, K.	Dr. Vogel, M.
Gagell, C.	Nebe, K.	
Heim, H.	Richter, C.	
Husar, R.	Schott, J.	

☞ The IRE provided one experiment "Alpha spectrometric isotope dilution analysis of uranium" of the laboratory course "Instrumental Analysis" held by the Institute for Analytical Chemistry, Technische Universität Dresden, during winter term.

Advisers:

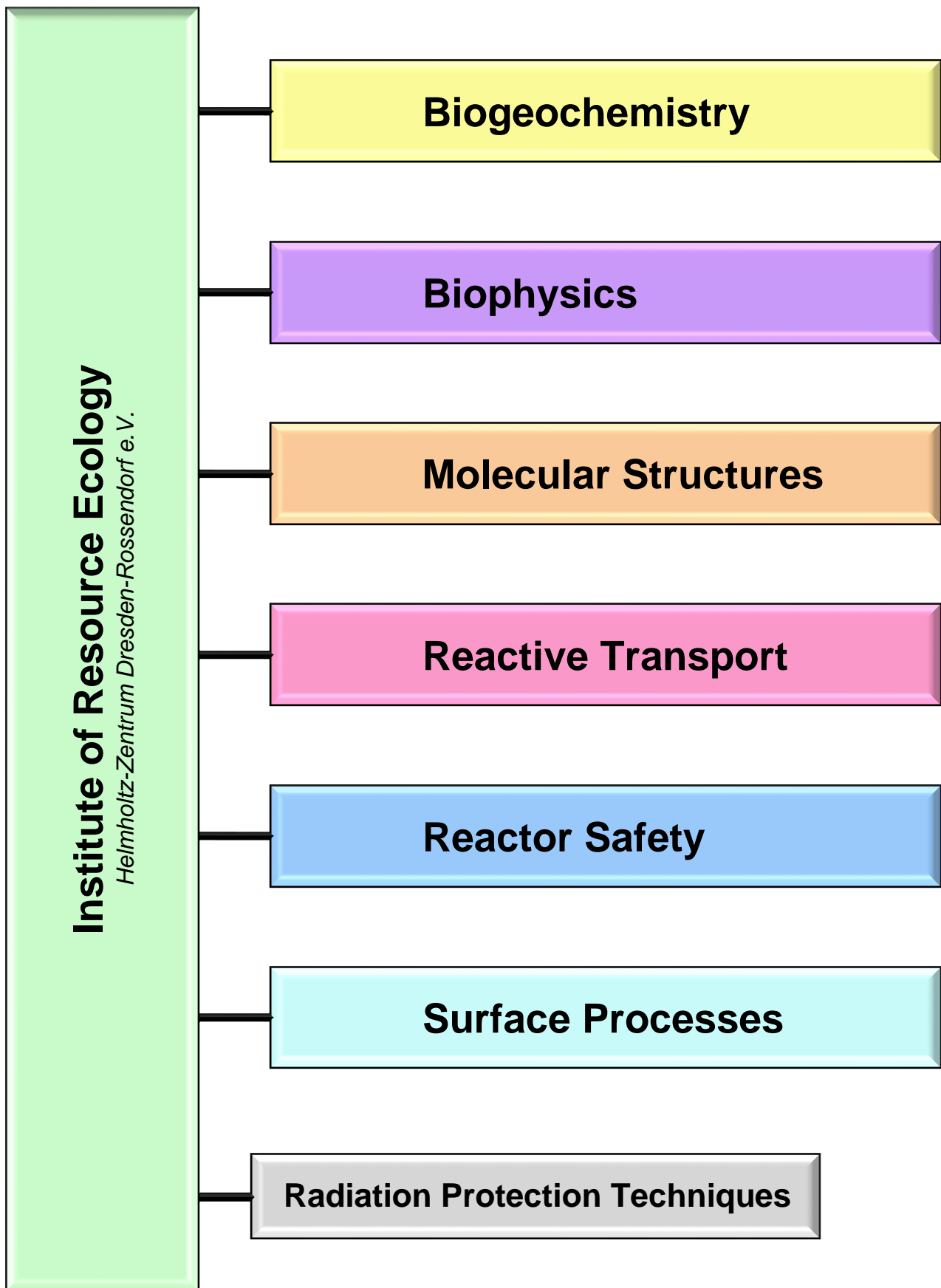
<i>Winter term 2012-13</i>	<i>Winter term 2013-14</i>
Fritsch, K.	Gagell, C.
Lindner, K.	Nebe, K.
Mickein, K.	Weiß, S.
Schott, J.	Zirnstein, I.
Weiß, S.	

☞ Biophysics course of the Dresden-International-Graduate School
December 02–13, 2013

Advisers:

Dr. Fahmy, K.	Philipp, J.
Groß, M.	Sayed, A.
Dr. Oertel, J.	

PERSONNEL



Prof. Dr. T. Stumpf (Director since Oct. 01, 2013)
Dr. V. Brendler (Acting director until Sept. 30, 2013)

ADMINISTRATION:

Gorzitze, Jana; Lauke, Regina; Mauersberger, Anke; Berndt, Ronny (Sysad)
 Kurde, Kerstin; Glückert, Marion (ESRF); Gerstner, Katrin (FS Leipzig)

RADIATION PROTECTION TECHNIQUES:

Heim, Heidemarie; Falkenberg, Dirk; Henke, Steffen; Hiller, Bernd; Nebe, Kathrin;
 Rumpel, Annette

D I V I S I O N S

BIOGEO-CHEMISTRY

Dr. Geipel, Gerhard

Dr. Arnold, Thuro
 Dr. Baumann, Nils
 Dr. Cherkouk, Andrea
 Drobot, Björn
 Dudek, Monika
 Flemming, Katrin
 Gagell, Corinna
 Gerber, Ulrike
 Dr. Großmann, Kay
 Dr. Günther, Alix
 Dr. Heller, Anne
 Heller, Sylvia
 Dr. Krawczyk-Bärsch, Evelyn
 Dr. Lütke, Laura
 Dr. Matys, Sabine
 Dr. Moll, Henry
 Müller, Manuela
 Dr. Raff, Johannes
 Ramisch, Alexander
 Dr. Sachs, Susanne
 Schulz, Katja
 Seibt, Jana
 Dr. Selenska-Pobell, Sonja
 Dr. Vogel, Manja
 Zirnstein, Isabel

BIOPHYSICS

Dr. habil. Fahmy, Karim

Abu Shark, Sawsan E.
 Fischermeier, Elisabeth
 Kummer, Ulrike
 Dr. Oertel, Jana
 Philipp, Jenny
 Sayed, Ahmed M. T.
 Suhr, Matthias
 Dr. Tsushima, Satoru

MOLECULAR STRUCTURES

Dr. habil. Scheinost, Andreas C.

Dr. Butzbach, Randolph
 Dulnee, Siriwan
 Exner, Jörg
 Fengler, Matthias
 Dr. Hennig, Christoph
 Dr. Lozano Rodriguez, Janeth
 Dr. Rossberg, André
 Dr. Steudtner, Robin

External Ph. D. students

Attia, Enas M. H.
 Dr. Brockmann, Sina
 Müller, Mathias
 Müller, Melanie
 Obeid, Muhammad H.
 Osman, Ahmed. A. A.
 Sabäu, Andrea

REACTIVE TRANSPORT

Dr. Lippmann-Pipke, Johanna

Claus, Benjamin Manuel
 Dr. Franke, Karsten
 Gründig, Marion
 Gruhne, Stefan
 Dr. Hildebrand, Heike
 Korn, Nico
 Dr. Kulenkampff, Johannes
 Dr. Lippold, Holger
 Lösel, Dagmar
 Dr. Mansel, Alexander
 Mickein, Kathleen
 Poetsch, Maria
 Schößler, Claudia
 Dr. Schymura, Stefan
 Zakhnini, Abdelhamid

REACTOR SAFETY

Dr. Kliem, Sören

Dr. Baier, Silvio
 Baldova, Daniela
 Bilodid, Yurii
 Dr. Dürigen, Susan
 Dr. Fridman, Emil
 Glivici-Cotruta, Varvara
 Gommlich, André
 Dr. Grahn, Alexander
 Hoffmann, Alexander
 Holt, Lars
 Konheiser, Jörg
 Kozmenkov, Yaroslav
 Litskevich, Dzianis
 Dr. Merk, Bruno
 Nikitin, Evgeny
 Rachamin, Reuven
 Dr. Rohde, Ulrich
 Dr. Schäfer, Frank
 Dr. Tusheva, Polina

SURFACE PROCESSES

Dr. Brendler, Vinzenz

Dr. Foerstendorf, Harald
 (Acting head –Oct. 31, 2013)
 Dr. Barkleit, Astrid
 Dr. Bok, Frank
 Eckardt, Carola
 Fischer, Sarah
 Dr. Franzen, Carola
 Fritsch, Katharina
 Dr. Gückel, Katharina
 Gürtler, Sylvia
 Heim, Karsten
 Hellebrandt, Stefan
 Dr. Huittinen, Nina
 Husar, Richard
 Dr. Jordan, Norbert
 Kretzschmar, Jerome
 Müller, Christa
 Dr. Müller, Katharina
 Neubert, Heidrun
 Peschel, Sophia Elisabeth
 Dr. Richter, Anke
 Richter, Constanze
 Ritter, Aline
 Dr. Schmeide, Katja
 Dr. Schmidt, Moritz
 Schott, Juliane
 Dr. Stockmann, Madlen
 Weiß, Stephan
 Dr. Zänker, Harald

GUEST SCIENTISTS

Bernhard, Gert	<i>Radiochemie Technische Universität Dresden</i>
Comarmond, M. Josick	<i>Institute for Environmental Research, Australian Nuclear Science and Technology Organisation, Menai, Australia</i>
Gomez, Cynthia	<i>Leonardo da Vinci trainees program</i>
Hofinger, Jürgen	<i>Namos GmbH, Dresden, Germany</i>
Kania, Ewa	<i>Wroclaw University of Technology</i>
Lehrer, Tamar	<i>Technion - Israel Institute of Technology Civil and Environmental Engineering Haifa, Israel</i>
Moral, Ana	<i>Leonardo da Vinci trainees program</i>
Roos, Steffen	<i>Namos GmbH, Dresden, Germany</i>
Sabäu, Andrea	<i>Agence Nationale pour la gestion des Déchets RAdioactifs, Châtenay-Malabry, France, Laboratoire Ecosystèmes Côtiers Marins Et Réponses aux stress (ECOMERS/EA 4228), Parc Valrose, Nice, France</i>
Skierski, Maciej	<i>Institute of Waste Disposal, Karlsruhe Institute of Technology, Karlsruhe, Germany</i>
Solioz, Marc	<i>Department of Clinical Pharmacology, University of Berne, Berne, Switzerland</i>
Zemb, Thomas	<i>Institut de Chimie Separative de Marcoule, Marcoule, France</i>

MASTER/DIPLOMA/BACHELOR

Bittner, Lars	Hildebrand, Pia	Luthardt, Paula	Zabelt, Denise
Domaschke, Kristin	Jäckel, Elisabeth	Maffert, Anika	Zehlike, Lisa
Domaschke, Steffen	Köppchen, Sandra	Stuhlfauth, Christin	
Gröschel, Annett	Leipold, Thomas	Viacava Romo, Karen Elda	

GRADUATE ASSISTANTS, STUDENT ASSISTANTS, TRAINEES

Berger, Julia	Friebel, Cindy	Peuker, Lisa Christin	Wagner, Oliver
Berger, Maria	Friebel, Michael	Quast, Dennis	Zechel, Susanne
Cordiez, Maxence	Kermes, Sissi	Rehak, Josephine	Zimmermann, Veit
Döge, Sarah	Köpke, Dorina	Sander, Madlen	
Fischer, Sarah	Kuczera, Mirco	Strobel, Alexander	

ACKNOWLEDGEMENTS

The Institute of Resource Ecology is one of the eight institutes of the Helmholtz-Zentrum Dresden-Rossendorf e.V. (HZDR). As registered, non-profit institution, the HZDR is supported by the authorities of the Federal Government and the Free State of Saxony. In addition to the basic funding, the financial support of the projects listed below by the given organizations and companies is gratefully acknowledged.

FUNDING ORGANIZATION / COMPANY	PROJECT TITLE	CONTRACT NO.
Commission of the European Communities (EU)	ACTINET Integrated Infrastructure Initiative (ACTINET-I3)	232631
	CROCK Crystalline Rock Retention Processes	FP7-269658
	EVOL Evaluation and Viability of Liquid Fuel Fast Reactor Systems	FP7-249696
	FREYA Fast Reactor Experiments for hYbrid Applications	FP7-2696665
	HEXANE Heavy Elements X-ray Absorption Spectroscopies Network	230807
	SARGEN IV Safety Assessment for Reactors of Generation IV	FP7-295446
	TALISMAN Transnational Access to Large Infrastructures for a Safe Management of ActiNide	FP7-323300
Bundesministerium für Wirtschaft und Technologie (BMW) & Bundesministerium für Bildung und Forschung (BMBF)	Conditioning Grundlegende Untersuchungen zur Immobilisierung langlebiger Radionuklide mittels Einbau in endlagerrelevante Keramiken	02NUK021B
	DIL Water Untersuchungen zur Entwicklung neuer Biokompositmaterialien zur Entfernung von Schadstoffen aus Abwässern	02WA1223
	IMMORAD Grundlegende Untersuchungen zur Immobilisierung langlebiger Radionuklide durch die Wechselwirkung mit endlagerrelevanten Sekundärphasen	02NUK019D
	Kompetenzerhalt in der Strahlenforschung Verbundprojekt: Multifunktionelle Komplexbildner mit N, O, S-Donorfunktionen für d- und f-Elemente	BMBF-FZK 02NUK014B
	P&T Partitioning and Transmutation	FKZ: 1501446
	Verbundprojekt: Rückhaltung endlagerrelevanter Radionuklide im natürlichen Tongestein und in salinaren Systemen – Geochemisches Verhalten und Transport von Radionukliden (Np, U, Pu und weitere RN) in salinaren Systemen in Gegenwart endlagerrelevanter Organika	BMW 02E10971
	Strahlung und Umwelt II Verbundprojekt: Radionuklide in der Umwelt, ihr Transport in die Nahrungsketten zum und im Menschen, Teilprojekt F	BMBF-FZK 02NUK015F
	TransAqua Teil A	02NUK030F
	TransAqua Teil B	02NUK030F
	VESPA Verbundprojekt: Verhalten langlebiger Spalt- und Aktivierungsprodukte im Nahfeld eines Endlagers und Möglichkeiten ihrer Rückhaltung	FZK-BMW 02E10790

FUNDING ORGANIZATION / COMPANY	PROJECT TITLE	CONTRACT NO.
	VESPA – Aufstockung	FZK-BMWi 02E10790X
	WASA-BOSS	
	WEIMAR	BMWi 02 E 11072B
	Wissenschaftler austausch Frau Tamar Lehrer	YSEP 76
	WTZ-Russland- Fluenzberechnungen	FKZ: 1501403
	WTZ Russland - Transientenanalysen für schnelle Reaktoren	1501462
Deutsche Forschungsgemeinschaft (DFG)	Imaging and image simulation of organic target compound migration between different biogeochemical interfaces of a soil horizon using position emission tomography and the lattice Boltzmann equation approach (BIG)	LI 872/5-1
	Sorptions- und Redoxreaktionen von Sn II und Sn IV an der Magnetite/Wasser-Grenzfläche in An- und Abwesenheit organischer Liganden (Zinn-Redox)	SCHE 509/3-1
	Surface processes of Np species on selected mineral oxides. From sorption to precipitation	MU 3207/1-1
	Transport von CNP	FR 1643/3-1
Project Management Jülich & BMBF	Nano Track	03X0078A
	Untersuchung des Lebenszyklus von Nanopartikeln anhand von [⁴⁵ Ti]TiO ₂ und [¹⁰⁵ Ag]Ag ₀	
	NANOPHARM	03X0094G
	Neue photokatalytisch aktive Verbundmaterialien zur Eliminierung von pharmazeutischen Reststoffen	
AREVA	Experimente PKL3	
ANDRA, Paris, France	Pollutant Trapping	RCOT ASEV 110027
Bundesamt für Strahlenschutz (BfS)	THEREDA-SZ II	WS 2051-8732-9
	Vervollständigung einer Thermodynamischen Standarddatenbasis	
	Cryo-Fluoreszenzspektroskopie	3342
BMBF & DLR	AptaSens	01RB0805A
	Aptamer modifizierte bakterielle Oberflächenstrukturen für die Entwicklung neuer Sensoren	
E.ON, Hannover	MCNP Rechnungen	4500063558/KM E/0701
	Datenpflege ATHLET-Datensatz für 2013 2014	
	Datensatzerstellung Vor-Konvoi-Anlage	4500047740/KM E/0701
	DYN3D	4500081577/KM E/0701
	Analyse von Neutronenflussrauschen	
	Entwicklung eines Modells thermo mechanisches Brennstabverhalten	4570157785/IQ4 /0701/NB
VGB Powertech	Kopplung Neutronik/ Thermohydraulik für DWR	SA "AT" 41/09 A
	Kopplung Neutronik/ Thermohydraulik für SWR (TU Dresden)	SA "AT" 41/09 C
TÜV SÜD	Reaktorberechnungen für WWER-1000-Reaktoren	500601247

FUNDING ORGANIZATION / COMPANY	PROJECT TITLE	CONTRACT NO.
STFI	Textilien S-Layer	
UJV Rez, a.s.	DYN3D für UJV Wartung 2012/2013	150178
Wismut	Spezialanalytik WISMUT II	Vertrag 3164929-U02/1
SAB Förderbank, Dresden, Germany	SYNCOPE Synergetische Kopplung von Energieträgern für effiziente Prozesse	100109023
GRS	Codetraining Belarus	
HGF	HGF-Nachwuchsgruppe Dr. Schmidt	VH-NG-942
SCK•CEN, Studiecentrum voor Kernenergie, Brussels, Belgium	Mont Terri BN-experiment pH 17	

INDEX OF AUTHORS

AUTHOR	PAGE	AUTHOR	PAGE
Abdala, P. M.	40	Köppchen, S.	11
Acker, M.	23, 24, 27	Kozmenkov, Y.	56
Altmaier, M.	36	Kraus, W.	40
Arnold, T.	10, 11, 12	Krawczyk-Bärsch, E.	9
Bachvarova, V.	14, 15	Kretschmar, J.	27, 39
Baldova, D.	59	Lehmann, F.	19
Banerjee, D.	43	Leipold, T.	49
Barkleit, A.	16, 20, 22, 27, 46	Lippmann-Pipke, J.	49
Baumann, N.	10	Lippold, H.	25
Belle, C. J.	41	Litskevich, D.	46, 55
Berger, J.	34	Lozano-Rodriguez, M. J.	41
Bernhard, G.	14, 15, 26	Lucks, C.	28
Bok, F.	46, 47, 48	Lütke, L.	14, 15
Brendler, E.	39	Maffert, A.	35
Brendler, V.	13, 27, 39, 46, 47	Merk, B.	55
Cherkouk, A.	15	Moll, H.	14, 15, 19, 31
Cuello, G.	43	Müller, K.	31, 34
Domaschke, K.	28	Müller, M.	23, 24
Domaschke, S.	37	Neumeier, S.	41
Drobot, B.	19, 31	Oertel, J.	22
Duerigen, S.	53	Opherden, L.	22
Dumas, T.	36	Pannier, A.	18
Emerich, H.	40	Pattison, P.	40
Fahmy, K.	21, 22, 31	Pollmann, K.	18, 21
Fellhauer, D.	36	Rachamin, R.	61
Fischer, S.	17	Raff, J.	17, 18, 19, 21
Foerstendorf, H.	32, 37	Richter, A.	48
Franke, K.	42, 49	Richter, C.	13, 46
Franz, R.	60	Rohde, U.	54, 56
Franzen, C.	17, 37, 38, 39	Röske, I.	11, 12
Fridman, E.	59, 61	Röske, K.	12
Fritsch, K.	33	Rossberg, A.	26, 28, 31, 36
Gagell, C.	12, 13	Sachs, S.	16
Galperin, A.	61	Scheinost, A. C.	35, 36, 37, 40, 41, 43
Gaona, X.	36	Schmeide, K.	9, 33
Grahn, A.	58	Schott, J.	27, 46
Großmann, K.	13	Schulz, K.	26
Günther, A.	26	Schymura, S.	42
Hauser, J.	49	Selenska-Pobell, S.	14, 15
Heim, K.	32, 37, 38	Simon, U.	41
Heller, A.	46	Soltmann, U.	18
Hennig, C.	20, 40, 43	Stedtner, R.	17, 21, 31, 35
Hering, D.	38	Stockmann, M.	46
Hildebrand, H.	42	Suhr, M.	21
Hoffmann, A.	57	Taube, F.	24
Holt, L.	54	Taut, S.	23, 24, 27
Honkimäki, V.	43	Tsushima, S.	28, 31
Hübner, R.	45	Ulbricht, I.	44
Husar, R.	44, 45	Viacava Romo, K. E.	21
Ikeda-Ohno, A.	40, 43	Vogel, M.	17, 18
Jenk, U.	12	Weiß, S.	37, 38, 40, 43, 44, 45
Jordan, N.	32, 37, 38, 39, 46	Wesch, G. E.	41
Joseph, C.	46	Zänker, H.	43, 44, 45
Keller, A.	22	Zimmermann, V.	37
Kliem, S.	54, 60	Zirnstein, I.	11
Konheiser, J.	58		

HZDR

 **HELMHOLTZ**
| ZENTRUM DRESDEN
| ROSSENDORF

Institute of Resource Ecology
P.O. Box 51 01 19 · 01314 Dresden/Germany
Phone +49 351 260-3210
Fax +49 351 260-3553
Email contact.resourceecology@hzdr.de
<http://www.hzdr.de>

Member of the Helmholtz Association